Helsinki University of Technology Publications in Engineering Physics
Teknillisen korkeakoulun teknillisen fysiikan julkaisuja
Espoo 2005 TKK-F-A836

Magnetohydrodynamic stability analyses of tokamak edge plasmas

Samuli Saarelma

Dissertation for the degree of Doctor of Science in Technology to be presented with due permission of the Department of Engineering Physics and Mathematics for public examination and debate in Auditorium F1 at Helsinki University of Technology (Espoo, Finland) on the 22nd of April, 2005 at 12 noon.

Helsinki University of Technology
Department of Department of Engineering Physics and Mathematics
Laboratory of Advanced Energy Systems

Distribution:

Helsinki University of Technology

Department of Department of Engineering Physics and Mathematics

Laboratory of Advanced Energy Systems

P.O Box 2200

FIN-02015 HUT, Finland

E-mail:samuli.saarelma@ukaea.org.uk

© 2005 Samuli Saarelma

ISBN 951-22-7600-3 (printed)
ISBN 951-22-7601-1 (pdf)

ISSN 1456-3320 (printed)
ISSN 1459-7268 (pdf)

Otamedia Oy
Espoo 2004

HELSINKI UNIVERSITY OF TECHNOLOGY
P.O. BOX 1000, FIN-02015 HUT
http://www.hut.fi

ABSTRACT OF DOCTORAL DISSERTATION

Author Samuli Saarelma

Name of the dissertation

Magnetohydrodynamic stability analyses of tokamak edge plasmas

Date of manuscript 17th of March, 2005 | Date of the dissertation 22nd April, 2005

☐ Monograph ☑ Article dissertation (summary + original articles)

Department Engineering Physics and Mathematics
Laboratory Advanced Enegy Systems
Field of research Fusion and plasma physics
Opponent(s) Dr. Arthur Peeters, IPP-Garching, Germany
Supervisor Prof. Rainer Salomaa, Helsinki University of Technology
(Instructor) Dr Taina Kurki-Suoni, Helsinki University of Technology

Abstract

Edge Locilised Modes (ELMs) are edge phenomena in fusion plasmas that cause small bursts of energy and particles out of the plasma. In a fusion devices such as a tokamak, ELMs affect the plasma confinement and can cause divertor plate erosion. Therefore, for the operation of a tokamak fusion plasma it is important to understand the physical mechanisms behind the ELM phenomenon and to be able to minimise the detrimental effects of the ELMs.

In this thesis, the ELMs are modelled using magnetohydrodynamic stability analysis. First an accurate equilibrium of the experimental plasma is created and then the stability of the equilibrium is analysed. The stability analyses show that the Type I or 'giant' ELMs in ASDEX Upgrade and JET plasmas are triggered by peeling-ballooning modes with low to intermediate toroidal mode number (n). The radial struture of these modes is relatively wide and is localised near the edge of the plasma. The ASDEX Upgrade plasmas with smaller Type II or 'grassy' ELMs are found to have narrower mode structure of the triggering instability. The stability against low-n modes is improved as well causing the triggering instability to shift to higher n. Increased plasma pressure in the core region is found to improve the stability of the edge against low-n instabilities. This can explain the easier access to Type II ELMs observed in such plasmas. The Type III ELMs in JET plasmas are found to be deep in the stable region against the low- to intermediate-n peeling-ballooning modes and are likelyto triggered by a different mechanism than other ELMs. Of various ELM-control methods, pellet triggering is studied and it is found that pellet-triggered ELMs are destabilised by the same mechanism as intrinsic Type I ELMs. In quiescent H-mode where no ELMs are observed, the plasma edge stability is significantly better than in similar ELMy plasmas. This can explain the absence of ELMs.

Keywords ELM, stability, modelling, edge plasma, MHD

UDC | Number of pages 144

ISBN (printed) 951-22-7600-3 | ISBN (pdf) 951-22-7601-1

ISBN (others) | ISSN 1456-3320 (printed) 1459-7268 (pdf)

Publisher Otamedia Oy

Print distribution Advanced Energy Systems P.O. Box 2200, FIN-021015 HUT, Finland

☑ The dissertation can be read at http://lib.hut.fi/Diss/ 2005/isbn9512276011/

Preface

The origin of this thesis is in a one week intensive course on Magnetohydrodynamic instabilities lectured by Prof. Hartmut Zohm in 1997. I was in the middle of doing my Master's thesis on MHD equilibrium and knew already something about the subject, but of course there was a lot of new material, too. In the end of the course, there was an oral examination. That was very new to me (and probably also to other Finnish students) and naturally, I was quite nervous. But I think, it went quite well, since in the end, Hartmut asked me if I were interested in continuing on this subject and come to Germany after I finished my Master's thesis. I had not expected this kind of a question in an exam, but after a little thought I answered yes and that put the wheels in motion.

After finishing the Master's thesis, continued as a graduate student at the Laboratory of Advanced Energy Systems in Helsinki University of Technology under the wings of Prof. Rainer Salomaa. However, as we had agreed with Hartmut, a part of the work would be done at IPP in Garching, Germany. During the following years, I spent a fews months in Garching and the rest of the time in Finland. In Garching, I was supervised by Prof. Sibylle Günter to whom I am indebted in gratitude for the inspiration and support during my visits. Of other co-workers in Garching who I would like to mention for their help on this journey are Dr. Hans-Peter Zehrfeld, Dr. Lorne Horton and Dr. Wolfgang Suttrop. I am also grateful to the entire ASDEX Upgrade experimental team for providing the data for my calculations as well as explaining how to use it.

It turned out that for my analyses of ASDEX Upgrade plasmas I needed an MHD stability code and a suitable one was at General Atomics in San Diego, USA. My visit there was very fruitful and thanks for that goes to Dr. Alan Turnbull.

Thanks to Rainer's pushing, in addition to ASDEX Upgrade, I also had a chance to work on JET experiment in UK. For the support of my work there, I am grateful for the entire JET experimental team and for Dr. Vassili Parail in particular for his guidance in my stability analyses.

Despite these many visits, the bulk of the work for this thesis was done at HUT in Espoo. The people in the laboratory created a good working environment and it felt bad to leave them all behind. At HUT, the person who basically kept me going through the years that it took to write this thesis is Dr. Taina Kurki-Suonio. I am especially thankful for her for the way she "forced" me to really understand what I was doing by asking the right questions. She has also been invaluable in the writing process of not only this thesis but also other publications.

This thesis has required a lot of hard work. I could not have survived through all that without the support of my parents and my sisters. The questions such as Valpuri's:"Is fusion safe ?" showed your interest in my work and kept my motivation high. Last but not least, I want to thank my wife Yang for your patience and care during the time I have been writing this thesis.

The funding for this work has come from Euratom-TEKES. The cost of visits to other institutes have been covered by Euratom Staff Mobility. I also received a personal support from Fortumin Säätiö. I owe gratitude to these organisations. Most of the results presented in this thesis have been calculated using computational resources of Finnish Centre for Scientific Computing.

Original Publications

1. Saarelma, S., Günter, S., Kurki-Suonio, T. and Zehrfeld, H-P. "ELM phenomenon as an interaction between bootstrap-current driven peeling modes and pressure-driven ballooning modes." Plasma Physics and Controlled Fusion, 2000. Vol. 42, nro 5A, p. A139.

2. S. Saarelma, S. Günter, T. Kiviniemi, T. Kurki-Suonio, ASDEX Upgrade Team, "MHD Stability Analysis of Type II ELMs in ASDEX Upgrade" Contributions to Plasma Physics, 2002, Vol 42, 277.

3. S. Saarelma, S. Günter, L.D. Horton and ASDEX Upgrade Team, "MHD stability analysis of type II ELMs in ASDEX Upgrade", Nuclear Fusion, 2003, Vol 43, 262-267.

4. S. Saarelma, S. Günter, "Edge Stability Analysis of High β_p Plasmas", Plasma Physics and Controlled Fusion, 2004, Vol 46, 1259-1270.

5. S. Saarelma V. Parail, Y. Andrew, E. de la Luna, A. Kallenbach, M. Kempenaars, A. Korotkov, A. Loarte, J. Lönnroth, P. Monier-Garbet, J. Stober, W. Suttrop and Contributors to the EFDA-JET workprogramme, "MHD Stability Analysis of Diagnostic Optimized Configuration (DOC) shots in JET" , Plasma Physics and Controlled Fusion, 2005, Vol 47, 713-731.

Contents

Chapter 1

Introduction

Since the beginning of industrialisation, mankind has become increasingly dependent on cheap and abundant energy. The energy consumption has steadily grown in the past and is expected to do so in the future. Until now, the energy demand has been met mainly by burning fossil fuels. However, two issues prohibit basing further growth on them. First, the known oil and gas resources will last only a few decades with current consumption. In the second half of this century, their use will come to an end even without any other constraints. Second, the environmental impact from burning fossil fuels may force mankind to phase them out even before the resources are exhausted.

One of the key questions of this century is how the gap between the ever-growing energy consumption and the decreasing fossil fuel use will be covered. Conventional nuclear energy that is based on the fission of heavy elements, like uranium, can contribute to the energy production, but without breeder reactors the uranium resources will not last longer than the fossil fuels. Furthermore, the fission power suffers from poor political acceptance due to the risk of a serious accident, long term radioactive waste, and its connections to nuclear weapons.

The renewables, wind and solar, show potential as a clean and abundant source of energy. While small now, it is possible that they provide a significant share of the energy in the future. However, in this work another future energy form, nuclear fusion, is investigated. Fusion energy is inherently safe and has very little effect on the environment. Its use does not create a long-term radioactive waste problem. Best of all, its fuel reserves are practically inexhaustible. The scientific and technological research and development of the peaceful use of fusion energy started in 1950's. The task has proved very challenging, but it is expected that fusion energy can start contributing to the world's energy production in the second half of the century.

1.1 The basics of nuclear fusion

In nuclear fusion, two light nuclei are fused together into a heavier nucleus. The lost mass in the reaction is turned into energy according to the famous Einstein's $E = mc^2$ law. On earth, the most prospective reactions for fusion energy production are:

$$\begin{aligned} \mathrm{D} + \mathrm{D} &\rightarrow {}^{3}\mathrm{He} + \mathrm{n} + 3.27\ \mathrm{M}eV \\ \mathrm{D} + \mathrm{D} &\rightarrow \mathrm{T} + \mathrm{H} + 4.03\ \mathrm{M}eV \\ \mathrm{D} + \mathrm{T} &\rightarrow {}^{4}\mathrm{He} + \mathrm{n} + 17.6\ \mathrm{M}eV \end{aligned}$$

$$\mathrm{D} + {}^3\mathrm{He} \rightarrow {}^4\mathrm{He} + \mathrm{H} + 18.3\ \mathrm{M}eV.$$

The reaction between deuterium and tritium is the most probable one. Therefore, all the current scientific research efforts are concentrated on realising a fusion reactor that uses deuterium-tritium fuel, and at least the first fusion reactors are expected to use it in energy production. Deuterium is readily obtained from sea water. Tritium can be bred from lithium that is abundant in the earth's crust.

The nuclei have a positive electric charge that makes them repel each other. The fusing nuclei must have enough kinetic energy to overcome the electric repulsion force and get within the range of the attractive nuclear force. This sets a requirement for the fusion fuel. It must be very hot, with a temperature of about 100 million degrees C. At this temperature the matter is in the form of a plasma. In plasma, the atoms are broken into free electrons and ions. Since fusion plasma is very hot, the most crucial question is how to confine it before it gets in contact with solid materials and cools down.

In the Sun, the largest fusion reactor in the solar system, the gravitational force takes care of the confinement of the hot plasma. However, on earth, this method is not suitable for power-producing reactor. The gravitational force is far too weak to be used in a fusion power reactor scale. Therefore, other ways to confine the hot plasma and produce fusion energy has had to be found. There are two main approaches for building a fusion power reactor: inertial and magnetic confinement.

In inertial confinement, a small fusion fuel target sphere is imploded using powerful lasers or particle beams. The temperature and density in the centre of the target reach the conditions required for the fusion reactions and the target ignites. The process can be interpreted as a small nuclear explosion. As the name implies, the only confinement is that provided by the inertia of the particles.

In magnetic confinement, the plasma is confined using strong magnetic fields. In a magnetic field, the charged particles of the plasma (electrons and ions) can not move freely but instead gyrate around the magnetic field lines. The stronger the field, the smaller the gyration radius. Unfortunately, the magnetic field confines the particles only in the direction perpendicular to the field. Along the field lines, the particles can move freely. However, if the field lines are bent into a toroidal shape, it is possible to fully confine the particles.

In this thesis, a toroidal plasma device called tokamak is studied.

1.2 Tokamak

Tokamak is widely considered as the most promising device for harnessing fusion power for peaceful applications [1]. Of all magnetically confined plasmas, it holds the record of achieving, simultaneously, a high temperature, a long confinement time, and a high plasma density. At the time of this writing, the record value for fusion power in a tokamak is 16 MW [2].

Figure 1.1 shows a schematic picture of the tokamak concept. Because of the toroidal configuration of the magnetic field in a tokamak, it is useful to project the magnetic field lines in two coordinates. The *poloidal* direction goes the short way and the *toroidal* direction the long way around the torus. The plasma toroidal current induced by the central solenoid creates a poloidal magnetic field in the plasma. When this field is combined with

the magnetic field created by the external toroidal field coils, a helical field is created. The charged particles gyrating around the helical field lines are fully confined.

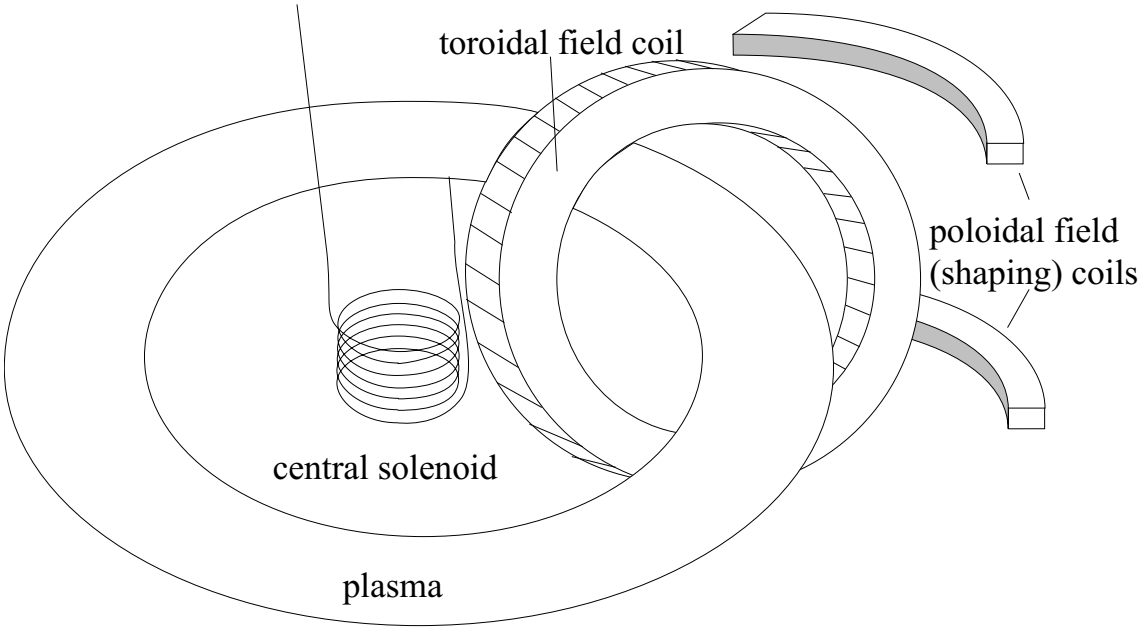

Figure 1.1: *The tokamak coil system. The plasma is confined using a plasma current generated by the central solenoid and stabilised using the magnetic fields generated by the toroidal field coils. The poloidal field coils are used to shape and position the plasma.*

In addition to the magnetic coils shown in Fig. 1.1, the tokamak contains various *heating devices* (neutral beam injectors, radio frequency antennas). The plasma itself is kept inside a *vacuum vessel*. The edge of the plasma is allowed to have contact with solid surfaces only at special *limiters* or *divertors* which will be explained in detail in the following section. All the present-day tokamaks are still experimental devices and their function is scientific research, not fusion energy production. Therefore, they are usually equipped with extensive *diagnostics* to measure various plasma parameters, such as temperature, density, radiation and magnetic field fluctuations. In an actual energy producing reactor using DT-fuel, there would also be systems to transfer heat from the reactor to the turbines and a tritium breeding blanket.

Today, the biggest tokamak is JET (Joint European Torus) [3], situated in the United Kingdom and operated by the European Union. It holds the above-mentioned record for the fusion power production. However, its performance is still slightly below net power production with $P_{fusion}/P_{in} \approx 0.65$ [2]. Currently, it is the only tokamak in the world that can use fusion relevant deuterium-tritium fuel.

The second largest tokamak is JT-60U in Japan [4]. It operates with pure deuterium and, consequently, is not able to reach the same fusion performance as JET. However, it is possible to calculate what the fusion power production would be if deuterium-tritium fuel were used. In JT-60U, values of up to $P_{fusion}/P_{in} = 1.25$ have been reached for the virtual performance.

In addition to these two large devices, there are a number of medium and small scale tokamaks in the world, like ASDEX Upgrade in Germany, TORE SUPRA in France, DIII-

D and Alcator C-Mod in the United States. A description of all these devices is given in Ref. [1]. In addition to conventional tokamaks, there are also so-called spherical tokamaks that have a small aspect ratio, i.e. ratio between the overall size of the device and the thickness torus. At the moment, the largest spherical tokamak devices are MAST [5] in the United Kingdom and NSTX [6] in the United States.

In 2005, a decision on the construction of a large international experimental reactor, ITER (International Tokamak Experimental Reactor), is expected. ITER is designed to reach energy multiplication factor of 5-10, i.e., it should produce 5-10 times more fusion energy than it needs for confining and heating the plasma. The original ITER design [8] was finished in 1998, but it was found too expensive. To cut the cost of the machine, a new design with reduced objectives has been finalised [7].

1.3 Plasma-wall interaction, limiters and divertors

Even in the earliest tokamaks problems arose from the interaction between the plasma edge and the solid material surrounding it. When the hot fusion plasma comes into contact with solid material that surrounds it, the plasma gives its energy to the material and causes erosion. The eroded wall materials migrate into the plasma diluting it and increasing radiation losses. Without any control of the impurities, reaching fusion relevant conditions becomes impossible.

The first solution to the impurity problem was to isolate the plasma from the vacuum vessel wall with a limiter. The concept of the limiter operation is fairly simple. The helical magnetic field lines in a tokamak form nested toroidal surfaces. By placing a solid object, the limiter, into the plasma, the surfaces that are outside the outermost surface that is not in contact with the limiter are "scraped off" and the limiter becomes the only solid contact with the plasma. The plasma boundary is defined by the last closed flux surface that is not in contact with the limiter. The region just outside the boundary and in contact with the limiter is called the scrape-off layer or SOL. The limiter is made of materials that have high resistance against erosion and preferably also a low charge number Z. The lower the average charge number of the plasma, the less it radiates. The high-Z impurities also dilute the plasma more than low-Z impurities.

It turned out, however, that even with limiters it is difficult to reach fusion relevant conditions before impurities become a problem. The limiter temperature would still be too hot for the materials. The problem of impurities is greatly reduced by replacing the limiter with a divertor [9]. In a diverted plasma, the edge magnetic field configuration is altered using external poloidal coils (see Fig. 1.1), so that an x-point is created. The outermost closed magnetic surface, called the separatrix, becomes the plasma boundary. Inside the separatrix, the magnetic field forms closed flux surfaces. Outside the separatrix, the flux surfaces are open and the magnetic field lines lead to a special divertor, where the plasma is allowed to make contact with solid material. Unlike in the limiter configuration, the use of the separatrix allows placing the divertor plates far from the hot plasma. The temperature of the plasma that interacts with the divertor can be lower than the plasma temperature at the separatrix. Furthermore, the transport of impurities from the divertor plates to the core plasma is reduced from that of the limited plasma. Thus, the divertor allows tokamak operation at high plasma temperature without suffering from unacceptable erosion of the walls and influx of impurities. Figure 1.2 shows the difference

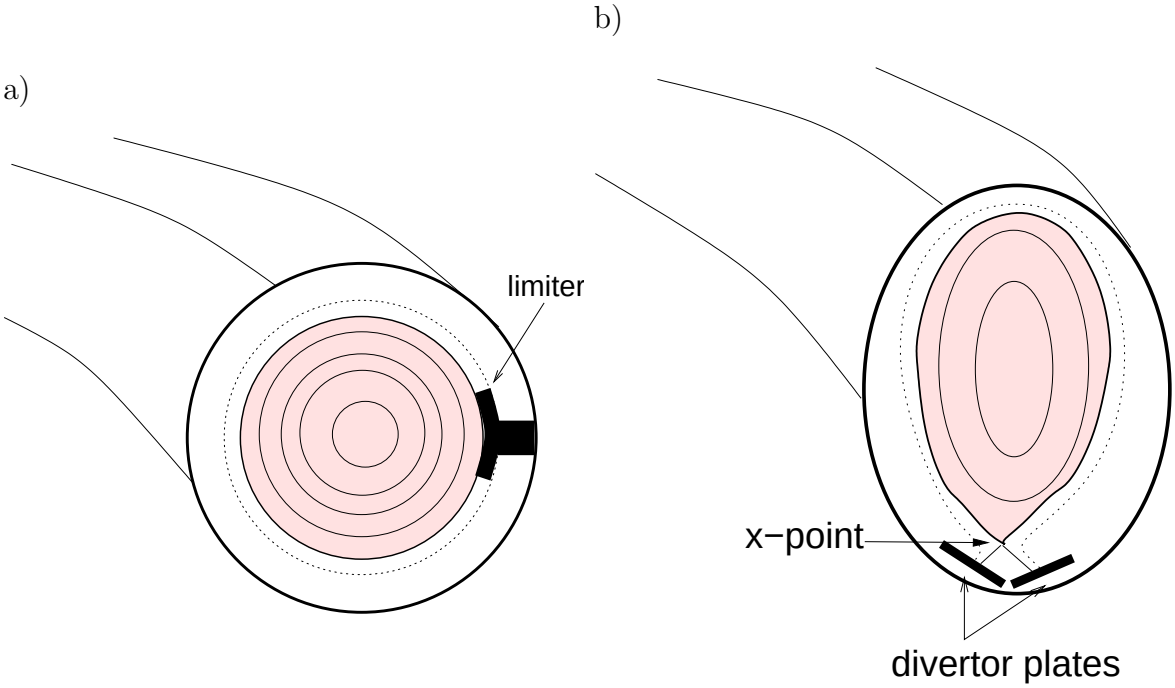

Figure 1.2: *The limiter a) and divertor b) concepts. The grey area represents the plasma. The closed lines inside plasma show the flux surfaces, and the dotted line outside the plasma boundary represents the extent of the scrape-off layer.*

between limiter and divertor configurations.

Even with the divertor concept, the plasma-wall interaction places demanding requirements for the materials to be used in a tokamak fusion reactors. In ITER, the divertor is subject to a heat load of 7-10 MW/m^2 [10]. On top of that, plasma edge bursts called ELMs (Edge Localised Modes) can deposit 25-80 MJ of energy on the divertor targets in a short period of time ($\approx 0.1 - 1.0$ms) [12]. Such short bursts of energy can cause ablation of the target material, which is unacceptable for the safe operation of the plasma. In addition to causing erosion on the plasma facing components, ELMs also affect the plasma performance, exhaust of helium ash and impurities, and global density of the plasma. They play such an important role in the physics of well-confined plasmas that understanding the physics of the ELM phenomenon and being able to control the ELM behaviour is necessary for tokamak fusion reactor development. They are also the topic of this thesis.

1.4 Outline of the thesis

The ELM phenomenon poses two main questions for the plasma physics research. First, what is the triggering mechanism of the ELMs, i.e. what causes the plasma to lose a large amount of energy and particles in a short burst ? Second, how can the ELM phenomenon be affected by changing the plasma conditions or, more specifically, how can the ELMs be reduced in size or eliminated completely ? This thesis tries to answer both of these questions.

The method used to study the ELM phenomenon is magnetohydrodynamics or MHD. MHD is a way to treat the plasma as a fluid whose motion is governed by the pressure of

the plasma and electromagnetic forces. The collective treatment of plasma particles allows global investigations of tokamak plasmas, as opposed to the local studies simulating the motion of individual particles. In particular, MHD is a well-suited tool for studying the equilibrium and stability properties of fusion plasmas. Chapter 2 gives a brief introduction to the MHD theory and describes how the MHD theory is used to analyse plasma equilibrium and stability properties in the study of the ELM phenomenon. The equilibrium reconstruction taking self-consistently into account the so-called bootstrap current is described. The concept of stability and a few instabilities most relevant to the ELMs are introduced.

Chapter 3 gives an introduction to the ELM phenomenon itself. ELM types, as well as a few other edge phenomena closely related to ELMs, are described. Experimental observations of ELMs and the operational regimes of different ELM types are discussed. A theoretical model for the ELMs is also introduced. This model will later be used in more detailed investigations of specific ELMy regimes. Finally, a few experimental methods that have been used in various tokamaks to control the ELMs are described.

Chapter 4 presents the results obtained in stability analyses of various ELMy plasmas. It also combines the results from the publications relevant to this thesis. In publication 1, the ELM model was tested for Type I ELMs in ASDEX Upgrade using experimental data. The plasma pressure profile was given by the temperature and density profiles, and the self-consistent equilibrium was calculated taking into account the bootstrap current. The MHD stability analysis of the equilibria with varying amount of bootstrap current showed that the plasma is indeed destabilised as the bootstrap current increases. This observation agrees with the proposed model.

With certain changes in the plasma conditions, the large Type I ELMs are replaced by smaller and more benign Type II ELMs. After the Type I ELM investigation, the analysis was extended to Type II ELMs by investigating the changes in the edge plasma stability due to the changes in plasma conditions that were experimentally required for Type II ELMs. The differences between the stability properties of Type I and Type II ELMy plasmas and how they can be used to explain the smaller amplitude of the Type II ELMs were studied in publications 2 and 3. Publication 4 presents analyses of the edge stability changes due to changes in the global plasma performance that is characterised by so-called β_p value. The stabilising effect of an increasing β_p is investigated using artificial plasma equilibria with varying values of core pressure. In some cases the ELMs can be avoided without sacrificing the plasma performance. In Section 4.3, the complete suppression of ELMs in the so-called quiescent H-mode is considered. The stability of the edge plasma in ELM-free operation is compared with the normal Type I ELMy operation and a possible mechanism for the ELM suppression is discussed.

In addition to operating the plasma in such conditions that the large ELMs are avoided, an active control of ELMs is another possible way to reduce the ELM size. In Section 4.4, one such method, launching small pellets to actively trigger ELMs, is discussed. The edge stability properties of plasmas with intrinsic high-frequency ELMs, intrinsic low-frequency ELMs and pellet-triggered high-frequency ELMs are compared. The results of the analysis can explain why the intrinsic and pellet-triggered high-frequency ELMs are similar to each other, while the intrinsic low-frequency ELMs are significantly different.

In publication 5, the stability analyses of ASDEX Upgrade ELMs were supplemented by a stability analysis of ELMs in JET. The emphasis of the analysis was on how the edge stability is altered using various external methods such as gas puffing, heating and

impurity injection. The stability changes were used to explain the changes in the observed ELM behaviour, especially in the transition from Type I to Type III ELMs.

The final chapter collect all the results from the analyses of ELMs and draws a comprehensive picture of the ELM phenomenon within the framework of linear MHD stability. Also a few guidelines for the future work are given.

During the course of this work, the stability calculations were done using well-established stability codes such as MISHKA, GATO and IDBALL. Since the bootstrap current plays an important role in the ELM triggering, the equilibrium code GRETA was modified to calculate the equilibrium takes into account the bootstrap current self-consistently.

Chapter 2

Methods

2.1 Magnetohydrodynamics

Plasma is composed of charged particles, electrons and ions. In a magnetic field, a charged particle gyrates around the field line, but is free to move along it. In principle it is possible to derive all the plasma phenomena from the behaviour of the individual particles and their interactions. However, in tokamak fusion plasmas, the number of particles is so high ($> 10^{20}$ electrons and ions in a medium size tokamak) that in practise it is impossible to follow the motion of all the particles individually. Magnetohydrodynamics or MHD is a way to describe plasma as a fluid that is controlled by electromagnetic forces. This makes it possible to describe macroscopic phenomena of the plasma without having to know the position and the velocity of individual particles.

The MHD description of plasma can be divided into two approaches depending on how the resistivity of plasma is treated. In the so-called *ideal MHD*, the plasma is considered to be perfectly conducting in contrast to the *resistive MHD* where this assumption is relaxed. The finite resistivity complicates the theoretical treatment of plasma and makes the numerical computations more expensive in terms of computer resources. Since a hot plasma has very high electrical conductivity, most plasma phenomena relevant to fusion reactors can be investigated using ideal MHD.

A characteristic dimension for MHD phenomena is the overall dimension of the plasma, typically of the order of one meter. A characteristic time scale of ideal MHD is set by the thermal velocity of the ions, i.e. $V_{Ti} = (2T_i/m_i)^{1/2}$. This is the fastest velocity at which the plasma as a whole can be moved. For typical tokamak fusion reactors, the magnetic field (B) is 5 T, typical temperature ($T_{i,e}$) 10 keV and density (n) $2 \times 10^{20}\mathrm{m}^{-3}$. Corresponding length and time scales for particle gyro motion as well as typical length and time scales of MHD phenomena are given in Table 2.1. In addition, a few other time scales which are needed in the derivation of ideal MHD equations are listed. The electron plasma period is the time that it takes for a charge separation to neutralise. For phenomena slower than the electron plasma period, the plasma can be considered quasineutral, i.e. the local electron and ion densities are equal. Electron collision time is the time that it takes to equilibrate particle energies to a Maxwellian distribution through collisions. The electron and ion temperatures are equilibrated (i.e. $T_e \approx T_i$) within the energy equilibriation time. Alfvé time is the time it takes for a hydrodynamic wave to move through the plasma. The growth time of MHD instabilities is often normalised to the the Alfvén time.

Table 2.1: Typical time and length scales of a tokamak plasmas. Deuterium ions are assumed.

Scale	Formula	Numerical value
Electron gyro radius	$r_e = (m_e T_e)^{1/2}/eB$	4.8×10^{-5} m
Ion gyro radius	$r_i = (m_i T_i)^{1/2}/eB$	2.9×10^{-3} m
Characteristic ideal MHD length	a	1 m
Electron plasma period	$\tau_{pe} = 2\pi(m_e \epsilon/ne^2)$	7.9×10^{-12} s
Debye length	$\lambda_d = V_{Te}/\omega_{pe}$	4.7×10^{-5} m
Electron gyro period	$\tau_{ce} = 2\pi m_e/eB$	7.1×10^{-12} s
Ion gyro period	$\tau_{ci} = 2\pi m_i/eB$	2.6×10^{-8} s
Electron-electron collision time	$\tau_{ee} = 7.4 \times 10^{-6} T_e^{3/2}/n$	1.2×10^{-4} s
Energy equilibration time	$\tau_{eq} = (m_i/2m_e)\tau_{ee}$	2.1×10^{-1} s
Alfvén time	$\tau_A = a(\mu_0 \rho)^{1/2}/B$	1.8×10^{-7} s

In the MHD theory, it is essential that the plasma is collisional, i.e. the particles interact frequently with each other. Without this assumption such quantities as temperature or pressure of the fluid element can not be defined. On the other hand, if ideal MHD is considered, plasma should not be too collisional, since it is assumed that the resistivity of the plasma is small. Low resistivity allows to neglect such phenomena as resistive diffusion and reconnection of magnetic field lines.

It turns out that the collision frequency in most plasmas of fusion interest is so low that the plasma can not be assumed collisional in the direction parallel to the magnetic field lines. This can be seen by comparing the electron-electron collision time with the ideal MHD time in Table 2.1. However, since the charged particles gyrate around magnetic field lines, they can be assumed to be "frozen" to the field lines. This means that, while the particle motion is very rapid in the parallel direction, gyro-averaged perpendicular particle motion is slow and, consequently, the collisional effects are fast compared with the transport across the field lines, so that the perpendicular behaviour can be treated with the fluid model. This allows treating most fusion plasmas with the ideal MHD theory in the direction perpendicular to the magnetic field.

The parallel direction has to be treated differently. In open-ended systems the parallel behaviour largely determines the overall confinement of the device. In toroidal systems, all parallel gradients disappear quickly due to the large parallel transport. The only parallel effect, the parallel sound waves, have usually very little effect on the macroscopic perpendicular instabilities. Consequently, extending the region of validity of the MHD model to lower collisionalities by considering only perpendicular phenomena is well justified.

However, at all times it is good to keep in mind the limitations of the MHD theory. For instance, if the particle orbit radius is comparable to the gradient lengths of the plasmas, averaging the particle position over the Larmor orbit is no longer justified and even the perpendicular MHD has reached its limit of validity. For instance, in the region near the tokamak plasma edge, where a steep pressure gradient exists, MHD theory is close to the limit of validity and some effects caused by the finite ion gyro radius start to play a role in the MHD stability of the plasma.

The detailed derivation of the ideal MHD equations starting from the particle picture

of the plasma is given in the Appendix. The equations are:

$$\frac{\partial \rho}{\partial t} + \nabla \cdot \rho \mathbf{v} = 0, \tag{2.1}$$

$$\rho \frac{d\mathbf{v}}{dt} - \mathbf{J} \times \mathbf{B} + \nabla p = 0, \tag{2.2}$$

$$\frac{d}{dt}\left(\frac{p}{\rho^{\gamma}}\right) = 0, \tag{2.3}$$

$$\mathbf{E} + \mathbf{v} \times \mathbf{B} = 0, \tag{2.4}$$

$$\nabla \times \mathbf{E} = -\frac{\partial \mathbf{B}}{\partial t}, \tag{2.5}$$

$$\nabla \times \mathbf{B} = \mu_0 \mathbf{J}, \tag{2.6}$$

$$\nabla \cdot \mathbf{B} = 0. \tag{2.7}$$

The restrictions for using these equations can be summed up by three conditions.

1. The ion gyro radius must be small compared with the characteristic length scale of the MHD phenomena.

2. The collisionality must be large in order to keep ion and electron temperatures equal and to ignore the viscous effects.

3. The resistivity must be small to avoid resistive diffusion.

The first and the third condition are satisfied for most plasmas that are interesting from the fusion point of view. Unfortunately, the second condition is not. The collisionality is too low for the particle motion parallel to the magnetic field lines to be treated accurately by ideal MHD. Fortunately, in toroidal devices, like the tokamak, this has little effect on the equilibrium and stability of the plasma. Consequently, the ideal MHD model for tokamak fusion plasmas can be used in most cases.

2.2 MHD equilibrium and stability

Macroscopic plasma instabilities are one of the key issues in the fusion research. Some instabilities can lead to a complete loss of confinement and naturally have to be avoided in a fusion reactor. Some instabilities cause less dramatic effects, but play an important role in the plasma performance. MHD theory is a useful tool for the study of all these instabilities. In this chapter, methods for reconstructing the plasma equilibrium and analysing the stability of the equilibrium are described.

2.2.1 Tokamak equilibrium

For a static plasma ($\mathbf{v} = 0$), the force balance in the ideal MHD momentum equation (2.2) gives:

$$\mathbf{j} \times \mathbf{B} = \nabla p. \tag{2.8}$$

Therefore, in the equilibrium $\mathbf{B} \cdot \nabla p = 0$, and there can be no pressure gradients parallel to the magnetic field. In a tokamak, the plasma pressure is the highest in the centre of the

plasma and the lowest at the edge. Consequently, the pressure gradient points from the edge to the centre everywhere, and the magnetic field has no radial (from the centre to the edge) component. Instead it forms nested surfaces that can be labelled, for instance, by their poloidal flux ψ_p that is defined as

$$\psi_p = \int_{A_{tor}} \mathbf{B} \cdot d\mathbf{A}, \tag{2.9}$$

where the integration is carried out in an arbitrary toroidal cross section A_{tor} that is bounded by the flux surface. Since the flux surfaces are nested, the poloidal flux value acts as a unique label for each flux surface. Therefore it can be used as a radial coordinate. In an axisymmetric device such as tokamak, the poloidal flux is a function of only two coordinates, the radial distance R from the toroidal axis and the vertical coordinate along the toroidal axis z.

Combining Eq. (2.8) with Ampere's law and using the axisymmetry of a tokamak, the plasma equilibrium is defined by a simple equation derived by Grad and Shafranov [18,19]

$$R\frac{\partial}{\partial R}\left(\frac{1}{R}\frac{\partial}{\partial R}\psi_p\right) + \frac{\partial^2 \psi_p}{\partial z^2} = -4\pi\mu_0 R^2 p'(\psi_p) - \mu_0^2 J(\psi_p) J'(\psi_p), \tag{2.10}$$

where p is the pressure, J is the poloidal current, and the prime denotes the derivative with respect to ψ_p. This equation can be solved for $\psi_p(R, z)$ that gives the magnetic configuration of the plasma. However, it must be noted that since on the right hand side both $p'(\psi_p)$ and $J(\psi_p)J'(\psi_p)$ are functions of the poloidal flux, the equation can generally be solved only iteratively. The pressure profile can be obtained from the temperature and density profile measurements, but there is no direct way to measure the poloidal current profile. Therefore, the current profile has to be reconstructed using indirect information. In most cases, most of the plasma current is driven inductively using the central solenoid. If the loop voltage created by the solenoid is not varied, the radial profile of the ohmic current can be assumed to be identical to the conductivity profile. In plasmas with a steep pressure gradient, in addition to the ohmic current the plasma itself can generate a current called bootstrap current. Next, the bootstrap current and its inclusion into the equilibrium calculation is described.

2.2.2 Bootstrap current

The bootstrap current is a parallel current driven by the plasma pressure gradient. It originates from the momentum transfer between trapped and passing particles. In a tokamak, the bootstrap current can contribute a significant part of the plasma current.

The bootstrap current was first predicted by Bickerton, Connor and Taylor in 1971 [20]. Since then, it has been observed in various experiments, like TFTR [21] and JET [22]. It is useful in advanced tokamak operation since it provides a way to drive plasma current non-inductively. In the edge stability and ELM physics, the bootstrap current plays an important role providing a mechanism to destabilise current-driven MHD instabilities.

The physical mechanism of the bootstrap current generation is briefly described below. A more complete presentation by Peeters can be found in Ref. [23].

Particle Drift Orbits

In a magnetised plasma, the particles move rapidly along the field lines. In the direction perpendicular to the magnetic field lines their motion is restricted to gyration around the field line. If there is a gradient in the magnetic field, the particles with a perpendicular velocity of $v_\perp$ drift with a velocity [1]

$$\mathbf{v}_d = \frac{1}{2}\rho_j v_\perp \mathbf{B} \times \nabla \mathbf{B}/B^2. \tag{2.11}$$

Here ρ_j is the gyro radius of the particle and it includes the sign of the charge, i.e. $\rho_j = m_j v_\perp/(e_j B)$. The toroidal magnetic field strength varies as $B \sim 1/R$, where R is the major radius. Since in a tokamak the magnetic field is predominantly in the toroidal direction, the gradient points to the centre of the device. Consequently, the direction of the drift is either up or down depending on the direction of the magnetic field and the charge of the particle.

The total energy and the so-called magnetic moment μ of the particle are conserved along its path. This means that if the strength of the magnetic field changes along the field line, it is possible that at some point the particle is reflected. This is seen from the definitions

$$E = \frac{1}{2}mv_\parallel^2 + \frac{1}{2}mv_\perp^2, \tag{2.12}$$

$$\mu = \frac{mv_\perp^2}{2B}. \tag{2.13}$$

$$\tag{2.14}$$

If the magnetic field increases, the perpendicular velocity also has to increase in order to keep the magnetic moment constant. Since the total energy does not change, this causes the parallel velocity to decrease. Once it becomes zero, the particle is reflected. Remembering that in a tokamak $B \sim 1/R$, the magnetic field strength increases as the particles follow the helical field lines and move towards the centre of the tokamak (decreasing R). In the poloidal plane, the reflection happens as shown in Fig. 2.1.

The particles that have enough parallel kinetic energy that they can complete circular orbits in the poloidal plane without being reflected are called *passing particles*. The particles that are reflected can not reach the high field side of the plasma and are thus called *trapped particles*.

Combining the drift caused by the magnetic field gradient and the reflections, the orbits in the poloidal plane look like in Fig. 2.2. Let us assume a particle with ∇B drift upwards and initial velocity downward on the outboard side of the equatorial plane. The particle starts its orbit from the midplane. As it moves downwards along the field line, it drifts upward because of ∇B. The drift causes it to move inwards from the original flux surface. If the particle does not have enough parallel velocity, it is reflected at some point. After the reflection, it moves upwards along the field line. The drift causes it to move further inwards until it reaches the midplane. After that the upward drift moves the particle towards its original flux surface. At some point, it is reflected again. Then it moves again downwards along the field line and the drift moves it outwards until it finally reaches the starting point. The particle with sufficient initial parallel velocity is not reflected, but it does experience the same inward drift below the midplane and outward drift above the midplane as the reflected particle.

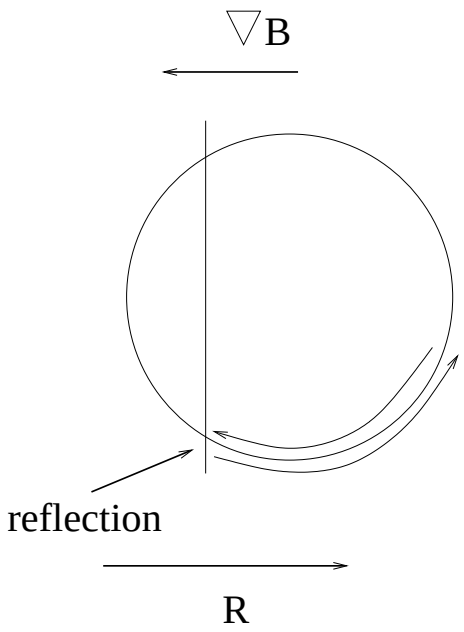

Figure 2.1: *Particle reflection in a torus with circular flux surfaces and* $B \sim 1/R$.

Because of the resulting orbit shape, the trapped particles are sometimes called banana particles. The width of the banana orbit is dependent on the initial parallel velocity and the poloidal magnetic field through the relation

$$\Delta r = v_{\|0} \frac{m_j}{e_j B_\theta}. \tag{2.15}$$

This is equal to the gyro radius calculated for a particle of the initial velocity $v_{\|0}$ at the midplane and magnetic field of $\mathbf{B}_\theta$. Therefore, it is often called the *poloidal gyro radius*.

Using the parallel and perpendicular components of the particle velocity on the outboard side of the midplane, the particle distribution can be displayed as in Fig. 2.3. The pitch is defined as $\frac{v_\|}{v}$ and the pitch angle as $\arccos \frac{v_\|}{v}$, where the velocities are taken at the outermost position of the particle orbit. The pitch determines whether the particle is trapped or passing. The trapped-passing border can be approximated for a plasma with circular cross-section. Since the magnetic moment is conserved,

$$\frac{v_\perp^2}{B} = \frac{v_{\perp 0}^2}{B}_{min}. \tag{2.16}$$

Since also the energy is conserved and at the reflection point $v_\| = 0$, it is possible to solve for the magnetic field at the reflection point (B_b) yielding the relation

$$\frac{B_b}{B_{min}} = 1 + \left(\frac{v_{\|0}}{v_{\perp 0}} \right)^2 \tag{2.17}$$

Since the magnetic field strength varies as $1/R$, the ratio of the maximum field to the minimum field at minor radius r can be written as

$$\frac{B_{max}}{B_{min}} = \frac{R_0 + r}{R_0 - r}, \tag{2.18}$$

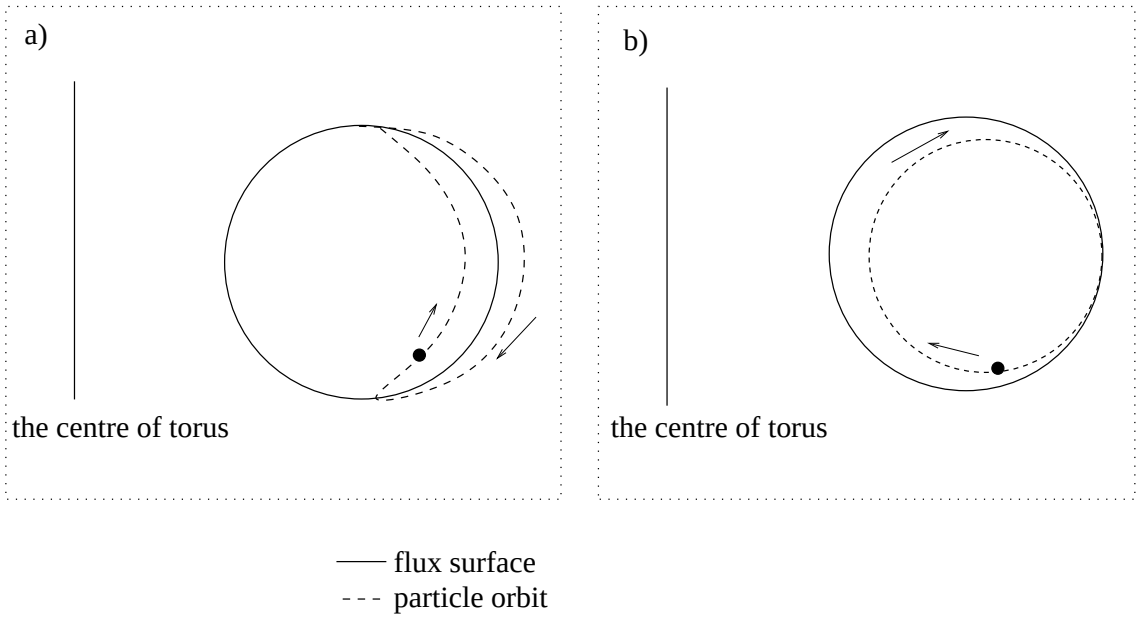

Figure 2.2: *Particle orbits in a tokamak: a) a banana orbit, b) a passing orbit*

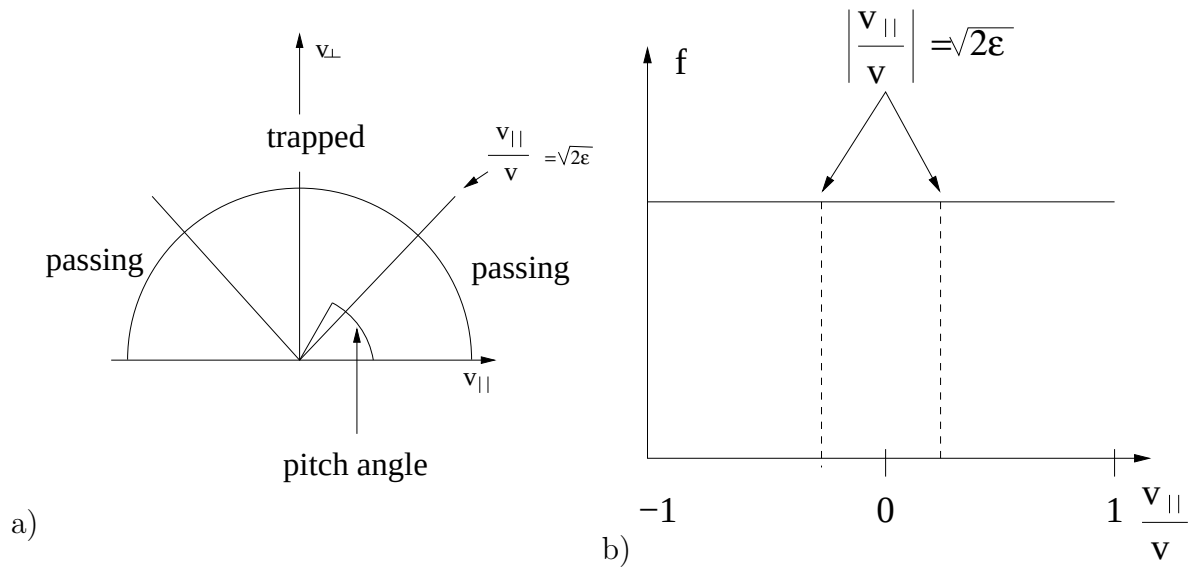

Figure 2.3: *Passing and trapped particles in the velocity plane for fixed energy. In a), the radius of the half circle represents the number of particles in that pitch ($v_\parallel/v$). In this case, the distribution is homogeneous and there are equal number of particles for every pitch. In b) the same distribution is shown with a pitch as the x-axis and the distribution as the y-axis. The borderline between the trapped and passing particles ($v_\parallel/v = \sqrt{2\epsilon}$) is shown in both pictures.*

where R_0 is the major radius of plasma. In order to have a reflection inside the plasma, a particle has to fulfil the condition $B_b < B_{max}$. Using Eqs. (2.18) and (2.17) this condition

can be written as

$$\left(\frac{v_{\parallel 0}}{v_{\perp 0}}\right) < \left(\frac{2r}{R_0 - r}\right)^{1/2}. \tag{2.19}$$

Using $v^2 = v_\parallel^2 + v_\perp^2$ the trapping boundary in velocity space can be written as

$$\left(\frac{v_{\parallel 0}}{v_0}\right)_{critical} = \left(\frac{2r}{R_0 + r}\right)^{1/2}. \tag{2.20}$$

Assuming large aspect ratio (R/r), the boundary can be approximated as

$$\left(\frac{v_{\parallel 0}}{v_0}\right)_{critical} = \sqrt{2\epsilon}, \tag{2.21}$$

where $\epsilon = r/R$.

Banana Current

If there is a pressure gradient in the plasma, the particles on banana orbits will generate current that is parallel to the plasma current. Next, the generation of this so-called banana current is explained.

Let us consider two particles on two adjacent banana orbits as in Fig. 2.4. At the point where the orbits touch, the particles are moving in opposite directions along the field lines. If there is a density gradient pointing left, there are more particles on the inner orbit than on the outer orbit at the touching point. This can be interpreted as "net velocity" in the direction of the particle on the inner orbit. Since the particles are charged, the net velocity means that current is flowing at this point.

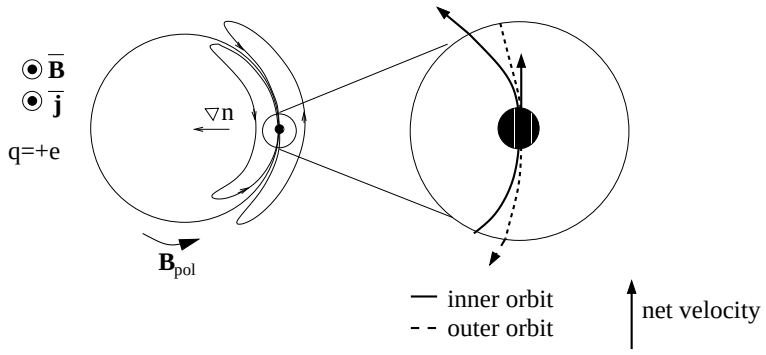

Figure 2.4: *Banana orbits that are touching each other result in net velocity parallel to the magnetic field in the presence of a density gradient.*

The average parallel velocity of trapped particles is approximately $v_{\parallel,tp} = \sqrt{\epsilon} v_{th}$. The trapped particle density can be approximated by $n_t = \sqrt{\epsilon} n$, where n is the total density. Assuming homogeneous temperature and recalling the width of a banana orbit given in Eq. (2.15), the net velocity at the point where the orbits meet is given by

$$n_j u_{\parallel j} \approx \frac{\sqrt{\epsilon} v_{th} m_j}{e B_p} \sqrt{\epsilon} v_{th} \sqrt{\epsilon} \frac{dn}{dr} = 2\epsilon^{3/2} \frac{1}{e B_p} T \frac{dn}{dr}, \tag{2.22}$$

where the relation $v_{th}^2 = 2T/m$ was used. When the electron and ion contributions are combined, the current density is obtained. Since the electrons drift in the direction opposite to the ion drift, the effects of ions and electrons on the parallel current add together

$$j = -enu_{\|e} + enu_{\|i} = 4\epsilon^{3/2}\frac{1}{B_p}T\left(\frac{dn}{dr}\right). \tag{2.23}$$

Here $n = n_e = n_i$ and $T = T_e = T_i$ is assumed. The direction of this current is parallel to the plasma current, if $dn/dr < 0$, which is true practically always in a tokamak plasma.

The net velocity can be interpreted as a shift in the distribution function towards the direction of the net velocity. In the velocity space this can be illustrated as in Fig. 2.5

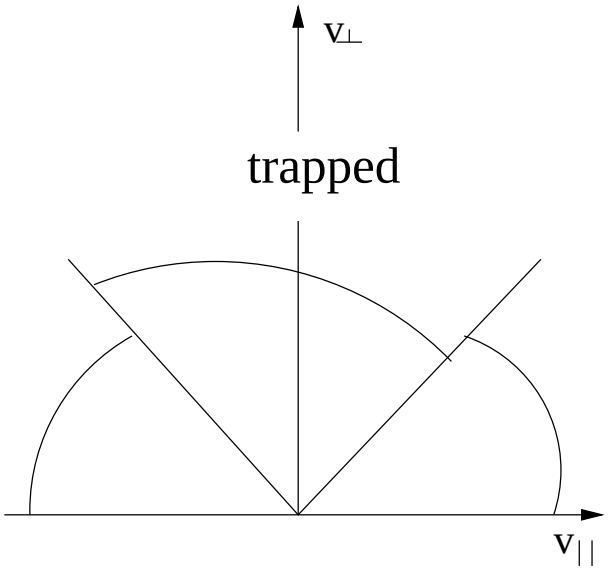

Figure 2.5: *The distortion of the trapped part of the distribution function due to the density gradient.*

In addition to the density gradient, also the temperature gradient contributes to the banana current. It can be explained as follows. If there is a temperature gradient, the particles that have higher temperature also have higher average parallel velocity. At the point where the orbits touch, the velocity difference between the orbits creates net parallel velocity just like in the case of a density gradient. Combining the net velocities of electrons and ions, a current is obtained. As with the density gradient, the direction of the current driven by the temperature gradient is parallel to the plasma current if $dT/dr < 0$, which is again fulfilled in a tokamak where the temperature decreases from the core to the edge.

Passing Particles and Bootstrap Current Generation

The passing particles do not stay on one flux surface along their path either, but unlike for the trapped particles, there is never ambiguity of the radial position of the particle at a given poloidal angle. Therefore, even in the presence of a density or temperature gradient, the passing particles do not contribute directly to the parallel current. However, due to collisions particles scatter from trapped to passing orbits and vice versa. This causes some

of the net parallel velocity of the trapped particles to be transferred to passing particles. After the collisions, the distribution function smooths as illustrated in Fig. 2.6. It can be seen that the entire distribution is shifted along the parallel velocity axis.

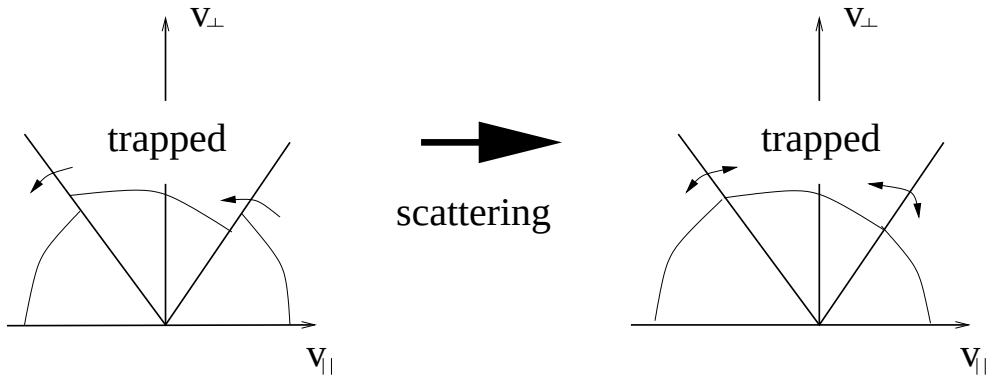

Figure 2.6: *Scattering smooths the velocity distribution function and shifts it in the parallel direction.*

In the end, the distribution functions of the electron and ion parallel velocities can be illustrated with Fig. 2.7. The electron distribution function has shifted in the direction opposite to that of the ion distribution function.

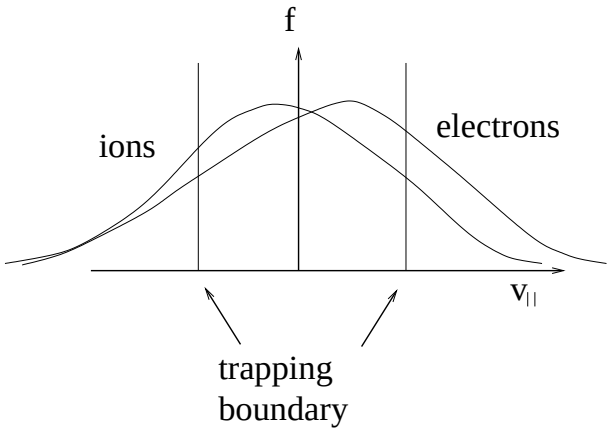

Figure 2.7: *The distribution functions of electrons and ions for parallel velocity.*

This is still not the full picture. The electron distribution is affected by collisions with much heavier ions, while the collisions with light electrons do not affect the ion distribution. The result is that the net electron velocity turns in the same direction with the ions. However, the velocity of the electrons remains smaller than that of the ions. The difference between the velocities can be interpreted as current. This current is called the *bootstrap current* and it is parallel to the magnetic field.

Bootstrap Current in Equilibrium Calculations

Since the bootstrap current is parallel to the magnetic field, it can not directly affect the force balance ($\mathbf{j} \times \mathbf{B} = \nabla p$). However, it changes the toroidal and poloidal current profiles

and influences the equilibrium through them. The bootstrap current can be taken into account when solving the equilibrium from the Grad-Shafranov equation in the following way.

A standard free-boundary, separatrix-defined equilibrium is determined as a solution of the Grad-Shafranov equation, Eq. (2.10). Instead of solving the poloidal flux, the equation can be written in the form of that defines the toroidal current density [1]:

$$j_t = \frac{\mu_0}{4\pi R}\frac{dJ^2}{d\psi_p} + 2\pi R\frac{dp}{d\psi_p}. \tag{2.24}$$

The standard way of calculating a plasma equilibrium is to assume functions $dJ^2/d\psi_p$ and $dp/d\psi_p$ known, and to solve the flux $\psi_p(R,Z)$ from Eq. (2.10) using iteration. The function $dp/d\psi_p$ can usually be obtained from the experiments, but the poloidal current function is generally not known. Therefore, some assumptions on the $dJ^2/d\psi_p$ term have to be made. One possibility is to make an educated guess for the shape of the profile (for instance, using diagnostic information on the q-profile), and then scale the magnitude so that $\int j_t dA = I_p$ is consistent with the experimental plasma current. The boundary value of J is also restricted by the condition $J_B = 2\pi R B_t/\mu_0$. However, this is a relatively crude method and usually can not recreate the smaller details of the actual current profile such as the pressure gradient dependent bootstrap current.

An equilibrium including the bootstrap current can be solved from Eq.(2.10) by expressing $dJ^2/d\psi_p$ in terms of the flux surface average $\langle\, \mathbf{j}\cdot\mathbf{B}\,\rangle/\mu J$. The averaged parallel current $\langle\, \mathbf{j}\cdot\mathbf{B}\,\rangle$ includes the inductively driven current, the bootstrap current, and all other possible externally driven currents. In the following, the externally driven currents are neglected and only inductive and bootstrap currents are considered. This is done only for simplicity. If the profile of the externally driven currents were known, they could be included in the formulation as well. The inductively driven contribution to $\langle\, \mathbf{j}\cdot\mathbf{B}\,\rangle/\mu J$ can be evaluated using the experimental resistivity profile, and the bootstrap current contribution can be obtained using an analytical formula from the neoclassical theory.

First, let us write out the flux surface average of a function Q as

$$\langle\, Q\,\rangle \equiv \int Q\frac{dS}{|\nabla V|} = \oint Q\frac{2\pi R}{|\nabla V|}ds. \tag{2.25}$$

Here, V is the volume inside a flux surface, S is the area of the flux surface and ds is a length element on the flux surface. They both are, of course, flux quantities. The integration is carried out on the poloidal plane along flux surface ψ_p.

Using the definition of the poloidal magnetic field, $\mathbf{B}_p = |\nabla\psi_p|/(2\pi R)\mathbf{x}_\theta$, and the Ampère's law, it is possible to derive an expression for the toroidal current. It can be written as

$$\begin{aligned}\mu_0 I &= \oint \mathbf{B}\cdot d\mathbf{s} = \oint \frac{|\nabla\psi_p|}{2\pi R}ds = \frac{d\psi_p}{dV}\oint \frac{|\nabla V|^2}{(2\pi R)^2}\frac{2\pi R}{|\nabla V|}ds \\ &= \frac{d\psi_p}{dV}\frac{1}{4\pi^2}\left\langle \frac{|\nabla V|^2}{R^2}\right\rangle.\end{aligned} \tag{2.26}$$

The flux surface averaged current $\langle\, \mathbf{j}\cdot\mathbf{B}\,\rangle$ can be written in two parts. Using the expression for the toroidal current (2.26) the poloidal contribution can be written as

$$\langle\, B_p j_p\,\rangle = \frac{1}{4\pi^2}\oint \frac{|\nabla\psi_p|}{2\pi R}\frac{|\nabla J|}{2\pi R}\frac{2\pi R}{|\nabla V|}ds$$

$$= \frac{dJ}{d\psi_p}\frac{d\psi_p}{dV}\oint \frac{|\nabla\psi_p|}{2\pi R}ds = \frac{dJ}{d\psi_p}\frac{d\psi_p}{dV}\mu_0 I = \frac{dJ}{d\psi_p}\mu_0 I^2 \frac{\mu_0 4\pi^2}{\langle\, |\nabla V|^2/R^2\,\rangle}. \qquad (2.27)$$

The toroidal magnetic field is given by $B_t = \mu J/(2\pi R)$. Multiplying this with the toroidal current density given in Eq. (2.24) and taking the surface average gives the toroidal contribution

$$\begin{aligned}\langle\, B_t j_t\,\rangle &= \left\langle \left(\frac{\mu_0}{4\pi R}\frac{dJ^2}{d\psi_p} + 2\pi R\frac{dp}{d\psi_p}\right)\frac{\mu_0 J}{2\pi R}\right\rangle \\ &= \frac{\mu_0^2}{4\pi^2}J^2\frac{dJ}{d\psi_p}\left\langle \frac{1}{R^2}\right\rangle + \mu_0\frac{dp}{d\psi_p}J. \qquad (2.28)\end{aligned}$$

Adding the poloidal and toroidal contributions of flux surface averaged parallel current together and combining terms yields

$$\langle\, \mathbf{j}\cdot\mathbf{B}\,\rangle = \langle\, B^2\,\rangle\frac{dJ}{d\psi_p} + \mu_0 J\frac{dp}{d\psi_p}, \qquad (2.29)$$

where $\langle\, B^2\,\rangle$ is the surface averaged squared magnetic field and its components are

$$\langle\, B^2\,\rangle = \mu_0(L_p J^2 + L_t I^2), \qquad \langle\, B_t^2\,\rangle = \mu_0 L_p J^2, \qquad \langle\, B_p^2\,\rangle = \mu_0 L_t I^2, \qquad (2.30)$$

where L_p and L_t are the poloidal and toroidal inductance coefficients

$$L_p \equiv \frac{\mu_0}{4\pi^2}\langle\, 1/R^2\,\rangle, \qquad L_t \equiv \frac{4\pi^2\mu_0}{\langle\, |\nabla V|^2/R^2\,\rangle}. \qquad (2.31)$$

Using (2.29) the expression $dJ/d\psi_p$ can be eliminated from the Eq. (2.24), and we obtain

$$j_t = 2\pi R\left\{\frac{B_t^2}{\langle\, B^2\,\rangle}\frac{\langle\, \mathbf{j}\cdot\mathbf{B}\,\rangle}{\mu_0 J} + \left(1 - \frac{B_t^2}{\langle\, B^2\,\rangle}\right)\frac{dp}{d\psi_p}\right\}. \qquad (2.32)$$

However, j_t still depends on J itself as well as on the toroidal current I (through $\langle\, B^2\,\rangle$). They can be solved, if $\langle\, \mathbf{j}\cdot\mathbf{B}\,\rangle/\mu_0 J$ and $dp/d\psi_p$ are given. Taking the flux surface average of (2.32), it is possible to write an equation for dI/dV. Similarly, taking (2.29), solving for $dJ/d\psi$ and using the definition of $\langle\, B_t^2\,\rangle$, (2.30), it is possible to write an equation for dJ/dV. These two ordinary differential equations are

$$\frac{dI}{dV} = \frac{\langle\, B_t^2\,\rangle}{\langle\, B^2\,\rangle}\frac{\langle\, \mathbf{j}\cdot\mathbf{B}\,\rangle}{\mu_0 J} + \left(1 - \frac{\langle\, B_t^2\,\rangle}{\langle\, B^2\,\rangle}\right)\frac{dp}{d\psi_p} \qquad (2.33)$$

$$\frac{1}{2}\frac{dJ^2}{dV} = L_R I\frac{\langle\, B_t^2\,\rangle}{\langle\, B^2\,\rangle}\left\{\frac{\langle\, \mathbf{j}\cdot\mathbf{B}\,\rangle}{\mu_0 J} - \frac{dp}{d\psi_p}\right\}. \qquad (2.34)$$

Here L_R is the ratio of the inductances L_t/L_p. The two differential equations for I and J have only terms containing $dp/d\psi$ and $\langle\, \mathbf{j}\cdot\mathbf{B}\,\rangle/\mu_0 J$.

Let us now consider the functions $\langle\, \mathbf{j}\cdot\mathbf{B}\,\rangle/\mu_0 J$ and $dp/d\psi_p$ as given, and $\langle\, B^2\,\rangle$ as defined by Eq. (2.30). The solution of the nonlinear two-point boundary value problem described by (2.33) and (2.34) leads to a complete determination of the right-hand side for the Grad-Shafranov equation, Eq. (2.10). For the solution, two boundary conditions are needed. It is conventional to choose $I = 0$ on the magnetic axis. On the plasma boundary, the poloidal current density has to vanish and, thus, $J_p^2 = (B_{t,vac}R_0)^2$.

If also the total plasma current I_p is prescribed (as the measured value), there are more boundary conditions than dependent variables, and therefore an additional free parameter C_s is needed. It is used to adjust the amount of parallel current contribution to the equilibrium through I and J (Eqs. (2.33) - (2.34)). In all equations, $\langle \mathbf{j}\cdot\mathbf{B} \rangle$ is replaced by $C_s \cdot \langle \mathbf{j}\cdot\mathbf{B} \rangle$, and the equations (2.33) and (2.34) are augmented by the differential equation

$$\frac{dC_s}{dV} = 0, \tag{2.35}$$

which means that the scaling of $\langle \mathbf{j}\cdot\mathbf{B} \rangle$ is constant throughout the plasma. Now there are 3 variables and 3 boundary conditions, and the boundary value problem has a unique solution.

In order to get the plasma equilibrium, instead of $dJ^2/d\psi_p$ now only the flux surface averaged parallel current ($\langle \mathbf{j}\cdot\mathbf{B} \rangle/\mu_0 J$) has to be prescribed, because $dJ^2/d\psi_p$ is obtained from the solution of the differential equations(2.33) - (2.35). Since analytical expressions for the flux surface averaged bootstrap current $\langle \mathbf{j}\cdot\mathbf{B} \rangle_{bs}/\mu_0 J$ exist, this makes the bootstrap current equilibrium reconstruction possible. Part of the parallel current is due to the inductively driven current $\langle \mathbf{j}\cdot\mathbf{B} \rangle_{ind}/\mu_0 J$. In a normal H-mode operation, where the current has diffused into equilibrium, the inductively driven current obeys the conductivity profile ($\sim T_e^{3/2}$) and can be considered known as well.

At first look, the free parameter C_s seems unphysical. However, since it multiplies the parallel current, it can be looked at as a varying loop voltage U that is used to control the total current in a tokamak. Since parallel current density is proportional to the loop voltage and conductivity σ as $j_\parallel \sim U\sigma$, purely inductive current can now be accurately solved in the equilibrium reconstruction by knowing the total current and the conductivity profile.

However, for bootstrap current, the situation is more complicated. In a general case $C_s \neq 1$, which means that, in the equilibrium, the parallel current is not equal to the value given by the neoclassical theory for the bootstrap current. However, if we use C_s to scale only the inductively driven part of the parallel current (and multiply the bootstrap current by 1), we retain the requirement of 3 variables and 3 boundary conditions for the unique solution, but at the same time obtain the correct bootstrap current. This is in fact exactly what is done in practise when a tokamak is operated. The loop voltage of the transformer is varied to match the total current with the preset value. This scales the inductively driven current but does not affect the bootstrap current.

Four analytical expressions for the bootstrap current $\langle \mathbf{j}\cdot\mathbf{B} \rangle_{bs}/\mu_0 J$ with slightly different assumptions on the geometry and the collisionality can be found in the literature: the Hirshman model and the Harris model, both in [24], the Wilson model in [25] and Sauter model in [26]. A common feature in all the models is that the bootstrap current can be expressed with a formula that depends only on the pressure and temperature profiles and the plasma shape. The profiles can be obtained from the experiments, and the plasma shape is solved in the iterative process of the equilibrium reconstruction. Combining the above boundary value problem, Eqs. (2.33) - (2.35), with the solving of the Grad-Shafranov equation allows self-consistent equilibrium reconstruction that takes into account the bootstrap current. The equilibrium is solved iteratively, solving the current profile using the previous equilibrium and the boundary value problem, and then solving for the new equilibrium using the new current profile.

While there are some differences in the results of the different models, the general behaviour is quite similar in all of them. In the experimental cases to be studied in later

chapters, the Wilson model is used for Type I ELMs in ASDEX Upgrade. In all the other analyses of ASDEX Upgrade plasmas, the more general Sauter model (that was published after the Type I ELM analyses were completed) is used. It should be noted that, in all the analyses where different equilibria are compared with each other, only one model is used consistently.

2.2.3 Important MHD equilibrium quantities

Before continuing, we define a few quantities that play an important role in the MHD stability analysis. They can be easily calculated once the equilibrium is solved.

One of the most crucial quantities affecting the tokamak plasma stability is the so-called safety factor or q that is defined as

$$q(\psi_p) = \frac{1}{2\pi} \oint \frac{rB_t ds}{RB_p}. \tag{2.36}$$

The integration is carried out on the poloidal plane along a flux surface ψ_p. In an ordinary H-mode tokamak equilibrium, the safety factor grows monotonically from the centre of the plasma towards the edge. If the plasma has a separatrix, the safety factor has a singularity there ($B_p = 0$ at x-point).

The q-value can be differentiated with respect to the radial co-ordinate r. This gives the magnetic shear that is defined as

$$s = \frac{dq}{dr}\frac{r}{q}. \tag{2.37}$$

The magnetic shear describes how the magnetic field lines are sheared from each other at a given location.

Another important quantity is the so-called β-value that measures the ratio of the plasma pressure to the magnetic pressure. It is defined as

$$\beta = \frac{p}{B^2/(2\mu_0)}, \tag{2.38}$$

where p is the pressure and B is the magnetic field. Instead of the above local definition of β, usually a global or volume averaged β-value is used.

In addition to the total β, a quantity called the poloidal β is defined as

$$\beta_p = \frac{2\mu_0 < p >}{< B_p^2 >}, \tag{2.39}$$

where B_p is the poloidal magnetic field. From the definition of β_p it is easy to see whether the tokamak is dia- or paramagnetic. If $\beta_p > 1$, the efficiency of the magnetic confinement is better than if only the poloidal field was present. This means that, in addition to the force $\mathbf{j}_t \times \mathbf{B}_p$, another inward pointing force exist. This is, of course, $\mathbf{j}_p \times \mathbf{B}_t$. In order for this vector to point inwards, the poloidal current has to be chosen so that it reduces the magnitude of the toroidal magnetic field. In this case, the plasma is diamagnetic. Conversely, if $\beta_p < 1$, the tokamak is paramagnetic, and the efficiency of the confinement is worse than if $\beta_p = 1$.

2.2.4 MHD instabilities

A hot plasma, with a large current running through it, is a large source of free energy. If the confinement of the plasma is lost, this energy is deposited onto the walls of the device in a very short time and can cause serious damage. Therefore, it is very important to keep the plasma stable so that a small perturbation from the equilibrium does not lead to a complete loss of confinement, a so-called disruption.

However, instabilities whose growth can be limited to a small region of the plasma, can be tolerated in the plasma operation. They increase the transport of particles and energy out of the plasma, but do not lead to a catastrophic end of a discharge. While the increase of energy transport always degrades the plasma confinement, sometimes the increase in particle transport can even be beneficial, for instance, to remove helium ash from the plasma. Increased transport due to small instabilities can also prevent other more destructive instabilities from developing. Examples of such non-catastrophic MHD instabilities are sawtooth crashes in the centre of the plasma and neo-classical tearing modes localised on surfaces with rational values of q. Also the ELMs studied in this thesis are in this category. They degrade the plasma confinement, but do not usually lead to a disruption. The plasma recovers after each ELM back to its previous state and stays there until the next ELM occurs.

In this section, the linear theory of the MHD stability is described. Two instabilities, peeling and ballooning modes, are considered more closely, because they play a crucial role in the ELM-model presented in Ch. 3.

The Concept of Stability

The equilibrium introduced earlier in Eq. (2.8) means that all forces in the system are balanced. However, it does not guarantee that the system will return to the equilibrium state if it is perturbed from it. If a small perturbation causes the system to depart further from the original equilibrium, the system is said to be unstable. If the system returns to the equilibrium after the perturbation, it is said to be stable. Figure 2.8 illustrates the mechanical equivalent of the stability and instability. If the system is at the border between stability and instability, it is called marginally stable.

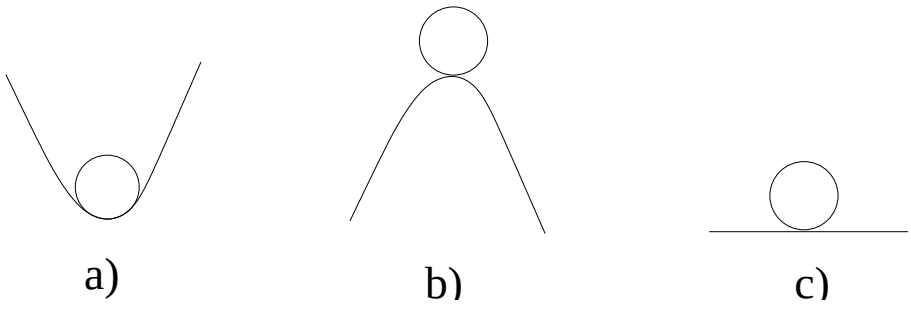

Figure 2.8: *a) A stable, b) an unstable, and c) a marginally stable equilibrium.*

In a stability analysis of a plasma, the plasma is assumed to be in an equilibrium, and it is disturbed by a small perturbation. The stability of the plasma is determined by its response to the perturbation. If the perturbation grows, the plasma is unstable. If

the perturbation only leads to oscillations near the equilibrium, the plasma is stable for the given perturbation. However, this determines only the stability against a particular perturbation. Only if the plasma is stable against all possible perturbations, it can be considered stable. Except for a few special cases, proving stability analytically is very difficult. Usually, numerical methods have to be used and, of course, the stability for infinite number of different perturbations can not be tested. Therefore, various approximations are used to simplify the analysis.

Linear Analysis

In the linear analysis, the equilibrium quantities, by definition, do not depend on time and are indicated by the subscript "0". The perturbed quantities are time-dependent and are marked with the subscript "1". The perturbed quantities are assumed to be much smaller than the equilibrium quantities, i.e. $Q(\mathbf{r},t) = Q_0(\mathbf{r}) + Q_1(\mathbf{r},t)$, $Q_1/Q_0 \ll 1$, where Q can be, for instance, the magnetic field $\mathbf{B}$ or pressure p. The linear analysis means that all terms that contain non-linear second order terms $(Q_1(\mathbf{r},t) \cdot Q_1(\mathbf{r},t))$ are considered so small that they can be neglected.

The perturbation of the plasma position, or the plasma displacement, is denoted with a vector $\boldsymbol{\xi}(\mathbf{r},t)$. In the equilibrium, the plasma velocity is zero, $\mathbf{v}_0 = 0$. The perturbed velocity is defined as

$$\mathbf{v}_1 = \frac{\partial \boldsymbol{\xi}}{\partial t}. \tag{2.40}$$

Neglecting the second order terms in the mass conservation equation (2.1), the energy relation (2.3), and in Faraday's law (2.7), and integrating with respect to time, we get

$$\begin{aligned} \rho_1 &= -\nabla \cdot (\rho_0 \boldsymbol{\xi}), \\ p_1 &= -\boldsymbol{\xi} \cdot p_0 - \gamma p_0 \nabla \cdot \boldsymbol{\xi}, \\ \mathbf{B}_1 &= \nabla \times (\boldsymbol{\xi} \times \mathbf{B}_0). \end{aligned} \tag{2.41}$$

Substituting these quantities into the momentum equation (2.2), gives

$$\rho_0 \frac{\partial^2 \boldsymbol{\xi}}{\partial t^2} = \mathbf{j}_0 \times \mathbf{B}_1 + \mathbf{j}_1 \times \mathbf{B}_0 - \nabla p_1 \equiv \mathbf{F}(\boldsymbol{\xi}), \tag{2.42}$$

$$\mathbf{F}(\boldsymbol{\xi}) = \frac{1}{\mu_0}(\nabla \times \mathbf{B}_0) \times \mathbf{B}_1 + \frac{1}{\mu_0}(\nabla \times \mathbf{B}_1) \times \mathbf{B}_0 + \nabla(\boldsymbol{\xi} \cdot \nabla p_0 + \gamma p_0 \nabla \cdot \boldsymbol{\xi}). \tag{2.43}$$

The function $\mathbf{F}(\boldsymbol{\xi})$ is called the force operator.

Equation (2.42) can be used to determine how the plasma state develops in time for a given perturbation. However, most of the time it is not the actual time development that is of interest, but only the stability of the plasma against all perturbations. Using Eq. (2.42) to test the plasma response to all possible perturbations is very difficult and better suited methods have to be used.

Eigenvalue Problem Formulation

The linear stability can be studied by assuming that the instabilities grow exponentially (because an exponential function is a solution to Eq. (2.42)). All perturbed quantities can then be written as

$$Q_1(\mathbf{r}, t) = Q_1(\mathbf{r})e^{-i\omega t}. \tag{2.44}$$

The perturbed momentum equation (2.42) now becomes

$$-\omega^2 \rho_0 \boldsymbol{\xi} = \mathbf{F}(\boldsymbol{\xi}). \tag{2.45}$$

Equation (2.45) can be treated as an eigenvalue problem for the eigenvalue ω^2. Once the eigenvalue is solved, the stability of the plasma is known. If ω^2 is negative, the plasma is unstable and, correspondingly, if it is positive, the plasma is stable. The transition from stability to instability occurs when $\omega^2 = 0$.

It can be shown [16] that the force operator is self-adjoint. This property allows to use the energy principle where the change of the potential energy of the system is minimised. Since the energy is conserved, a negative change of the potential energy corresponds a positive change in the plasma kinetic energy. This is naturally an unstable situation. Using the energy principle, the information about the growth rate of the instability is lost, but usually the determination of the stability is more important than the actual growth rate of the instability. The energy principle can be used by taking the inner product of Eq. (2.45) with $\boldsymbol{\xi}^*$ and integrating over the plasma volume, resulting

$$\omega^2 = \frac{\delta W(\boldsymbol{\xi}^*, \boldsymbol{\xi})}{K(\boldsymbol{\xi}^*, \boldsymbol{\xi})}, \tag{2.46}$$

where

$$\begin{aligned}
\delta W(\boldsymbol{\xi}^*, \boldsymbol{\xi}) &= -\frac{1}{2}\int \boldsymbol{\xi}^* \cdot \mathbf{F}(\boldsymbol{\xi}) d\mathbf{r} \\
&= -\frac{1}{2}\int \boldsymbol{\xi}^* \cdot \Big[\frac{1}{\mu_0}(\nabla \times \mathbf{B}_1) \times \mathbf{B}_0 + \frac{1}{\mu_0}(\nabla \times \mathbf{B}_0) \times \mathbf{B}_1 \\
&\quad + \nabla(\gamma p_0 \nabla \cdot \boldsymbol{\xi} + \boldsymbol{\xi} \cdot \nabla p_0)\Big] d\mathbf{r}, \\
K(\boldsymbol{\xi}^*, \boldsymbol{\xi}) &= \frac{1}{2}\int \rho_0 |\boldsymbol{\xi}|^2 d\mathbf{r}.
\end{aligned} \tag{2.47}$$

The function δW can be interpreted as the change in the potential energy associated with the perturbation $\boldsymbol{\xi}$. It is equal to the work done against the force $\mathbf{F}(\boldsymbol{\xi})$ with the displacement $\boldsymbol{\xi}$. The stability of the plasma can be determined from the change of the potential energy δW. Only if

$$\delta W(\boldsymbol{\xi}^*, \boldsymbol{\xi}) \geq 0 \tag{2.48}$$

for all perturbations, the plasma is stable. This is equivalent with the earlier condition $\omega^2 \geq 0$. If there exists any (allowable) perturbation that makes the potential energy negative, the plasma is unstable. So, in order to know the stability of the plasma, δW must be minimised with respect to $\boldsymbol{\xi}$. The minimum of δW then determines the stability.

Using the vector identities $\nabla \times (\mathbf{B} \times \mathbf{A}) = \mathbf{B} \cdot \nabla \times \mathbf{A} - \mathbf{A} \cdot \nabla \times \mathbf{B}$ and $\nabla \cdot (\phi \mathbf{A}) = \phi \nabla \cdot \mathbf{A} + \mathbf{A} \cdot (\nabla \phi)$ and the divergence theorem, the change of the potential energy can be written as

$$\begin{aligned} \delta W &= \frac{1}{2} \int d\mathbf{r} \left\{ \frac{|\mathbf{B}_1|^2}{\mu_0} + \gamma p_0 |\nabla \cdot \boldsymbol{\xi}|^2 - \boldsymbol{\xi}^* \cdot (\mathbf{j}_0 \times \mathbf{B}_1) + (\boldsymbol{\xi}^* \cdot \nabla p_0) \nabla \cdot \boldsymbol{\xi} \right\} \\ &\quad - \frac{1}{2} \int dS (\mathbf{n} \cdot \boldsymbol{\xi}^*) \left(p_1 - \frac{\mathbf{B}_0 \cdot \mathbf{B}_1}{\mu_0} \right), \end{aligned} \tag{2.49}$$

where $\mathbf{n}$ is the unit vector normal to the surface. If there is no vacuum region around the plasma, the surface term vanishes. With the vacuum region (but no surface currents or jumps in the pressure), this term can be written as

$$\delta W_{vacuum} = \frac{1}{2} \int_{vac} d\mathbf{r} \frac{|\mathbf{B}_1|^2}{\mu_0}, \tag{2.50}$$

and represents the energy transferred from plasma to the vacuum region.

The vacuum term is always positive definitive and, thus, stabilising. It is minimised by setting the change of the magnetic field in the vacuum region zero. If there are no currents at the boundary, all potentially destabilising effects are included in the fluid term and it will be looked at more carefully.

It has been shown [27] that the fluid term can be written in an intuitive form

$$\begin{aligned} \delta W_F &= \frac{1}{2} \int_{plasma} d\mathbf{r} \Bigg[\frac{|\mathbf{B}_{1,\perp}|^2}{\mu_0} + \frac{B_0^2}{\mu_0} |\nabla \cdot \boldsymbol{\xi}_\perp + 2 \boldsymbol{\xi}_\perp \cdot \boldsymbol{\kappa}|^2 + \gamma p_0 |\nabla \cdot \boldsymbol{\xi}|^2 \\ &\quad - 2 (\boldsymbol{\xi}_\perp \cdot \nabla p_0)(\boldsymbol{\kappa} \cdot \boldsymbol{\xi}_\perp^*) - j_\parallel (\boldsymbol{\xi}_\perp^* \times \mathbf{b}) \cdot \mathbf{B}_{1,\perp} \Bigg], \end{aligned} \tag{2.51}$$

where $\mathbf{b} = \mathbf{B}/B$, $\boldsymbol{\kappa}$ is the curvature vector of the magnetic field $\boldsymbol{\kappa} = \mathbf{b} \cdot \nabla \mathbf{b}$, and $\boldsymbol{\xi}_\perp$ is the component of $\boldsymbol{\xi}$ that is perpendicular to the equilibrium magnetic field. The terms can be interpreted as follows. The $|\mathbf{B}_{1,\perp}|^2$ term is the energy required to bend the magnetic field lines. The second term represents the energy required to compress the magnetic field. The third term is the compressional energy of the plasma. These three terms are always stabilising. The last two terms can be either stabilising or destabilising. The instabilities caused by the fourth term are called pressure-driven modes, because ∇p is the source of free energy. The last term represents current-driven modes. Here the source of free energy is the parallel current density $j_\parallel$.

Usually, the minimisation of δW has to be done using numerical methods. For that purpose the displacement $\boldsymbol{\xi}$ is often Fourier analysed and given in form

$$\boldsymbol{\xi}(\mathbf{r}) = \boldsymbol{\xi}(r) e^{i(m\theta + n\phi)}, \tag{2.52}$$

where m and n are called poloidal and toroidal mode numbers, respectively.

Before going to the numerical investigation of experimental plasmas, two important ideal MHD instabilities relevant to ELMs are discussed.

Peeling Modes

Peeling modes are kink-type instabilities occurring in the edge region of the plasma [28, 29]. In a peeling mode, the edge plasma 'peels' off from the rest of the plasma. The

destabilising free energy comes from the last term of (2.51) and, therefore, the peeling modes are said to be current driven modes. The peeling modes have typically low or intermediate toroidal mode numbers (n), i.e. $n = 1 - 10$. The poloidal mode number (m) depends on the rational surface at which the peeling mode is localized, so that $q = m/n$. Due to the low mode numbers, the wavelength is long.

From the fourth term of (2.51)) it is easy to see that if the average curvature on a flux surface is favourable ($\int[(\mathbf{b}\cdot\nabla\mathbf{b})\cdot\nabla p]d\mathbf{r} < 0$), the pressure gradient has stabilising effect on the peeling modes because there is little variation in $|\xi|$ with the poloidal angle due to the long wavelength.

In the H-mode plasma edge, the turbulence is suppressed and a steep pressure gradient builds up. The steep gradient region is often called the pedestal region. As described in section 2.2.2, a pressure gradient generates bootstrap current. Therefore, in the pedestal region, there is also higher current density than in the surrounding plasma. The destabilising potential energy is localized to the edge region, where the current density gradient is large and, consequently, also the instability is localized to this region. The simplified radial structure of a perturbation that destabilises peeling modes is shown in Fig. 2.9. The instability increases the plasma transport at the edge, and causes the pressure profile to flatten. The edge current density drops due to lowered conductivity and decreased bootstrap current (proportional to the pressure gradient). As the edge current density gradient decreases below the stability limit, the plasma is stabilised again. The peeling mode effects are usually limited to affect only the edge region.

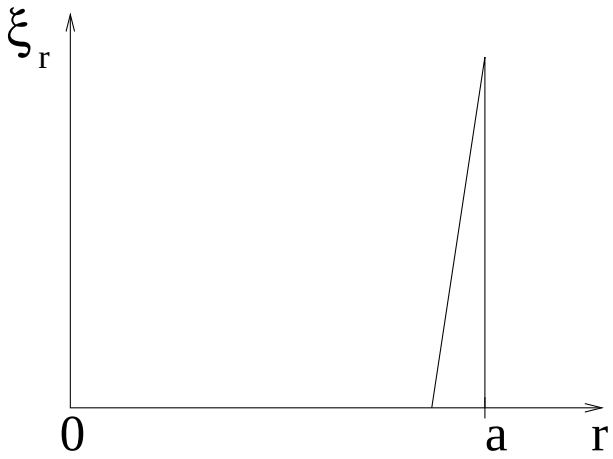

Figure 2.9: *The radial structure of a perturbation that can destabilise peeling modes.*

Ballooning Modes

The ballooning modes are pressure-driven instabilities that can only occur in a toroidal device. The destabilising energy comes from the fourth term of Eq. (2.51). The modes are localized to the region of unfavourable curvature (the curvature of the plasma and the pressure gradient point in the same direction, i.e., $(\mathbf{b}\cdot\nabla\mathbf{b})\cdot\nabla p > 0$) in order to minimise the stabilising effect of the favourable curvature. Figure 2.10 shows a typical mode structure for a perturbation that destabilises a ballooning mode. In order to be localised on the unfavourable curvature region, the amplitude variation along the field

line must be maximised. Therefore, the most unstable ballooning modes typically have high toroidal mode numbers [30]. The mode structure is such that there are very fine structures in the poloidal direction, but in the toroidal direction the wavelength is long. In a tokamak, the toroidal magnetic field is much stronger than the poloidal field. Thus, along the magnetic field line, the mode structure changes slowly, and the stabilising energy from the field line bending is minimised.

In determining stability against ballooning modes, the stabilising field line bending and the destabilising fourth term of (2.51) (pressure gradient drive) compete with each other. For circular plasmas, this means that the ballooning modes are stabilised by the shear of the magnetic field ($s = rq'/q$). The stabilising effect can be understood by following two magnetic field lines that are only slightly apart in the radial direction. Therefore the mode structure must be almost the same on both field lines. As the field lines are followed around the torus, if there is shear in the magnetic field, the distance between field lines starts growing. This means that in regions of strong shear the mode can not be entirely localized on the unfavourable side and the destabilising energy is reduced. On the other hand, low shear allows larger radial mode structures to stay together on adjacent field lines. The net effect is that the increasing magnetic shear raises the ballooning stability limit for given pressure gradient.

It turns out that in addition the stable region of high shear and low pressure gradient, there is a second region of stability as well [80]. This stable region has very low shear and high pressure gradient. The reason for this so-called second stable region is the following. What stabilises the ballooning mode is not actually the global shear, but the local shear in the region where the ballooning mode is localised. This region is the outboard side of the midplane, since there the magnetic shear is most unfavourable. When the global shear is lowered close to zero, the shear on the outboard side becomes negative. The more the local shear varies between the inboard and outboard sides of the flux surface, the more negative the outboard side shear becomes. Since the local shear is determined by the local toroidal current density (the higher the current density, the lower the shear), a large variation of toroidal current density on a flux surface creates also a large variation of the local shear. Recalling from Eq. (2.24) that $j_t \sim Rp'$, we can see that a large pressure gradient creates a large variation of the local shear on a flux surface. Therefore, when the global shear is close to zero, the stability of the plasma against the ballooning modes is improved by increasing the pressure gradient. Unfortunately, the access from the high shear low pressure gradient region to the second stability region for circular plasmas is closed, i.e. there is an unstable region between the two stable regions, see Fig. 2.11

Plasma shaping changes this situation. For strongly shaped plasmas, low shear can open the access to the region of high pressure gradient with ballooning stability. The reason for the stabilising effect of the plasma shaping is the following. If we follow a magnetic field line once around the poloidal plane, in plasma with circular cross-section, the distance the field covers in the region where the curvature is favourable is the about the same as in the region where the curvature is unfavourable. The average curvature is then neither favourable nor unfavourable. In carefully shaped plasma, however, it possible that the distance covered in the region of favourable curvature is longer than in the region of unfavourable curvature. The average curvature is favourable which improves the plasma stability against the ballooning modes. An example of the shaping that makes the average curvature more favourable is the increase of the plasma triangularity.

A numerical analysis of the ballooning stability yields a stability diagram depicted in

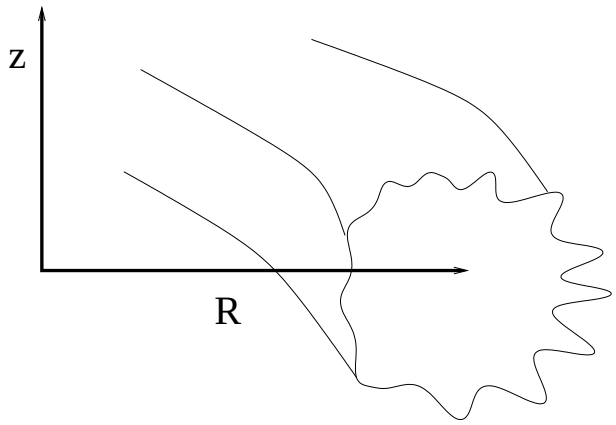

Figure 2.10: *The mode structure of a ballooning mode. The mode is localized to the unfavourable region (low magnetic field side) of the plasma.*

Fig. 2.11. For circular plasmas, there is no access from the first stable region (low p', high s) to the second stable region (high p', low s), but when the plasma is strongly shaped (increased elongation and triangularity) [31], the stable regions become connected and the access to the second stable region is opened. The access to the second stable region would make it possible to achieve high pressure values, and to operate the tokamak with high β. The second stability access also plays a role in the edge stability and affects the ELMs.

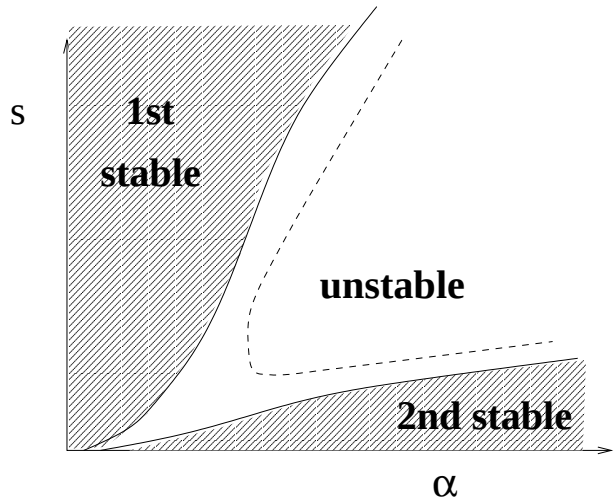

Figure 2.11: *Stability diagram of the ballooning mode [1]. The quantity* $\alpha = -(2\mu_0 r^2 p')/(R_0 B_{pol}^2)$ *is a measure of the pressure gradient, and* $s = rq'/q$ *is the average magnetic shear. The shaded area on the left is the first stable region, and the shaded region on the right is the second stable region. The dashed line represents a case where the access to the second stability region is opened.*

2.2.5 Numerical tools

Several codes have been developed for both solving the plasma equilibrium and analysing the stability of the equilibrium against MHD instabilities. In this thesis, GRETA code that uses the methods described in Sec. 2.2.2 for the self-consistent equilibrium calculation is used for ASDEX Upgrade plasmas. In GRETA, the plasma boundary is determined by the poloidal field coil currents. For JET plasmas, JETTO [32] code is used. JETTO is a transport code for energy, particles and current. In this case, the temperature and density profiles are kept fixed to the experimental ones and the current is allowed to diffuse to an equilibrium.

The stability against modes with low to intermediate toroidal mode numbers (n) is analysed using GATO [33] and MISHKA [34]. GATO is used to analyse ASDEX Upgrade plasmas and MISHKA to analyse JET plasmas. The codes use slightly different numerical approaches to the stability problem, but the basic idea is the same in both codes.

The codes solve for the ideal stability of the plasma in the following way. The starting point is the minimisation of the potential energy given by Eq. (2.49). By using a Galerkin-type expansion, the perturbation can be written as $\xi = \sum_i a_i \phi_i(\mathbf{x})$, where $\phi_i(\mathbf{x})$ are the finite elements at location $\mathbf{x}$. It is then possible to minimise δW by setting $\partial \delta W / \partial a_i = 0$. By discretising the plasma on a grid, the eigenvalue problem (Eq. (2.46)) is now transformed into a matrix form $AV = \omega^2 BV$, where A and B are matrix representations of W and K, and V is the vector of coefficients a_i. The solution to the matrix eigenvalue problem is obtained by ordinary matrix inversion. From the point of view of computing this part is the most demanding. The details of the numerical optimisation are, however, beyond the scope of this thesis.

GATO runs are typically carried out on a 160x320 or 200x400 grid in order to achieve sufficient convergence. The solution for the most unstable displacement ξ can be Fourier analysed ($\xi(\mathbf{x}) = \xi(r)e^{-i(n\phi+m\theta)}$, where n and m are the toroidal and poloidal mode numbers).

For MISHKA runs, the number of poloidal harmonics and radial grid points are specified. In most cases, 100 radial points are sufficient for convergence, but with very localised modes with high n, 200 radial points are used. The needed number of poloidal harmonics m depends on the investigated toroidal mode number n and the safety factor at the edge q_a with the relation m=nq_a. Both codes can pack radial grid points in the region of interest, for instance, near rational flux surfaces or the edge of the plasma.

A few selected equilibria have been analysed using both codes for edge instabilities [35]. It was found that at low toroidal mode numbers results agreed reasonably well, but as the mode number increased, the results started to diverge from each other. It is still unclear, whether the reason for differences is in the transform of the equilibria, which is not straightforward near the separatrix, or in the stability codes themselves.

The n=∞ ballooning stability is studied using GRETA (Type I ELMs in ASDEX Upgrade) and IDBALL (all other cases). Both codes use similar methodology by expanding the eigenfunction in powers of 1/n [36]. The expansion allows solving for the ballooning stability independently on each flux surface and is therefore considerably faster than the low-n analyses with GATO or MISHKA.

Chapter 3

Edge Localized Modes

3.1 Introduction

The simplest way to consider the transport of particles and energy perpendicular to the magnetic field lines is to consider a linear device with a modest temperature gradient. Due to collisions particles on adjacent gyro orbits exchange energy, and heat is transported from the hot centre of the plasma to the cold edge. This is called "classical" transport. In a torus, transport is enhanced by the banana orbits that are much wider than the gyro orbits. Consequently, the collisional transport in a torus is higher than the classical transport and it is called "neo-classical" transport. Since collisions are always present, the confinement in a tokamak can never exceed the neo-classical level. The ions in plasmas with only ohmic heating can reach the neo-classical confinement regime.

However, when the plasma is externally heated and the temperature gradient becomes steeper, the confinement becomes significantly worse due to the so-called "anomalous" transport. Compared to classical or neo-classical transport, it is usually orders of magnitude faster. The anomalous transport is driven by plasma turbulence. The plasma operating regime where anomalous transport is dominating throughout the plasma is called low confinement mode or L-mode.

A great advance in tokamak research was made, when it was discovered that increasing heating of the plasma above a certain threshold improves the confinement considerably [37]. The turbulence then becomes suppressed in the edge region. Since the confinement improvement is not global, the region where turbulence is suppressed is called a transport barrier. The improved confinement operating regime is called high confinement mode or H-mode.

In H-mode plasmas, short periodic bursts of plasma are often observed. They are called Edge Localized Modes or ELMs. The ELMs are usually detected most easily by the increased radiation coming from the divertor region (the so-called divertor D_α-radiation). The radiation is produced when the particles released from the edge plasma during the ELM burst collide with neutral atoms that are abundant near the divertor. The collisions excite the atoms and their de-excitation is observed as radiation. Figure 3.1 shows ELMs in a typical H-mode shot in ASDEX Upgrade. In addition to the D_α-signal, the ELMs manifest themselves in the edge line-averaged density from the laser-interferometer and the electron temperature on the top of the edge transport barrier from electron cyclotron emission measurements. As can be seen in the figure, when an ELM occurs, the plasma confinement in the edge region is lost and the temperature and density on the top of the

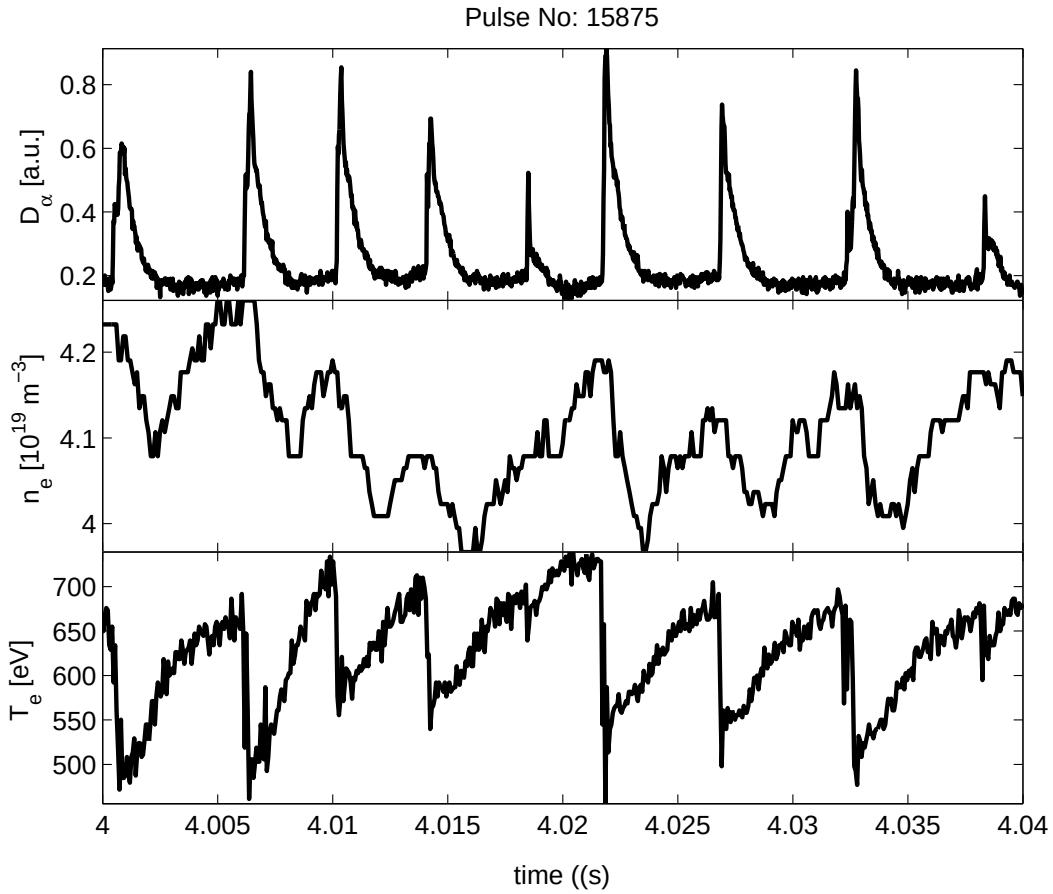

Figure 3.1: *The D_α-signal together with line-averaged electron edge density and electron temperature at radius $\rho = 0.97$, ($\rho = \sqrt{\psi_N}$, ψ_N is the normalised poloidal flux) of ASDEX Upgrade discharge #15875. Each peak in the D_α-signal represents an ELM.*

edge transport barrier decrease rapidly followed by a slow recovery.

The ELM crash does not usually disturb the confinement in the core plasma as can be seen in Fig. 3.2, where the relative change in electron temperature caused by the ELM crash is plotted as a function of radius. However, in advanced tokamak operation with an internal transport barrier (ITB), a large ELM can cause the loss of the barrier.

3.2 The importance of the ELM phenomenon

The ELMs have a degrading effect on the plasma confinement but, on the other hand, they help to remove impurities and helium ash from the plasma. They also prevent the density of the plasma from rising too high and causing a disruption. Stationary and clean H-mode plasmas without ELMs have been difficult to achieve. Even though in ELMy H-mode it is not possible to keep the confinement as high as in some ELM-free operations, like the hot-ion mode in JET [11], its stable steady state operation and good impurity exhaust in long pulses are superior to other operating regimes. Therefore, ELMy H-mode has been chosen as the standard operating mode for ITER.

Probably the most harmful consequence of the ELMs is the erosion of the divertor

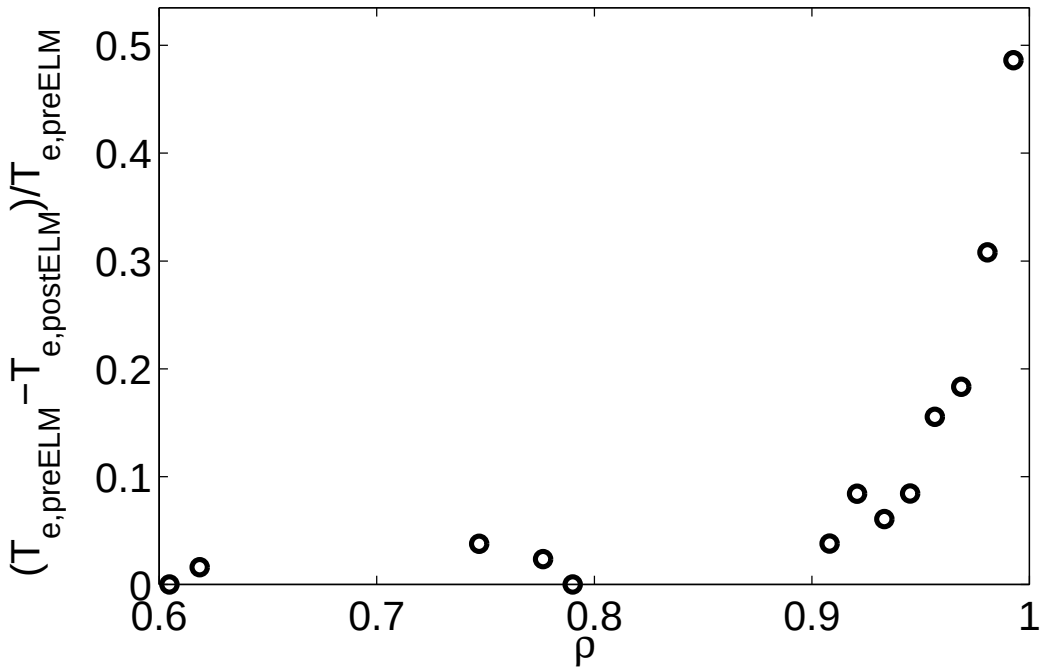

Figure 3.2: *Relative change in the electron temperature during an ELM. Fast ECE measurements for discharge #15875 on ASDEX Upgrade at 4.010 s and 4.011 s have been used to calculate the radial profile of* $(T_{e,preELM} - T_{e,postELM}/T_{e,preELM})$.

plates. From the point of view of the lifetime of the divertor plates, the ELM bursts are much more destructive than the continuous flow of particles and energy. In ITER, the ELM energy may exceed the threshold for divertor target ablation by a factor of 5 [12]. Therefore, reducing the ELM peak power load or getting rid of the ELMs altogether without sacrificing the control of the density and sufficient helium exhaust are important goals that have to be reached on the way to a fusion reactor.

In addition to tokamaks, ELMs have also been observed in stellarator and spherical tokamak H-mode plasmas [13, 14]. Thus it looks like that the problems associated with the ELMs have to be solved even if one of these alternatives to a tokamak turns out to be better concept for harnessing the fusion energy.

It is also interesting to note that solar flares have been found to display similar MHD instability properties as ELMs [15].

3.3 ELM cycle

The periodic nature of the ELM phenomenon makes it possible to investigate a single ELM cycle and generalise it to the behaviour of the entire ELM phenomenon.

The most rapid changes occur naturally during the ELM crash (typically a few hundred microseconds [47]) that is usually significantly shorter than the time between the ELMs (several milliseconds, as can be seen in Fig. 3.1). A schematic description of the ELM burst is shown in Fig. 3.3, where the poloidal plasma cross-section, the plasma pressure profile and the D_α radiation from the divertor region are shown at four different time

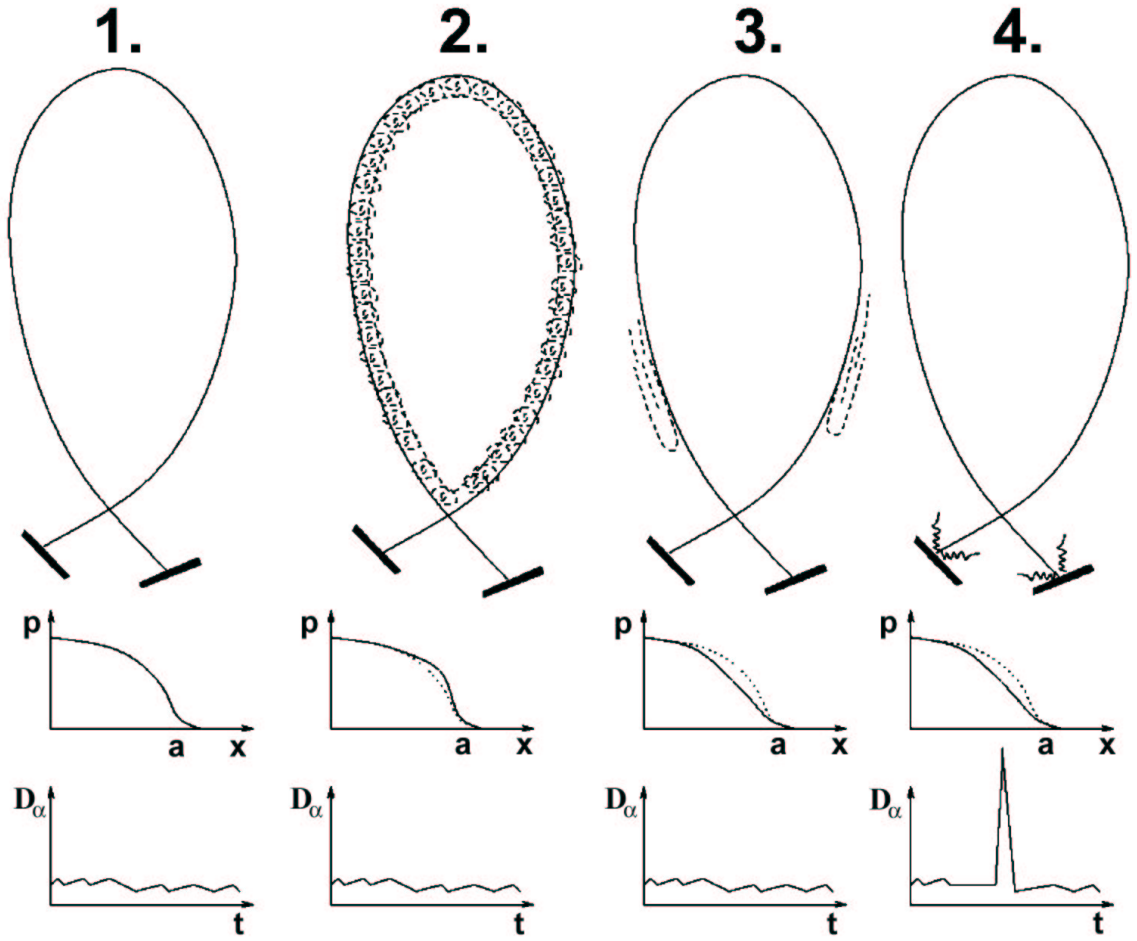

Figure 3.3: *ELM cycle from the build-up of the edge pressure gradient (1) to the triggering of the instability (2), the loss of the edge plasma (3) and the detection of the increased D_α-radiation from the divertor region (4).*

points during the cycle. The first picture shows the situation before the ELM crash. The plasma is stable and has a steep pressure gradient at the edge. The gradient is maintained by the edge transport barrier that is always associated with the H-mode. The second picture shows the onset of an ELM. The pressure gradient exceeds a critical value for the stability of the edge plasma. The instability is not necessarily driven by the pressure gradient itself but, for instance, the pressure gradient can drive the bootstrap current (as explained in the previous chapter) and the instability is triggered by the parallel edge current.

Once the instability takes place, the confinement of the edge plasma is lost. The lost plasma flows along the field lines (the third picture) and ends up on the divertor plates producing a distinctive peak in the D_α-signal (the fourth picture). During the instability, the edge pressure gradient is reduced until the plasma becomes stable again. Then the pressure gradient starts recovering until it reaches the stability limit again and another ELM occurs. If the conditions stay constant, the cycle can continue infinitely. Each cycle removes generally a few per cents of the plasma energy and particles.

3.4 Classification of ELMs

While some of the features are common to all ELMy plasmas, there are also qualitative differences between them. Consequently, it has become customary to classify ELMs into three separate types. In ELM physics, the following classification scheme, first given by Doyle et al. [38], is usually used:

- Type I ELMs: The D_α-signal shows large isolated bursts and, therefore, Type I ELMs are also called 'giant' ELMs. The plasma edge is close to the ideal ballooning stability limit or even beyond it. As the heating power is increased, the ELM repetition frequency also increases. The time-averaged degradation of the edge plasma confinement is smaller than with other ELM types.

- Type II ELMs: These are observed only in strongly-shaped (high elongation and triangularity) plasmas. The magnitude of the ELM bursts is lower and the frequency is higher than that of Type I ELMs, while the confinement stays almost as good as in Type I ELMy plasmas. Due to the strong shaping, the plasma is in the connection regime between the so-called first and the second ballooning stability regions (explained in more detail in Sec. 2.2). Sometimes, Type II ELMs are called 'grassy' ELMs.

- Type III ELMs: The bursts are small and frequent. Therefore, another name for Type III ELMs is 'small' ELMs. The repetition frequency is found to decrease with the heating power. The plasma confinement is degraded more than with other ELMs. The edge plasma pressure can be well below the ballooning stability limit.

In addition to the above ELMy operating regimes two ELM-free operating modes with stable density have been observed.

- In Alcator C-MOD, the so-called enhanced D_α-mode or EDA is observed [40, 41]. In EDA, while the plasma behaves like in ELMy H-mode (steady-state density, no accumulation of impurities), no periodic bursts of plasma exist, but instead the D_α-radiation remains at an increased level throughout the EDA-period. The particle and energy confinement is poorer than in true ELM-free H-mode. The conditions for EDA resemble that of Type II ELMs [41].

- In DIII-D and ASDEX Upgrade, the so-called quiescent H-mode (QHM) has been achieved [42, 44]. In the quiescent H-mode, the ELMs become suppressed and, instead, harmonic oscillations are observed in the plasma edge. They are signs of other MHD activity that keeps the particle transport high. The high particle transport keeps the density in control and avoids the typical problem of an ELM-free H-mode where the plasma density uncontrollably increases and the discharges ends with a disruption. In DIII-D, the quiescent operating mode has also been successfully combined with improved core confinement, which led to the so-called quiescent double barrier mode [45, 46]

In ASDEX Upgrade, different types of ELMs have been found to correspond to different plasma edge parameters [39]. Figure 3.4 shows schematically the ELM classification in $T_{edge} - n_{edge}$ space, with the addition of the above-mentioned QHM and EDA regimes. The edge temperature and density refer to the values on the top of the H-mode barrier.

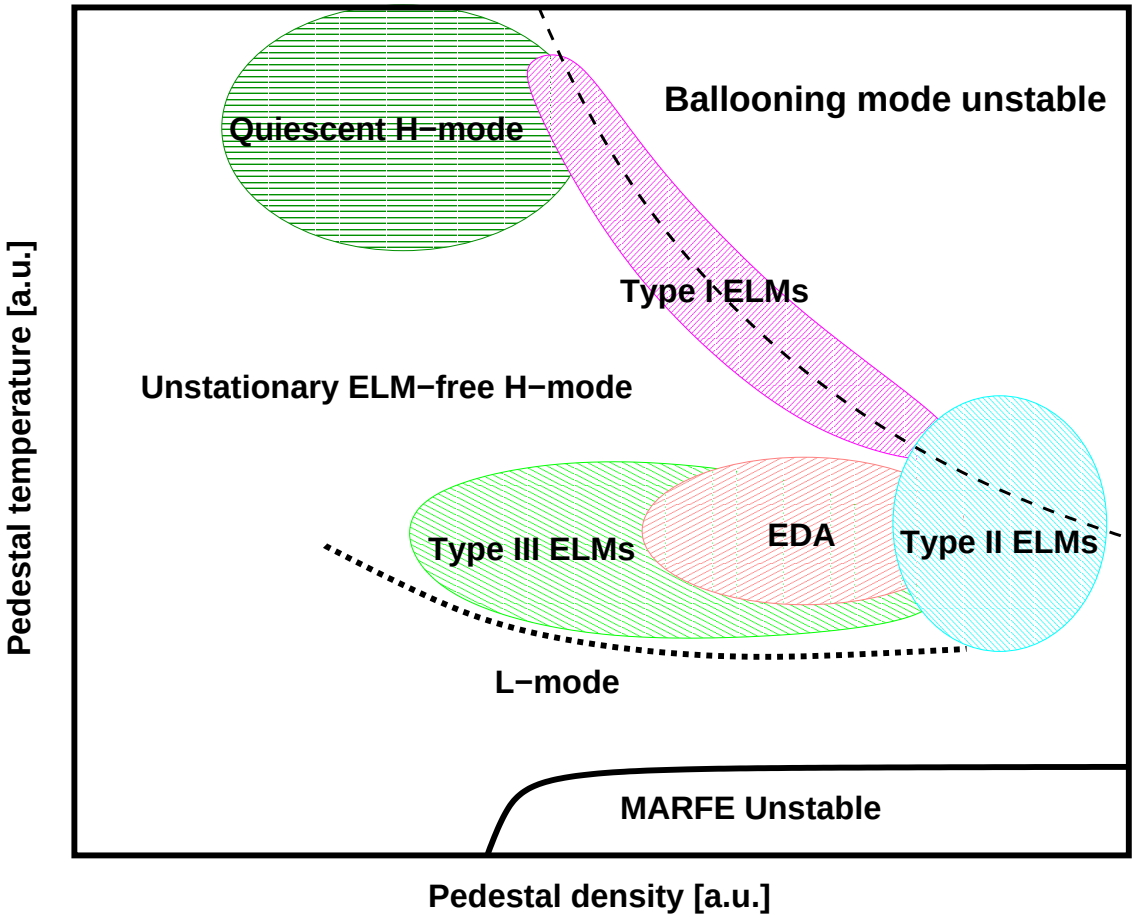

Figure 3.4: *A schematic view of different ELMy and ELM-like regimes in the pedestal temperature-density space. The numerical values of temperature and density for different regimes vary between plasma devices. Also other factors such as plasma shaping affect the access to different regimes.*

The lower limit for the temperature at high density (labelled "MARFE unstable") is caused by the radiation cooling of the edge plasma and is inaccessible operating regime.

3.5 ELM precursors

During the ELM cycle, magnetic fluctuations are observed before the main ELM crash. The fluctuations, also called precursors, differ between ELM types, which suggests that the instabilities behind the ELMs themselves can be different. In ASDEX Upgrade, the precursors are seen most clearly with Type III ELMs, but they have also been observed with Type I and Type II ELMs. The Type III ELM precursor frequency varies around 50-150 kHz and the observed toroidal mode numbers n are of the order 10-15 [47,48]. For type I ELMs frequencies of about 5-20 kHz and mode numbers n=5-10 are observed. In addition, higher frequency modes ($\nu \approx 75-145$ kHz) with n=3-5 [49] and $\nu \approx$300 kHz [50] have been associated with the MHD activity occurring before an ELM. An example of the magnetic signal of the high frequency activity and its frequency spectrum is shown

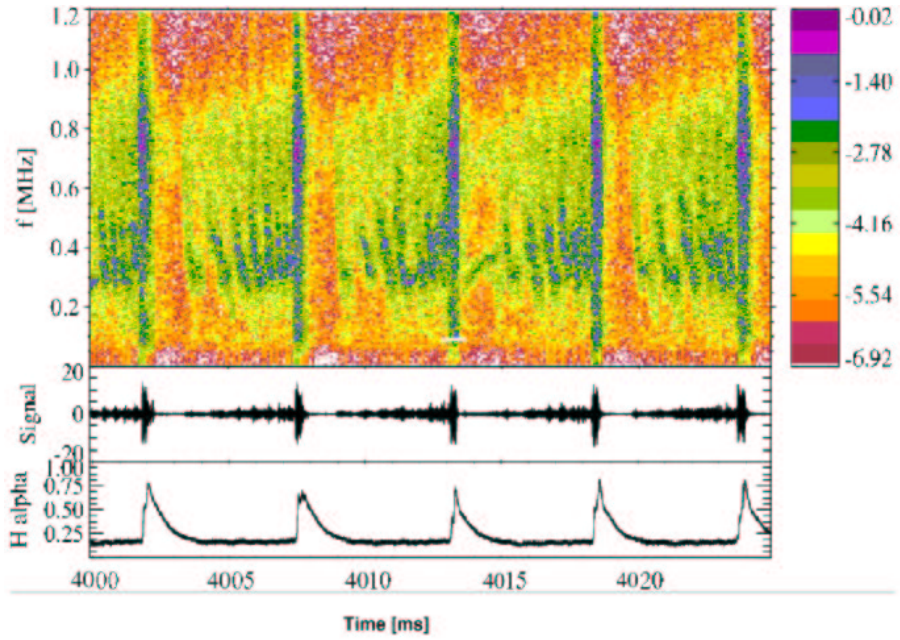

Figure 3.5: *The magnetic frequency spectrum from the Mirnov coils of the ASDEX Upgrade shot #15875 (Type I ELMs). The D_α-signal on the bottom shows the occurrence of the ELMs. Magnetic precursor activity can be seen between 300 and 600 kHz*

in Fig. 3.5. The precursors observed with Type II ELM have frequency of about 30 kHz. Typical toroidal mode numbers n are of the order of 3-4.

In JET, Type I ELM precursors at the frequency of about 20 kHz and mode numbers of 1-13 have been observed [51]. The lower mode numbers seem to be associated with lower values of collisionality in the edge region and high mode numbers with high collisionality. In addition to the precursors, the Type I ELM phenomenon has also been associated with the so-called washboard mode activity (bands of fluctuating magnetic activity rotating in the direction of the electron diamagnetic drift with typical frequencies in the range of 10-90 kHz) [52]. The washboard modes have also been observed with mixed Type I/Type II ELMs [52].

While the exact relationship between the precursors and the ELM crash itself is still not clear, the precursors can be used to obtain fundamental information on the underlying mechanisms for the ELMs. The mode numbers give insight to the mode structure of the instability that is responsible for the ELM. Therefore, to validate a theoretical model for the ELMs, its predictions have to be compared against the information obtained from the precursor observations.

3.6 The Connor-Wilson model for the ELMs

Several models for ELMs have been suggested (see Ref. [53] for a comprehensive summary of models). One class of models use MHD instabilities to explain the ELMy behaviour in the plasma. Both ideal [54] and resistive [55] instabilities have been considered. The basic idea in these models is that the plasma goes through a cycle where it is destabilised

by some instability causing an ELM. The ELM enhances the transport in the edge region, the pressure gradient is relaxed and the plasma returns to stability. During the stable phase, the edge profiles recover until the stability limit is reached again. The cycle can continue as long as plasma core is heated and the edge stays in H-mode. Another class of models, where ELMs are explained as transitions between L- and H-mode [56], is not considered here.

Connor et al. [57] have suggested the following model for the Type I ELM cycle. A sketch of the model is shown in Fig. 3.6. The ELM cycle starts with a low pressure gradient as a result of the previous ELM crash that has removed the edge pedestal. Due to the edge transport barrier, a pedestal with a steep pressure gradient develops at the edge (1). As explained in Sec. 2.2, the first ballooning mode stable region is limited by the pressure gradient. Consequently, the growth of the pedestal stops at the ballooning stability limit (2). Due to the pressure pedestal, the bootstrap current, which is proportional to the density and temperature gradients, builds up on a slower, resistive, time scale. Eventually, the bootstrap current that is parallel to the magnetic field drives the plasma ideal peeling mode unstable (3) causing an ELM crash and the loss of the edge pressure pedestal (4), and the cycle starts from the beginning. The peeling-ballooning ELM model has been experimentally studied in the DIII-D tokamak [58]. In Section 4.1, this model is analysed numerically using experimental plasma profiles for ASDEX Upgrade Type I ELMs.

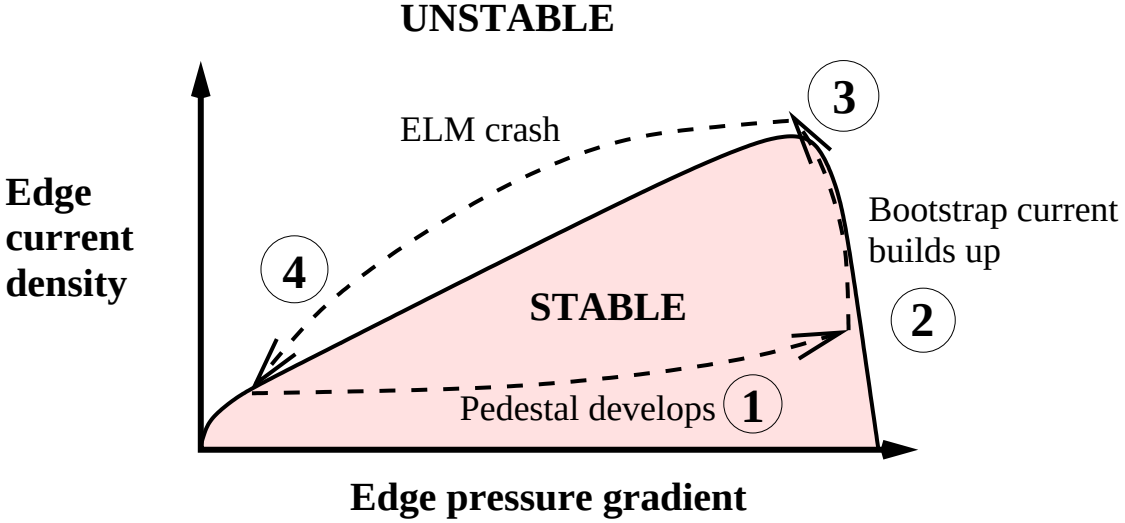

Figure 3.6: *The ELM cycle according to Connor et al.*

The model for the ELM cycle can be tested also for other ELM types. A qualitative model for Type II ELMs has been given by Snyder et al. [59]. In this model, the low-n peeling limit rises due to plasma shaping and increased density. Then, the ELM is triggered by the intermediate-n peeling-ballooning instability that has a narrow mode structure. The changes in the stability for Type II ELMs is analysed in Sec. 4.2.

3.7 ELM control

Controlling the ELM phenomenon is of paramount importance in order to avoid the detrimental effects of ELMs. One way to avoid problems caused by large ELMs is to operate plasma with small ELMs. Another possibility is to choose the operational parameters so that the ELMs are completely avoided. This could mean operating the plasma in, for instance, QHM or EDA-mode. However, these operating regimes are quite limited in their flexibility and performance. For instance, L-mode operation would eliminate the ELMs as well, but the confinement is inferior to H-mode. Therefore, it could be useful to device methods to operate the plasma in ELMy H-mode, but avoid large ELMs by active control. A few methods for active ELM control have been recently successfully tested experimentally. In addition to developing techniques for controlling the ELMs, these methods also allow probing the nature of ELMs.

3.7.1 Edge current modulation

In TCV tokamak, ELMs have been controlled using external coils to modulate the vertical position of the plasma. Shifting the plasma up and down modulates the current flowing at the plasma edge region. The method allows to either delay or precipitate the ELM events [60].

In JET, ramping the total plasma current by changing the inductively driven current has been observed to change the ELM behaviour [61,62]. Increasing the loop voltage and thus ramping up the current in a typical Type I ELMy plasma first increases the ELM amplitude, but after a short time (a few hundred ms), the Type I ELMs change to Type III ELMs. In a current ramp-down, the opposite happens and the Type I ELMs reappear. It is still questionable if this kind of method for ELM control is feasible for ITER because it requires quite substantial variations in the plasma current.

3.7.2 Pellet launching

Another way to externally affect the ELMs has been used in ASDEX Upgrade. Small pellets have been launched from the high field side to trigger ELMs [63]. The intrinsic low-frequency, high-amplitude ELMs are then replaced by high-frequency low-amplitude ELMs that are similar to the intrinsic high-frequency ELMs. A stability analysis of the edge region of the pellet triggered ELMs is given in Sec. 4.4.

3.7.3 Impurity injection

Impurities in the edge plasma and scrape-off layer increase radiation. The increased radiation can be used to mitigate the ELM effects on the divertors [64,65]. The particles that are lost from the plasma during an ELM crash lose their energy through radiation before they reach the divertors. This reduces the divertor heat flux.

Impurity injection can also be used to directly affect the ELM phenomenon itself. In JET and JT-60U, it has been possible to increase the ELM-free phases between Type I ELMs by injecting Argon into an H-mode plasma [66,67]. Unlike in ordinary gas puffing experiments, using impurity seeding it has been possible to lower both the ELM size and the ELM frequency [68].

3.7.4 Edge ergodisation using external coils

Since the ELMs are triggered by an MHD instability that is caused by the steep pressure gradient in the edge transport barrier, it is possible to prevent them by degrading the edge confinement before the ELM crash. In DIII-D [69], this has been successfully demonstrated by ergodising the plasma edge using external coils to produce magnetic perturbations. The problem with this method is that also the confinement is degraded by the loss of the edge barrier. However, the use of external coils for ELM control is still in its infancy. With more experiments, it could be possible to develop this method to avoid large Type I ELMs without significantly degrading the plasma confinement. The feasibility of this method in ITER depends on how large coils are required for the ergodisation and if such coils can be installed.

Chapter 4

ELM stability analysis results

4.1 Stability analysis of Type I ELMs in ASDEX Upgrade

The ELM model described in the previous chapter is tested for experimental plasmas. In publication 1, ASDEX Upgrade (R=1.6 m, a=0.5 m) discharge #11991 at 2.0 s is studied with MHD stability analysis. This shot displays clearly detectable Type I ELMs. Here, the stability analysis methods and the results are shortly described.

4.1.1 Equilibrium reconstruction

The plasma equilibrium is reconstructed using experimental temperature and density profiles and self-consistent bootstrap current as described in Ch. 2.2. Temperature and density profiles are taken just before (≈ 1 ms) an ELM crash. The electron temperature profile is given by Thomson scattering near the edge and by ECE in the core plasma. The ion temperature in the core plasma is obtained from charge exchange diagnostics. However, near the edge it could not be accurately measured, and it is assumed to be equal to the electron temperature. It is possible that this assumption overestimates the steepness of the ion pressure profile near the edge. The reason is that the electron temperature at the separatrix is set by the power balance between the parallel heat conduction to the divertor and the perpendicular heat conduction across the separatrix. The balanced separatrix temperature is found at about 100 eV. However, since the ions are much slower than the electrons, the separatrix ion temperature is not limited by the parallel heat conduction, and the separatrix ion temperature could be higher than the electron temperature. Consequently, the ion pressure profile could also be flatter than that of the electrons. However, the collisional equilibration should keep the electron and ion temperatures similar. In equilibrium calculations, we assume $T_i = T_e$.

The density profile is given by the lithium beam measurements near the edge. The lithium beam measurement is combined with the deconvoluted interferometer data for the full profile. The raw experimental profiles are smoothed for the equilibrium reconstruction. Figure 4.1 shows the experimental and smoothed profiles. Both temperature and density profiles display the typical steep H-mode transport barrier near the plasma edge.

The equilibrium is reconstructed with GRETA code that solves the Grad-Shafranov equation (2.10) for the poloidal flux. Free plasma boundary is assumed, and the plasma

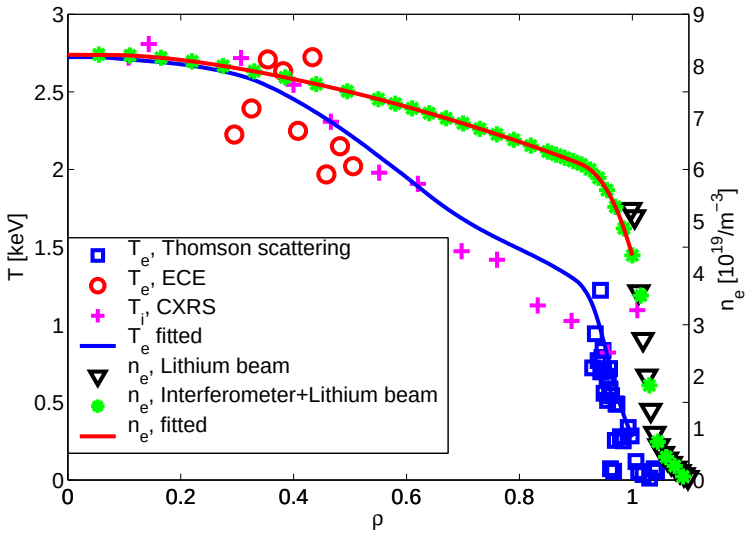

Figure 4.1: *The experimental and smoothed temperature and density profiles used in the equilibrium reconstruction of the shot #11991 at 2.0 s.*

shape is defined using the experimental currents in the poloidal field coils. The bootstrap current is included in the equilibrium reconstruction as described in Sec. 2.2.2. The radial profile of the ohmic current density is assumed parabolic, i.e. $j(x) = (1 - x^a)^b$, where x is the normalised poloidal flux, and a and b are adjustable parameters. In the equilibrium construction, the parameters a and b are adjusted so that q stay slightly above 1 in the plasma centre. This is done because, while the q-profile diagnostics in ASDEX Upgrade are not accurate enough for detailed measurement of the q-profile, but the value in the centre is known to stay above 1 as long as there is no sawtooth activity. Also, q_{95} (q at $\psi_p/\psi_{p,edge} = 0.95$) is roughly known, and it is used in the equilibrium reconstruction. In addition to the inductively driven current profile, the bootstrap current fraction (I_{bs}/I_{tot}) is varied to study how the amount of bootstrap current affects the stability of the plasma. Figure 4.2 shows two flux surface averaged toroidal current density profiles for two values of bootstrap current fraction, 0 % and 13 % that represents case where $C_s = 1$ in Eq. 2.35, i.e. the bootstrap current equals that given by the analytical formula. It is easy to see that a peak is created near the edge as the bootstrap fraction is increased. This current is the source of the peeling mode instabilities.

4.1.2 Stability analysis

Peeling mode stability

The low-n stability of the created self-consistent equilibria is analysed using GATO. An example of a Fourier decomposition of the radial component of the perturbation ($X_m = \xi \cdot \nabla\psi$) is shown in Fig. 4.3. This instability is found for the equilibrium where the bootstrap current fraction is raised to 31 %. It can easily be seen that the mode has a typical peeling-ballooning mode structure: The mode is localised to the edge region.

Figure 4.4 shows the growth rate of n=2, 3 and 4 modes as a function of the bootstrap current fraction (I_{bs}/I_{tot}). The growth rates are normalised to poloidal Alfvén frequency

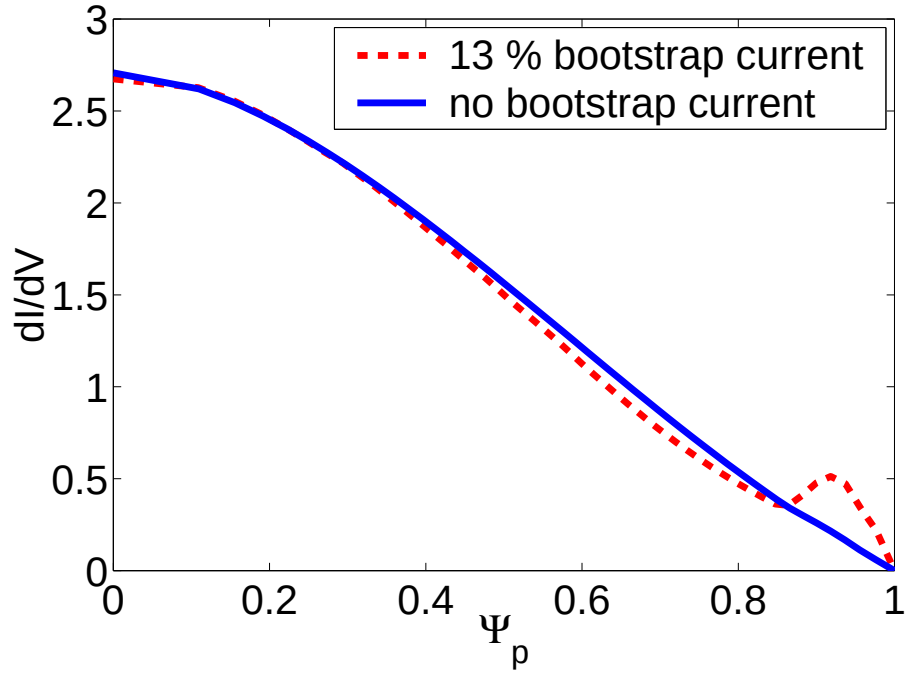

Figure 4.2: *Toroidal current density distribution of an equilibrium with no bootstrap current (solid) and if the bootstrap current amounts to 13 % of the total current (dashed).*

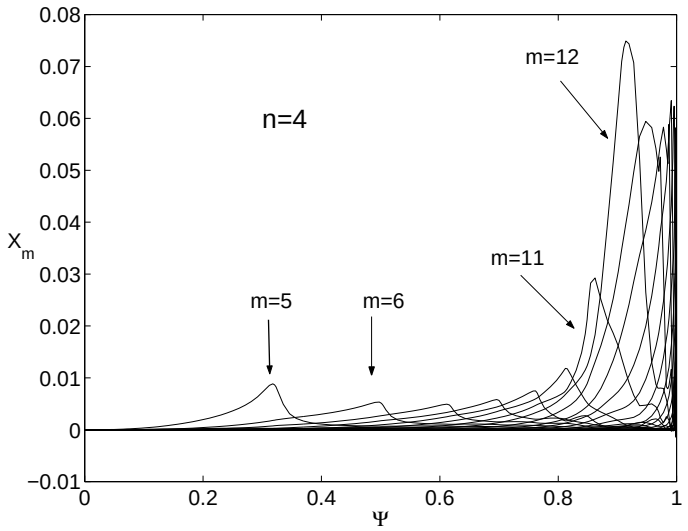

Figure 4.3: *Fourier decomposition of an n=4 peeling mode. Here* $I_{bs}/I_{tot} = 0.31$ *was used.*

($\omega_A^2 = B_0^2/(\rho_0 R^2 \mu_0 q_0^2)$, where B_0 is the magnetic field, ρ_0 is the mass density, R_0 is the major radius and q_0 is the safety factor. All quantities are evaluated at the plasma centre.) The increasing bootstrap current fraction in the equilibrium causes the plasma to become low-n peeling-ballooning mode unstable. The vertical lines in Fig. 4.4 show the bootstrap current fraction that is obtained taking into account 100 % of the neo-classical value (in this case Wilson's model [25], solid line) or ASTRA [74] transport code calculations

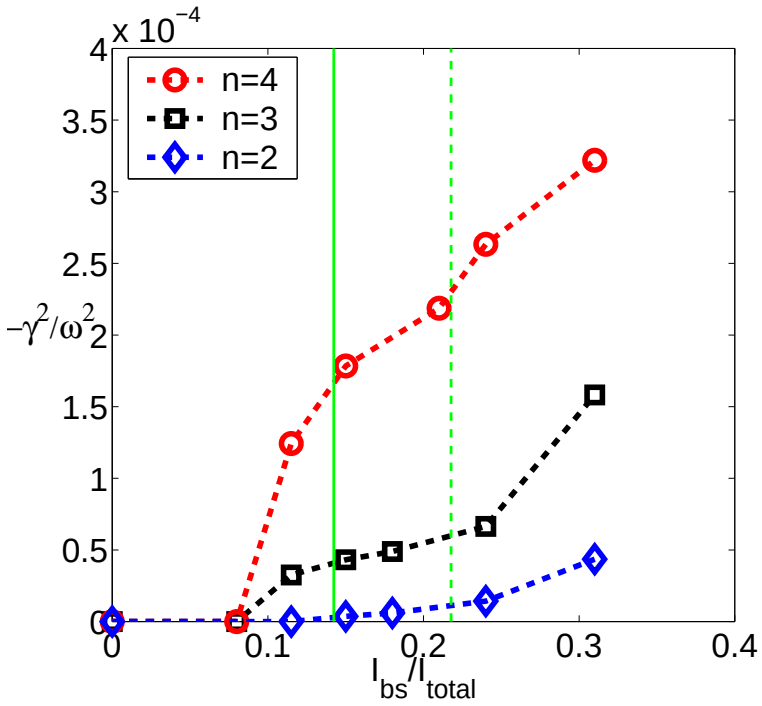

Figure 4.4: *Normalised peeling mode growth rates γ as a function of bootstrap current fraction for three toroidal mode numbers (n=1 is stable over the whole range). The vertical lines represent bootstrap current values calculated by two alternative methods: Wilson model [25] with 100 % of the bootstrap current included in the GRETA equilibrium calculation (solid), and transport calculations with ASTRA code (dashed). ASTRA uses the Hirshman [24] model for the bootstrap current.*

(dashed line). In the range between these two values, toroidal mode numbers ranging from 3 to 6 are found unstable. In the figure, n=2 mode seems marginally unstable, but the small value of the growth rate is at the limit of the numerical accuracy of the GATO code. Only at very high values of the bootstrap current fraction does the n=2 mode become unstable. For the given profiles n=1 mode is stable throughout the investigated range of bootstrap current fractions. The unstable mode numbers agree with the Mirnov coil observations of the Type I ELM precursors [49]. Similar results have been obtained in DIII-D for low-n peeling modes associated with the Type I ELMs [73].

The main result of the linear stability analysis is that the increasing bootstrap current fraction drives the edge plasma unstable. The mode structure of the instability is localised in the edge region suggesting that only the edge confinement is affected when the stability boundary is crossed. In addition, the mode numbers of the found instabilities agree with the experimentally observed mode numbers for the ELM precursors. It must be noted, however, that the linear stability analysis neither gives the time evolution of the plasma after the instability has occurred, nor does it tell how fast the bootstrap current builds up after the steepening of the pedestal pressure gradient. So, from this analysis, it is not possible to know how much of the plasma is lost during each ELM burst or how long the interval between two ELMs is. What can be said, however, is that the stability analysis supports the triggering mechanism of the Connor-Wilson model for ELMs (Ch. 3).

Ballooning mode stability

As explained in Ch. 2, the most unstable ballooning modes generally have high mode numbers. Unfortunately, GATO is restricted to relatively low values of the toroidal mode number and, therefore, another code is used to investigate the high-n ballooning stability. The ballooning stability code GARBO [75] calculates the threshold pressure gradient for the n= ∞ ballooning instability and compares it with the experimental pressure gradient. With GARBO the investigated equilibria are indeed found high-n ballooning unstable if the bootstrap current is low (Fig. 4.5). When the bootstrap current increases, the plasma edge accesses the second stability region for high-n ballooning modes.

Unfortunately, the MHD diagnostics of ASDEX Upgrade are limited to low toroidal mode numbers (n<7). Thus, only instabilities with these mode numbers can be accurately identified experimentally. The high-n modes can not be distinguished in the precursors, and a comparison with the numerical results is difficult.

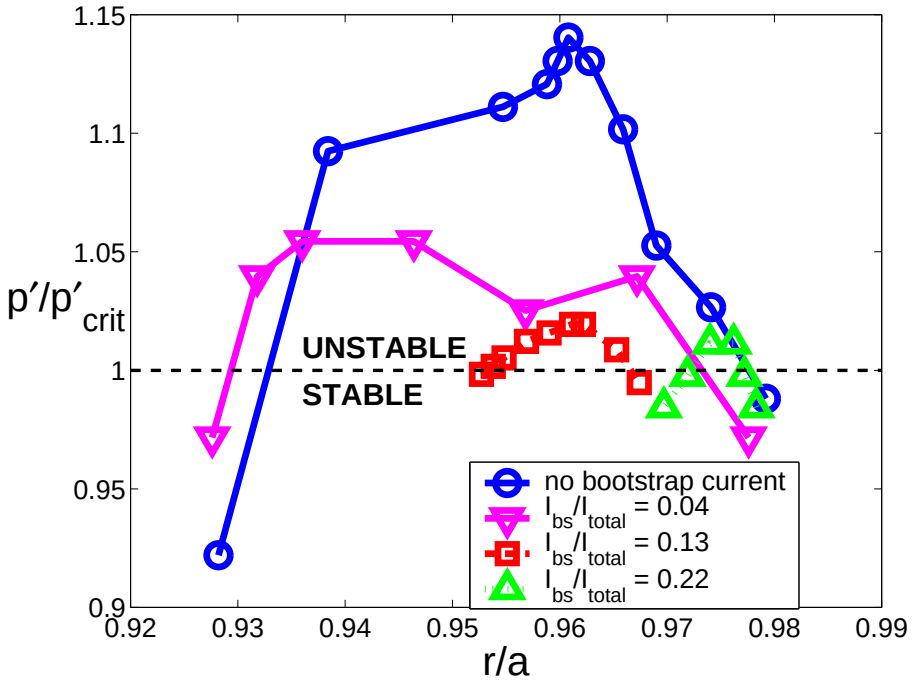

Figure 4.5: *High-n ballooning stability for ASDEX Upgrade shot #11991 at 2.0 s for different bootstrap fractions. Only the most unstable part of the plasma is plotted. The core plasma is stable in all cases. The y-axis is ratio between the experimental pressure gradient and the threshold pressure gradient for ballooning instability given by the GARBO code, i.e. the points with* $p'/p'_{crit} > 1$ *are unstable and those with* $p'/p'_{crit} < 1$ *are stable.*

It is possible that, since the profiles are created with slightly pessimistic assumptions (e.g. the T_i gradient is as steep as the T_e gradient), the ballooning instability is due to an unrealistically steep pressure gradient. The peeling instability, on the other hand, is current driven, and the uncertainty in the pressure profile does not affect it as much. Therefore, even if the bootstrap current is slightly lowered due to the decrease in the pressure and temperature gradients, the results presented in the previous section are still valid. The curves in Fig. 4.4 would be only slightly shifted to the right.

The conclusion that can be drawn from the ballooning mode analysis is that the edge region pressure gradient of a Type I ELMy plasma is close to the ballooning stability limit. Depending on the amount of bootstrap current, it is either slightly below or above the stability boundary. This is in agreement with the theoretical Connor-Wilson model. The ballooning limit of the plasma is considered "soft": Once the plasma pressure gradient reaches the limit, the instability creates turbulence and, thus, increases transport. As the transport increases, the pressure gradient decreases below the stability limit. As the instability disappears, the turbulence decreases again. This feedback mechanism keeps the pressure gradient close to the stability boundary without causing a catastrophic instability.

The ballooning analysis also revealed that, as the bootstrap current fraction is increased, the stability improves. In Fig. 4.5 the stability boundaries of a plasma both without a bootstrap current and with 4 %, 13 % and 22 % bootstrap current fractions are shown. Clearly, while the bootstrap current has a destabilising effect on the peeling modes (Fig. 4.4), it stabilises the ballooning modes. The reason for the stabilising effect is that, since we are investigating the edge of a strongly shaped plasma, the decreasing shear (caused by the bootstrap current) gives plasma access to the second stability region (recall Fig. 2.11).

Stabilising effect of the triangularity

In ASDEX Upgrade, long ELM-free periods have been observed in high triangularity ($\delta = 0.3 - 0.4$) shots, but not with low ($\delta = 0.1 - 0.2$) or medium triangularity ($\delta = 0.2 - 0.3$) [76]. The ELM frequencies were also lower in the high triangularity shots. This apparently stabilising effect of the triangularity is tested for the ELM model. If the model is correct, the stabilising effect of the triangularity should be found also in the numerical studies.

Two ASDEX Upgrade shots (#11991 and #11795) with similar plasma profiles but differing in the plasma shape (Fig. 4.6) are analysed with respect to the peeling modes. In addition to these two experimental shapes, an artificial equilibrium with experimental plasma profiles (T, n), but even higher value of triangularity ($\delta = 0.38$) is analysed. The q-profiles of the two experimental cases are almost identical (q_{95}=3.65 for #11991 and q_{95}=3.85 for #11795). For the very high triangularity case, q_{95} is 4.4. It is found that increasing the plasma triangularity indeed stabilises the plasma (Fig. 4.7). The better stability means that it takes longer to build up the bootstrap current needed to destabilise the peeling mode, or even that the plasma is stable against peeling mode when the bootstrap current has reached its full neo-classical value. This translates to longer periods between ELMs, or even a period with no ELMs at all. The numerical results thus agree qualitatively with the experimental observations.

4.2 Type II ELM stability analysis

Above, the stability analysis results using experimental data from ASDEX Upgrade Type I ELMy plasma was found to agree with the theory-based ELM model. In Publication 2 and 3, the stability analysis is extended to type II ELMs. As explained in Ch. 3, the type II ELMs are smaller than type I ELMs and, thus, are more suitable for a fusion reactor operation. In the stability analysis, the plasma conditions are changed from the typical Type I ELMy plasmas to those required for the operation with Type II ELMs.

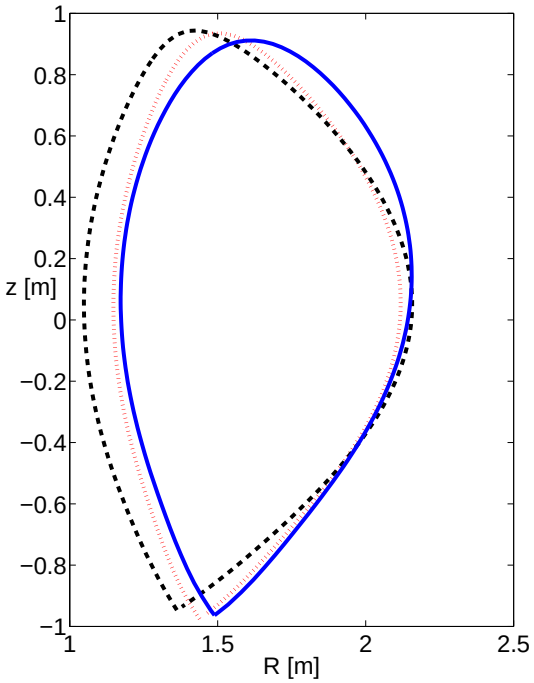

Figure 4.6: *Triangularity variation from $\delta = 0.24$ (#11991, solid line) to $\delta = 0.34$ (#11795, dotted line). The dashed line represents a virtual equilibrium with very high triangularity ($\delta = 0.38$). It is composed from the equilibrium of shot #11991 by artificially increasing its triangularity.*

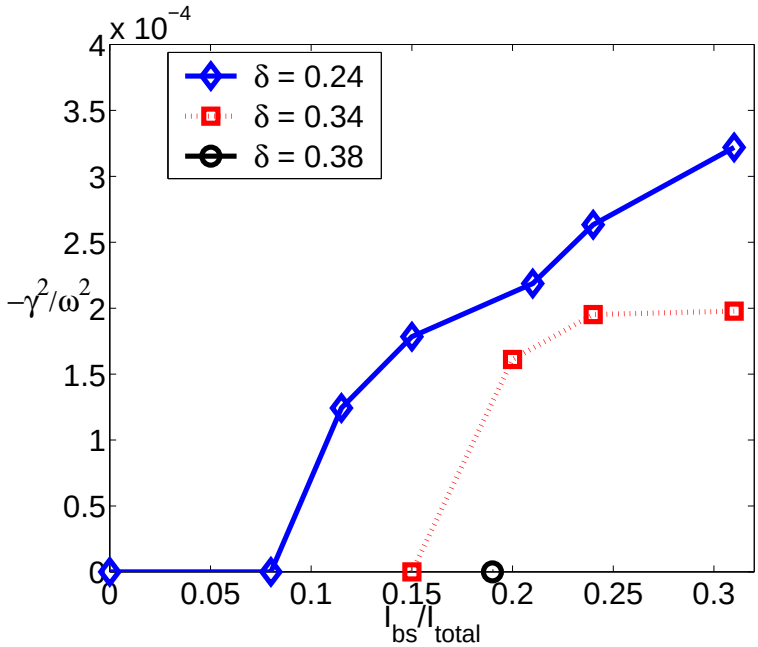

Figure 4.7: *Growth rates of the n=4 peeling mode for medium ($\delta = 0.24$), high ($\delta = 0.34$) and very high triangularity ($\delta = 0.38$).*

The changes in the stability properties can provide an explanation to the changes in the ELM behaviour.

4.2.1 Experimental observations of Type II ELMs

In DIII-D [77], in JT-60U [72, 78] and ASDEX Upgrade [71], it has been possible to replace the large Type I ELMs with smaller Type II ELMs without sacrificing good plasma performance. This is accomplished by using strong plasma shaping and high edge safety factor. However, in JET, the total suppression of the type I ELMs has not been successful. Instead a mixed type I-II operation has been achieved in strongly shaped plasmas with high edge safety factor value [81].

In addition to these general requirements, specifically in ASDEX Upgrade it has been observed that also an almost double-null configuration and sufficiently high density ($\overline{n}_{GW} = 0.85 - 0.95$) are required for the type II ELMs [71]. Decreasing density or moving the second separatrix away from the first one causes a transition back to type I ELMs.

In JT-60U, it has been observed that the requirements of plasma shaping and edge safety factor for the access to small ELMs are less stringent if the global β_p is increased [72, 79]. Also the observed pedestal pressure is higher with increased β_p suggesting that the edge stability is improved against the ELM triggering instabilities.

4.2.2 Edge stability in Type II ELMy plasma

In Sec. 4.1, it was shown that, in ASDEX Upgrade, the type I ELMs are low-n peeling-modes that are destabilised by the bootstrap current. In this chapter, these instabilities are studied in Type II ELMy conditions. The changes in stability properties from those of Type I ELMs can explain the different ELM behaviour.

In publications 2 and 3, the Type II ELMy conditions in ASDEX Upgrade are studied with the same methods as Type I ELMs earlier. As before, the GATO code was used to study low- to intermediate-n stability. High-n ballooning analysis is now done using IDBALL (based on methods in [80]). Both IDBALL and GARBO find the ballooning mode stability boundary using the expansion in powers of 1/n. The main difference is in the easier handling of the results in IDBALL, which is the reason it was used now to replace GARBO. In the stability analysis, the effects of various parameters (high triangularity, high density, almost double null configuration) are analysed independently.

Triangularity and safety factor

The Type I ELM studies in Ch. 4.1 already showed that increasing triangularity improves the edge stability against the low-n modes. If the triangularity is increased from 0.15 to 0.45, the stability of the edge plasma improves so that 30 % more edge current is required to destabilise the low-n peeling-ballooning modes. If the high triangularity is combined with high edge safety factor, also the spatial structure of the instability changes significantly from that of the Type I ELMy plasma. This is illustrated in Fig. 4.8. The eigenfunction of the n=3 instability with $\delta = 0.45$ and q_{95} =5.0 is significantly narrower than with $\delta = 0.15$ and q_{95}=4.3. It should be noted that both increased edge safety factor and high triangularity are required for making the mode very localised at the edge.

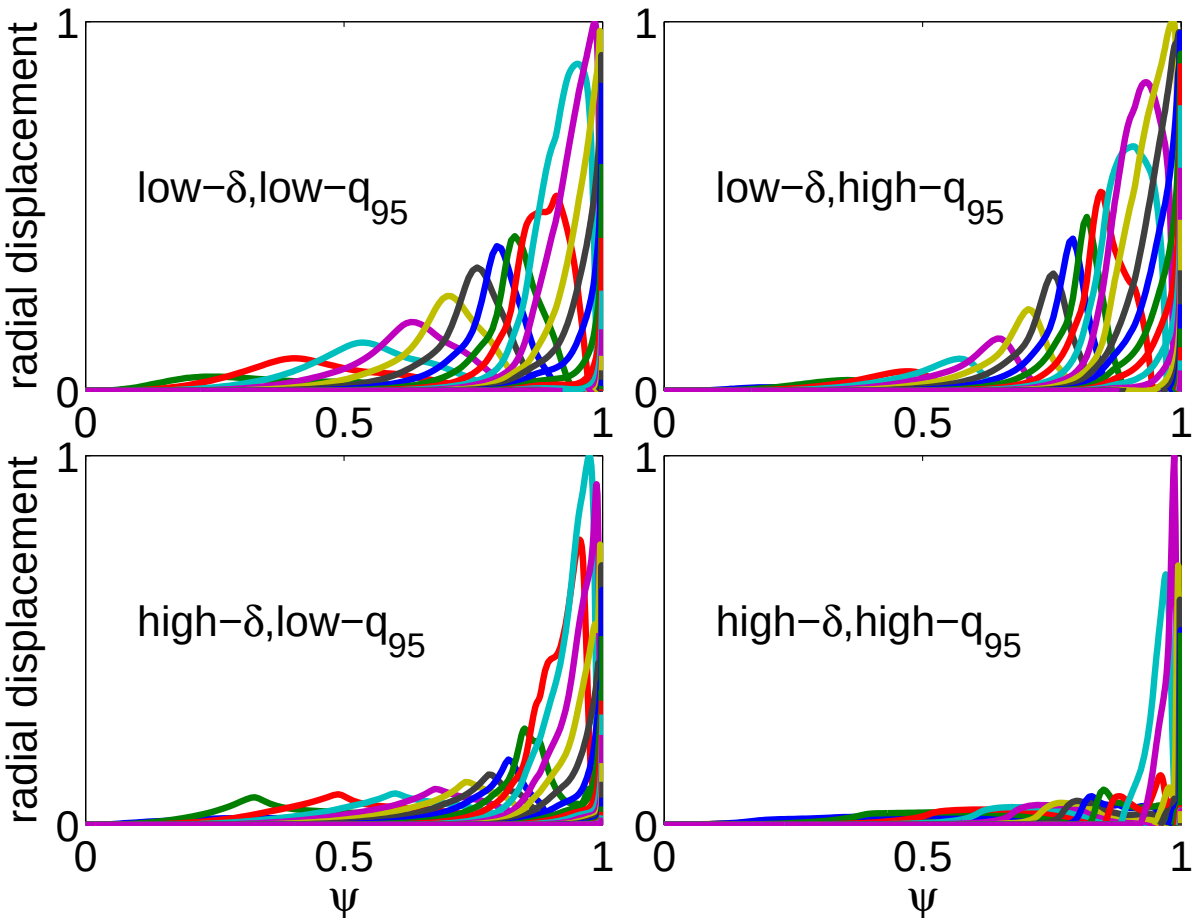

Figure 4.8: *Fourier analysis of the eigenfunctions of the radial displacement for the n=3 peeling-ballooning mode for different q_{95}-δ combinations. Each curve represents the eigenfunction of a single poloidal mode number. Low-q_{95} = 4.3, high-q_{95} = 5.0, low-δ = 0.15, high-δ = 0.45.*

Density

The role of density can be separately examined by keeping the pressure profile fixed, but varying the ratio of density and temperature. When the density increases and temperature decreases, the collisionality increases and the edge bootstrap current decreases. This further stabilises the low-n peeling-ballooning modes. As can be seen in Fig. 4.9, the stabilising effect applies to both single- and double-null plasmas. On the other hand, the second stability access for the high-n ballooning modes becomes narrower in radius and can even be completely closed as the density increases. The narrower or completely closed second stability access can limit the steepening of the pressure gradient thus avoiding the large Type I ELM crashes.

Double-null configuration

The access to Type II ELMs in ASDEX Upgrade, requires an almost double-null configuration. The transition from a pure single x-point configuration to a an almost double null configuration affects the stability of the edge plasma. The x-point has a strong local

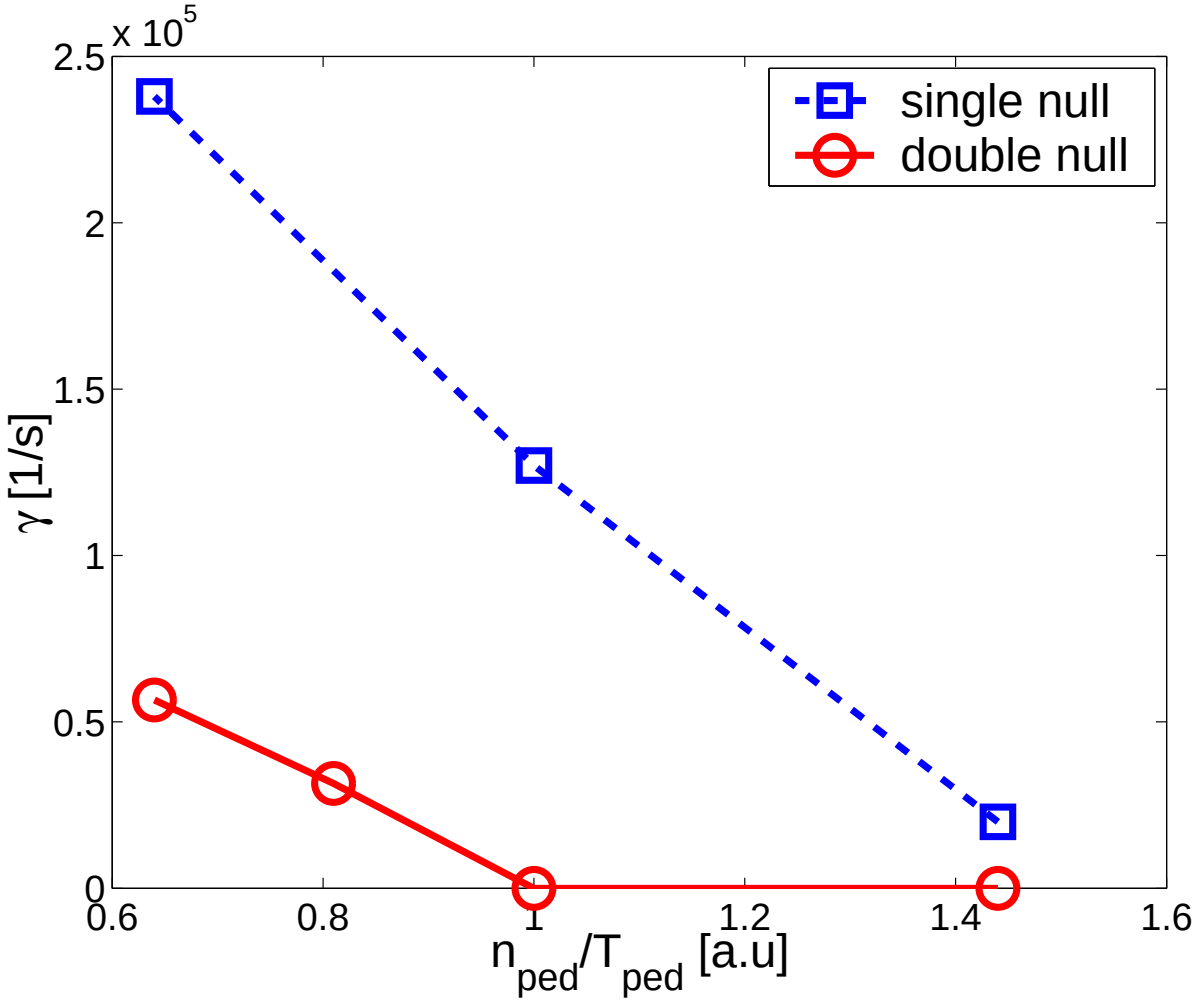

Figure 4.9: *The n=3 peeling-ballooning mode growth rate as a function of the pedestal density-to-temperature ratio. The value 1 is the experimental value.*

stabilising effect on the low- and intermediate-n modes. In the case of two x-points, the stabilisation is naturally even stronger. The stabilising effects of the double null and the increasing edge density are shown in Fig. 4.9. The double-null plasma is more stable than the single-null plasma.

The role of the double null was also studied by comparing two ASDEX Upgrade discharges. One (#15865) is purely single null and displays Type I ELMs. In the other (#15863) the plasma is moved closer to a double null (8 cm at the top of the plasma) and has Type II ELMs. The density and temperature profiles of the shots are very similar. The stability boundaries were found by varying the edge temperature gradients of the two plasmas. In addition to the experimental plasma shapes, a fictitious true double-null plasma was created using the experimental temperature and density profiles, but changing the plasma shape. Figure 4.10 shows the growth rates for the $n = 3$ mode as a function of the maximum pressure gradient in the pedestal region for the different configurations. While both plasmas are stable at the experimental value of the pressure gradient, the stability limit of the Type I ELMy plasma is considerably lower than in both Type II ELMy plasma and the fictitious true double-null plasma.

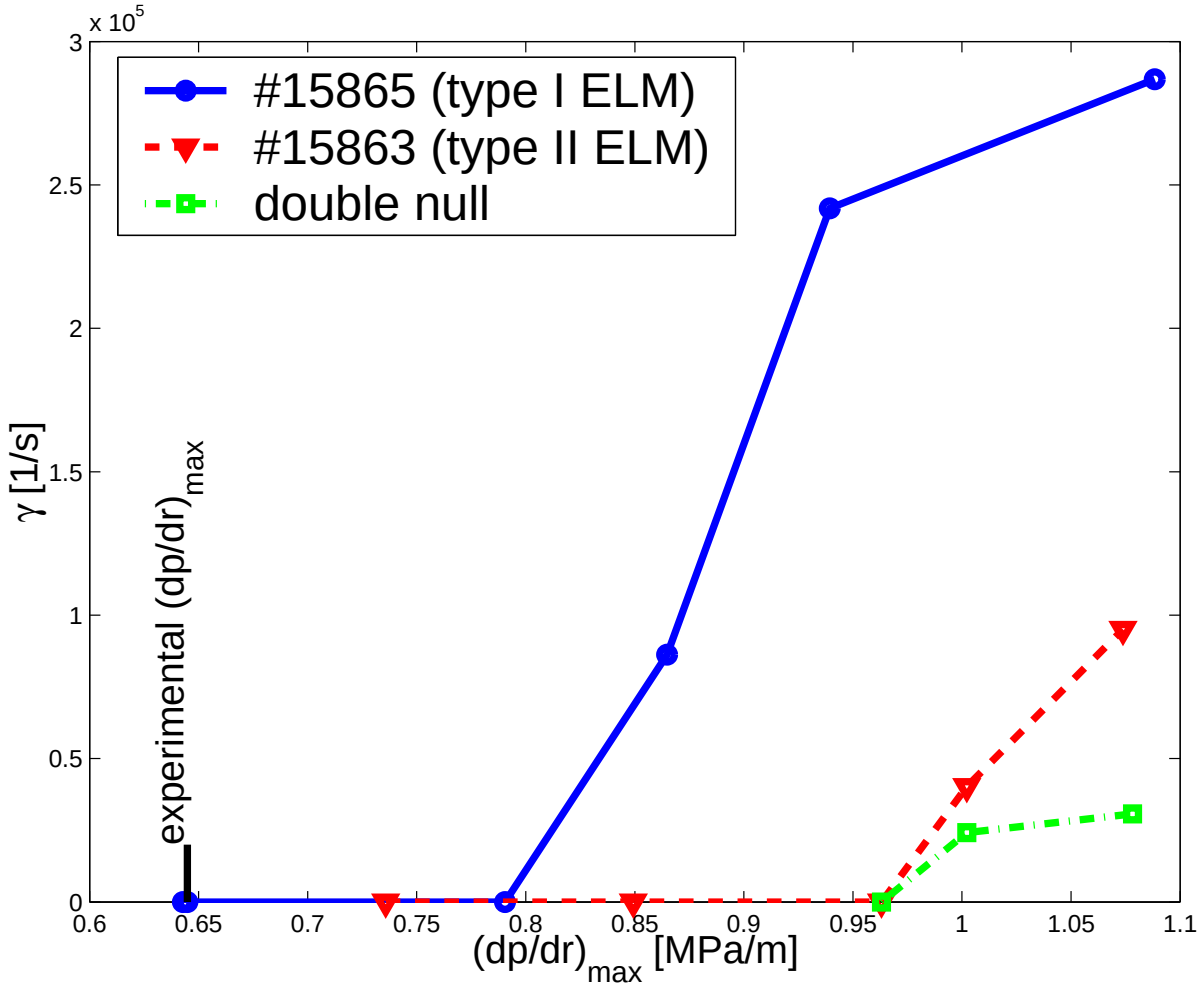

Figure 4.10: *The n=3 peeling-ballooning mode growth rate as a function of the edge pressure gradient for plasmas with Type I (#15865) ELMs, Type II (#15863) ELMs and for an artificial double-null configuration.*

In addition to the stability limit, the double-null configuration affects also the radial structure of the instability. The effect of the x-points on the 2-dimensional mode structure is shown in Fig. 4.11, where the plasma displacement ξ is plotted in the poloidal plane. It is easy to see that in both cases the mode disappears completely near the lower x-point and, in the case of the double-null plasma, also near the upper x-point.

It is interesting to note that the almost double-null configuration has similar effect on the radial structure of the low-n instability as the combination high triangularity and high safety factor, i.e., the eigenfunction becomes more localised on the edge. This can be seen in Fig. 4.12, where the envelopes of the n=8 eigenfunctions for the two above-mentioned ASDEX Upgrade discharges are compared. The eigenfunction for the equilibrium of #15863 is significantly narrower than that of #15865.

Global poloidal β-value

In publication 4, the effect of increased global β_p is investigated by varying the core pressure and analysing its effect on the edge stability. The edge profiles are taken from

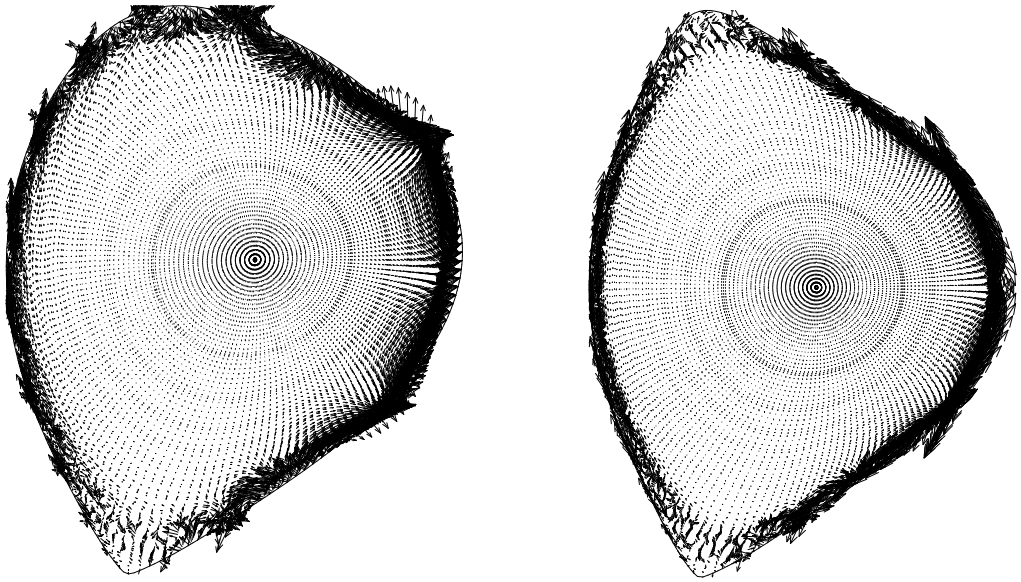

Figure 4.11: *The n=3 peeling-ballooning mode structure for single- (left) and double- (right) null plasmas. Both upper and lower x-point eliminate the mode from their vicinity.*

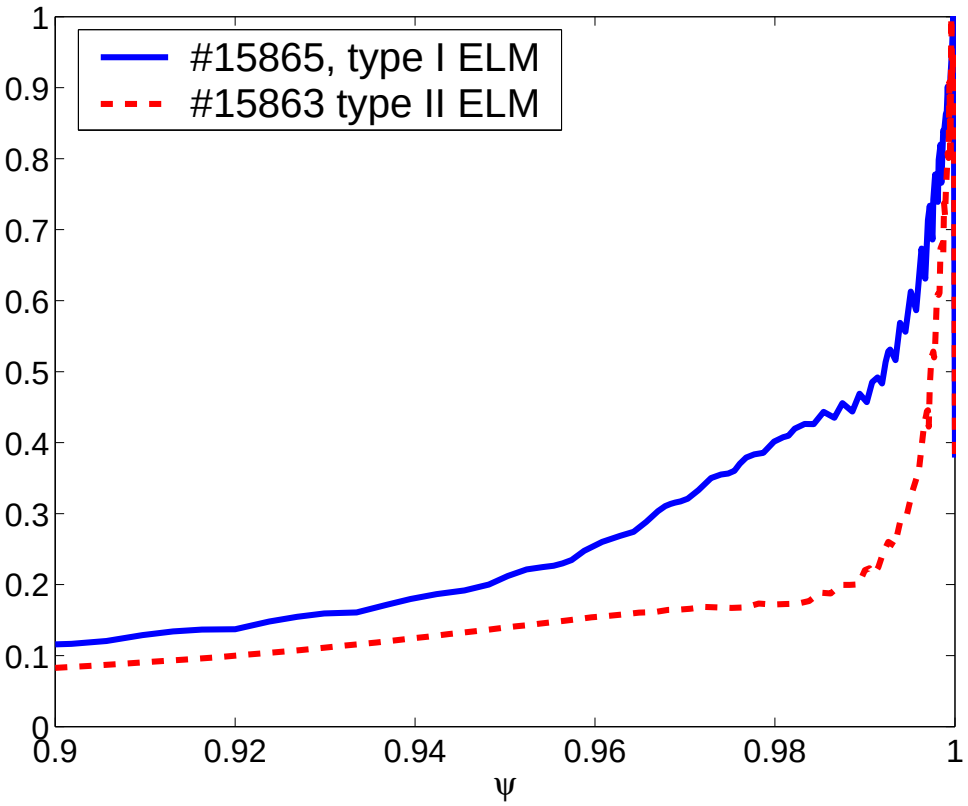

Figure 4.12: The n=8 peeling-ballooning mode radial envelope (the normalised sum of Fourier components of the $\xi \cdot \nabla\psi/|\nabla\psi|$) for type I (#15865) and type II (#15863) ELMy plasmas. The pedestal top is at $\psi = 0.94$. Note that both modes are narrower than the pedestal.

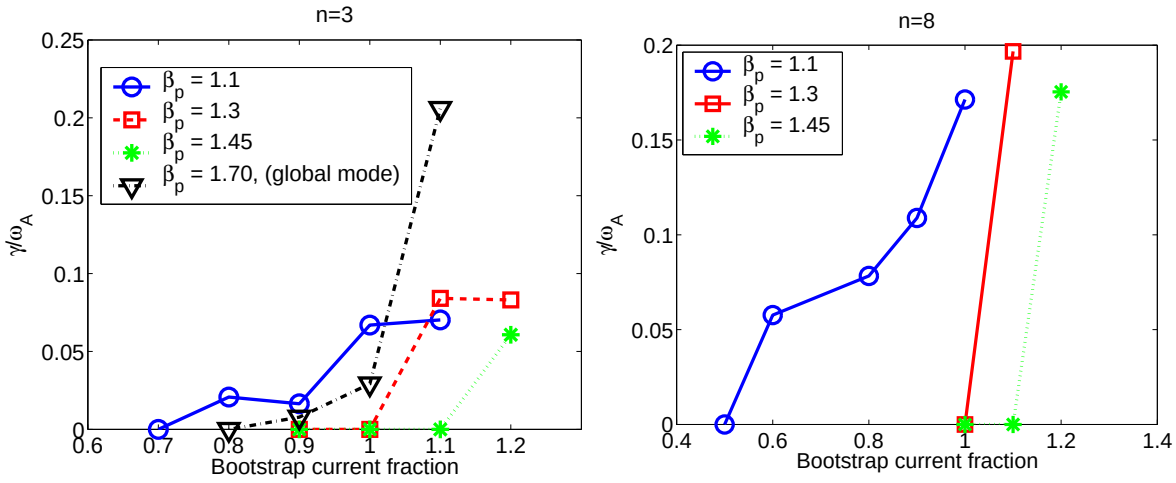

Figure 4.13: *Growth rate for the n=3 and n=8 peeling-ballooning modes for the high triangularity ($\delta = 0.42$) plasma as a function of the bootstrap current fraction for various values of β_p.*

the Type I ELM case of the previous study (ASDEX Upgrade discharge #15865). The core density is increased and the effect of the increasing β_p on the edge stability is studied. For each value of β_p the amount of bootstrap current that is included in the equilibrium reconstruction is varied to find the stability boundary.

The increased core pressure changes directly the equilibrium in the core region, but as long as no global mode is destabilised, this change does not influence the edge stability. The effect of increasing $\beta_p$on the equilibrium in the edge region is quite complicated. When the poloidal β is increased, it lowers the current in the edge. The reason for this is that in the high β_p plasma, the Shafranov shift squeezes the flux surfaces on the low field side and makes them further apart on the high field side. Thus, the distance between two flux surfaces increases on the high field side and decreases on the low field side. Since the toroidal current density is higher on the low field side, the flux surface averaged toroidal current density in the edge region decreases with increasing β_p. In addition to the current modification, the shift of the flux surfaces also increases the average "favourability" of the curvature ($\langle \kappa \cdot \nabla p \rangle$).

The stability analysis results of the β_p variation can be seen in Fig. 4.13, where the growth rates of n=3 and n=8 modes are plotted as a function of the fraction of the bootstrap current given by Sauter's formula [26] included in the equilibrium reconstruction. As can be seen, the increasing β_p has a stabilising effect on both modes, i.e. higher bootststrap current fraction is required for the destabilisation. The reason for the better stability with high β_p is the combined effect of lower current and more favourable average curvature.

The increasing β_p affects the high-n ballooning mode stability by moving the plasma closer to the stability limit. The reason is the lower edge current which increases the shear and thus limits the access to the second stability region.

4.2.3 The edge stability effects on the ELM triggering

Above, all the conditions required for Type II ELMs were investigated with a stability analysis. Now, the results can be combined and it is possible to predict, what the effects the required plasma conditions have on the ELM phenomenon. Of course a linear MHD analysis is not able to simulate the non-linear phase of the ELM crash, but with some simple assumptions the qualitative changes in the ELMs can be predicted.

The main result of the stability analysis was that the eigenfunctions of the ELM-triggering low- to intermediate-n peeling-ballooning modes are narrower in Type II than in Type I ELM conditions. In addition, the plasma becomes more stable against low-n modes, while the stability against modes with higher mode numbers is not improved. Since the intermediate-n modes were found to have narrower mode width than the low-n modes, the shift to higher mode numbers causes further localisation of the eigenfunction of the ELM triggering instability.

In DIII-D, the relative temperature drop during an ELM crash has been shown to match with the envelope of the most unstable mode corresponding to the equilibrium created for the plasma just before the ELM crash [59]. Therefore, we can assume that the width of the eigenfunction at least qualitatively affects both the ELM penetration depth and the amplitude of the ELM. Using this assumption the stability analysis results predict that the ELM-affected area and the ELM amplitude should be smaller for Type II ELMs than for Type I ELMs. This is indeed what has been observed in the experiments.

4.3 Quiescent H-mode

The ELMs cause problems in a tokamak operating in H-mode because the energy and particles that are lost from the plasma arrive to the plates in short bursts instead of a continuous flow. However, it is possible to find an operating mode where the ELMs are suppressed while keeping the good confinement and avoiding density accumulation. The so-called quiescent H-mode (QHM) was first observed in DIII-D [45] and, more recently, also in ASDEX Upgrade [44] [90]. The QHM is obtained by counter-injecting neutral beams, keeping high clearance between the plasma and the surrounding solid surfaces, and employing good cryopumping on the divertors by having the strike point at the pumping position. From the fusion reactor operation point of view, the drawback of the quiescent H-mode is that the effective charge (Z_{eff}) increases due to the accumulation of impurities in the core plasma [43]. While the good performance of the quiescent H-mode is experimentally proven, the reason for the ELM suppression is still lacking. The question of how the pedestal pressure similar to ELMy H-mode can be attained in QHM without destabilising the edge and causing an ELM crash is still to be answered.

4.3.1 Quiescent H-Mode in ASDEX Upgrade

Several features that distinguish QHM from standard ELMy H-mode have been observed in ASDEX Upgrade discharges. The quiescent H-mode is characterised by good energy confinement and suppression of ELMs. Compared to similar Type I ELMy plasmas, in QHM the pedestal pressure is about 10 % higher [44]. Additionally, the rotation of the core plasma is significantly increased. The effects of the core rotation on the plasma performance are still unknown.

While the ELMs are suppressed during the quiescent phase, special type of magnetic activity is observed. Fishbones and edge harmonic oscillations are observed at the frequency range of 7-30 kHz. Additionally, high frequency oscillations at the frequency of 350 and 490 kHz occur in QHM. While potentially important to the particle and energy exhaust, the MHD events do not seem to limit the pedestal pressure to a lower value in QHM than in ELMy H-mode. Therefore, it is unlikely that they alone could explain the disappearance of the ELMs.

The QHM plasma profiles are characterised by high ion temperature, low density and high Z_{eff} (≈ 5, while values 1-3 are typical for ELMy H-mode). However, recent experiments have been successful with Z_{eff} at the same level as in ELMy H-modes [90]. The electron temperature is slightly higher in QHM than in ELMy H-mode.

All the quiescent H-mode plasmas first enter an ELMy phase, followed by the quiescent phase, where the ELMs disappear, and eventually the ELMs reappear again. There can be more than one quiescent phase, but it is notable that no completely ELM-free discharge has been obtained. This behaviour has also been observed in D-IIID [45]. This indicates that there has to be a change in the plasma conditions that trigger the suppression of ELMs. The external conditions (high pumping, counter-injected neutral beams, high clearance) can not directly stabilise the edge plasma and prevent the instability that is responsible for the ELMs. This is further supported by the fact that ELMy H-modes have been observed with counter-injected discharges with sufficient clearance. Therefore, it seems that the ELM suppression is due both the configuration required for QHM and the change in plasma profiles during the discharge.

4.3.2 Edge plasma stability analysis for QHM

In the earlier sections, the edge MHD stability was analysed before an ELM crash in different plasmas. The stability analysis confirmed the model where at least the Type I and Type II ELMs are triggered by low- to intermediate-n peeling-ballooning modes. If the model is correct, these instabilities should be stable in QHM.

Stability limit for the pressure gradient

The stability of two counter-injected ASDEX Upgrade shots (#16104 and #16112) with identical shapes, one with ELMs and the other in QHM is analysed. The global parameters for both shots are: geometric major radius $R = 1.62$ m, minor radius $a = 0.49$ m, plasma current I_p =1 MA, toroidal magnetic field $B_T = 2$ T at $R = 1.65$ m, elongation $\kappa = 1.7$, upper triangularity $\delta_u = 0.0$ and lower triangularity δ_l=0.4. The D_α-signals of these shots are plotted in Fig. 4.14. The signal from the QHM-discharge shows long intervals when the ELM activity is completely suppressed, while the reference discharge has ELMs throughout the H-mode period.

Since both of the analysed shots have counter-injected beams, the plasma shapes are identical, and even the QHM-shot have an ELMy phase, neither the beam direction nor the clearance can be the reason why one of these shots is quiescent and why the other has ELMs. Both the direction of the beams and the wall clearance can still have some effect on the stability boundaries, though.

As before, the equilibria for both discharges were created taking into account the bootstrap current self-consistently. The smoothed electron density, electron temperature

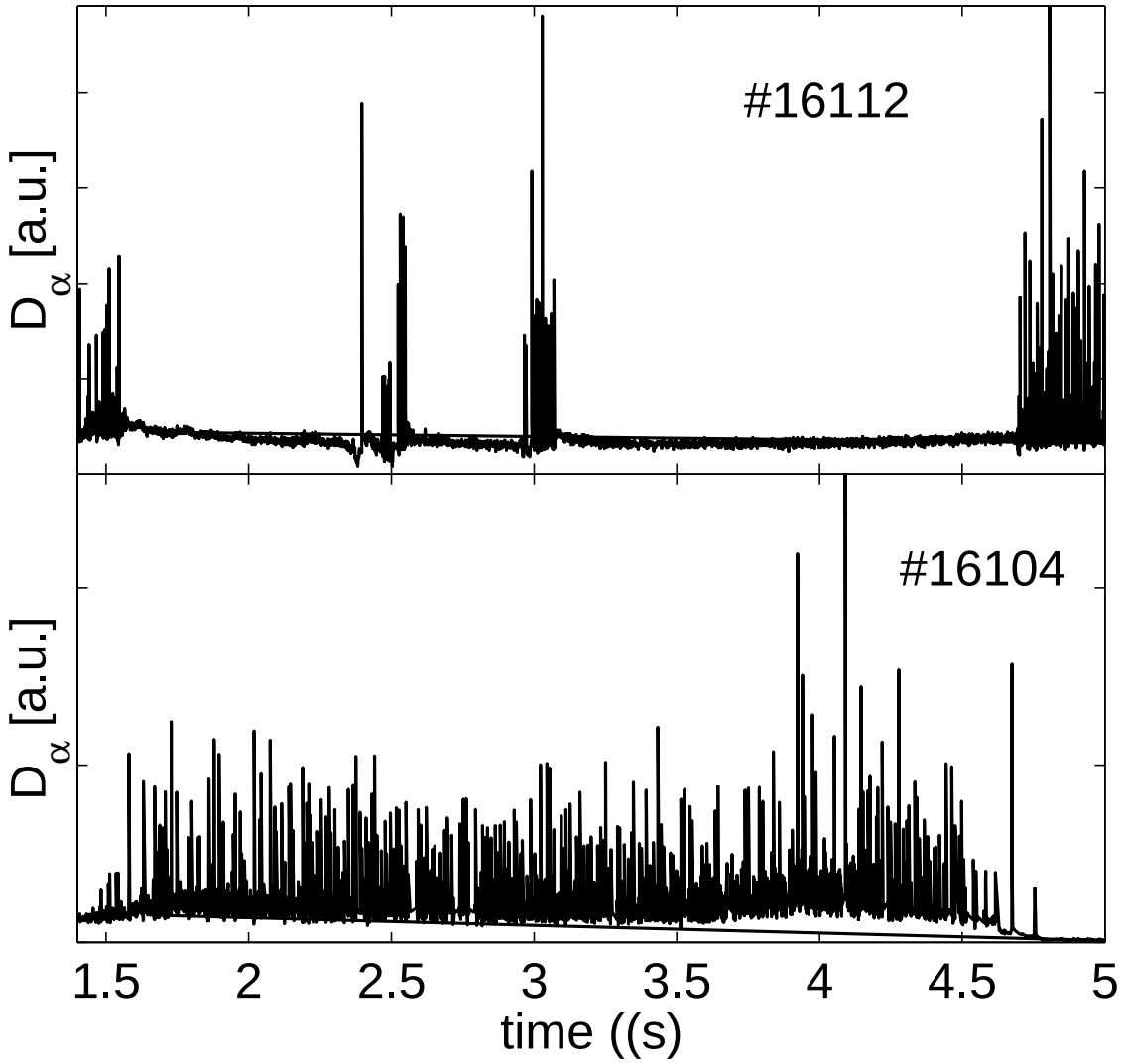

Figure 4.14: *D_α-signal of a QHM-discharge (#16112) and an ELMy H-mode discharge (#16104) in ASDEX Upgrade. In #16112, The ELMs are completely suppressed three times, the longest period lasting about 1.5 s.*

and ion temperature profiles used in the equilibrium reconstruction are shown in Fig. 4.15. Due to the high clearance no edge Thomson scattering is available for these shots. The values from the core Thomson scattering and CXRS are used to set the pedestal top values. The steepness of the edge profiles is adjusted so that the pressure gradient is similar to a well-diagnosed H-mode plasma edge and equal in both plasmas. The Z_{eff} profile is taken flat at values of 5 and 2.5 for QHM and ELMy H-mode, respectively. The inductively driven current profile is determined by the conductivity profile. The pressure gradients and the corresponding bootstrap currents for both plasmas are shown in Fig. 4.16. Note that with almost identical pressure gradients the bootstrap current profiles in the steep gradient region differ significantly. This is because, in this parameter range, the density gradient is more effective a driver of the bootstrap current than the temperature gradient, and also because the ion temperature gradient, which is especially

high in QHM, drives less bootstrap current than similar electron temperature gradient. The largest effect, however, is that the higher Z_{eff} of the QHM reduces the bootstrap current. It accounts for roughly half of the difference between the current profiles. The effect of Z_{eff} on the stability will be analysed in more detail later.

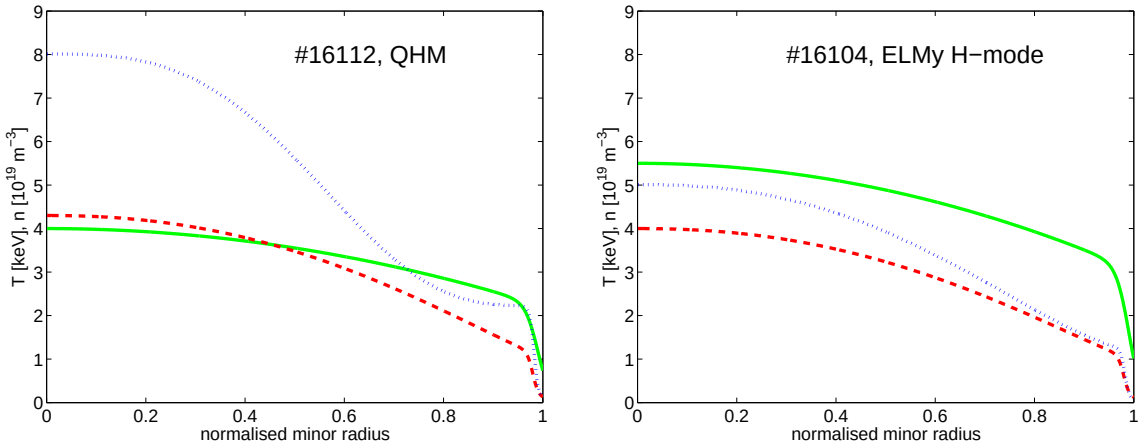

Figure 4.15: *The smoothed electron density* $[10^{19}m^{-3}]$ *(solid line), electron temperature* [keV] *(dashed line) and ion temperature* [keV] *(dotted line) profiles for QHM and ELMy H-mode plasmas.*

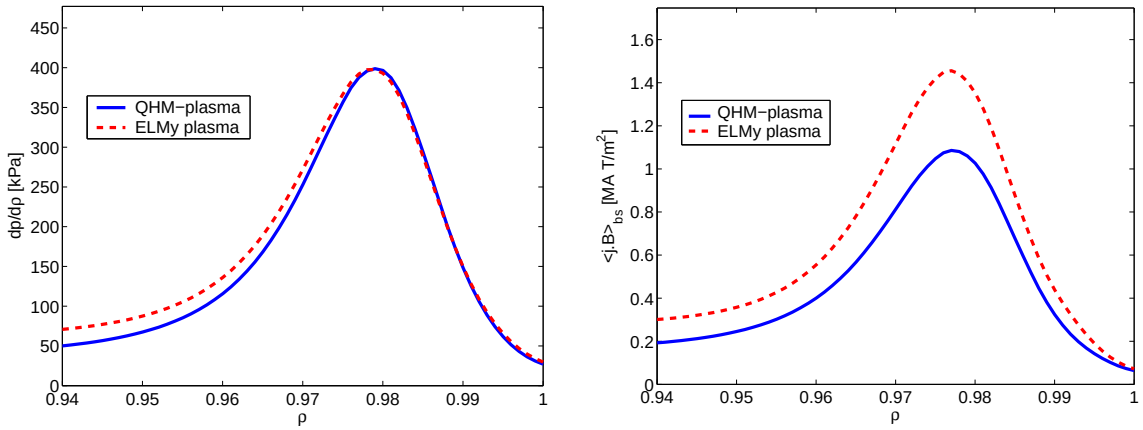

Figure 4.16: *The pressure gradient and the corresponding flux-surface averaged bootstrap current density as a function of the normalised radius for QHM (solid line) and ELMy H-mode (dashed line) plasmas.*

The stability properties of the QHM and ELMy plasmas are compared by varying the edge pressure gradient and analysing the stability. For the edge pressure gradient variation, the temperature profiles are scaled. They are multiplied by a scalar, new equilibria are solved, and the stability analysis is repeated. The result of the pressure gradient scan is shown in Fig. 4.17, where the growth rate of the n=3 mode is plotted as a function of the normalised pressure gradient α $(= -2\mu_0 Rq^2(dp/dr)/B^2)$ for both ELMy and QHM plasmas. The edge bootstrap gradient is the destabilising force for the low-n peeling-ballooning modes. As was shown above, with equal pressure gradients the bootstrap current is lower in the QHM than in ELMy H-mode. This is the reason why

in QHM-conditions the pressure gradient can be increased significantly higher than in ELMy-conditions before plasma becomes unstable.

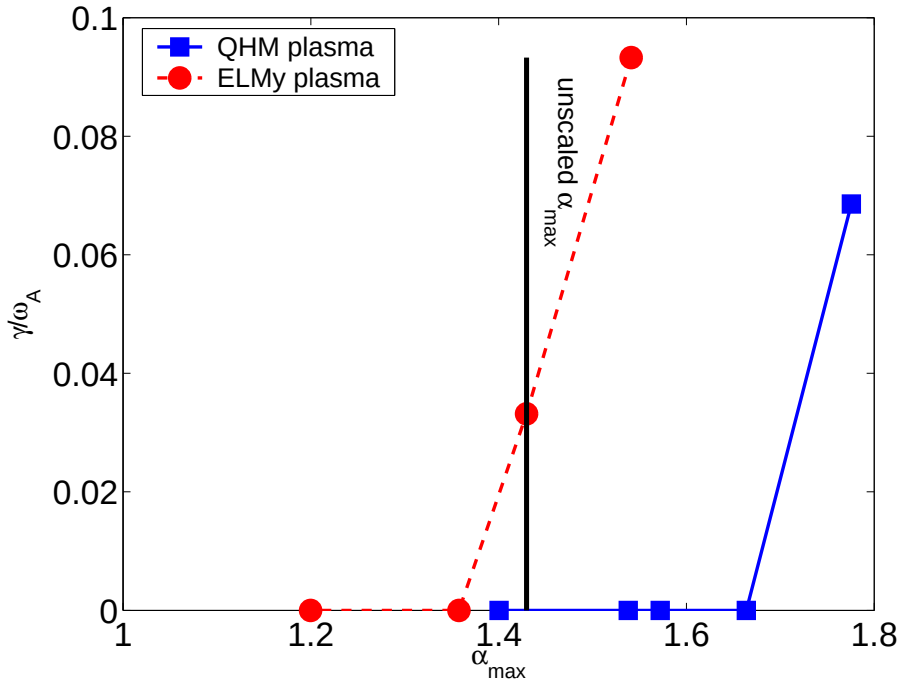

Figure 4.17: *Plasma edge stability against n=3 peeling-ballooning mode as a function of the maximum normalised pressure gradient α in the edge region. The vertical line shows the value of α_{max} for profiles in Fig. 4.15. One should note that the unscaled α_{max} is same for both plasmas.*

The toroidal mode number (n=3) used in the above stability analysis was selected on the basis of experimental observations on ELM precursors. The observed mode numbers for Type I ELMs in ASDEX Upgrade vary in the range of n=3-6 [49]. Similar mode numbers are detected also for Type II ELMy precursors [71]. However, it is possible that the edge stability is actually determined by intermediate mode numbers in the range of n=5-31 [59]. Therefore, the stability at a higher mode number, in this case n=8, is also analysed to see whether the mode number makes a difference in the stability behaviour. While the growth rates for the unstable n=8 modes are higher, the threshold (in α_{max}) where n=8 is destabilised, is found to be the same as for n=3. Therefore, it seems that at least in the intermediate range, the mode number has little effect on the stability limits. The stability analysis for even higher mode numbers becomes computationally prohibitive.

As before also the n=∞ ballooning mode stability properties are compared. Figure 4.18 shows the n=∞ ballooning stability diagrams on two flux surfaces, at the location of the steepest pressure gradient ($\rho = 0.982$) and between the steepest pressure gradient and the plasma edge ($\rho = 0.99$). Both the QHM and Type I ELMy H-mode have access to the second stability in the steepest gradient region. For the same value of α, QHM is slightly closer to the stability limit than the ELMy H-mode. At the very edge ($\rho > 0.99$), QHM becomes limited by the ballooning stability boundary while ELMy H-mode is still in the second stability region. However, there α is already only half of the maximum

value. Therefore, it can be said that the n=∞ ballooning stability does not limit the pressure gradient in the steepest gradient region for either QHM or ELMy plasmas.

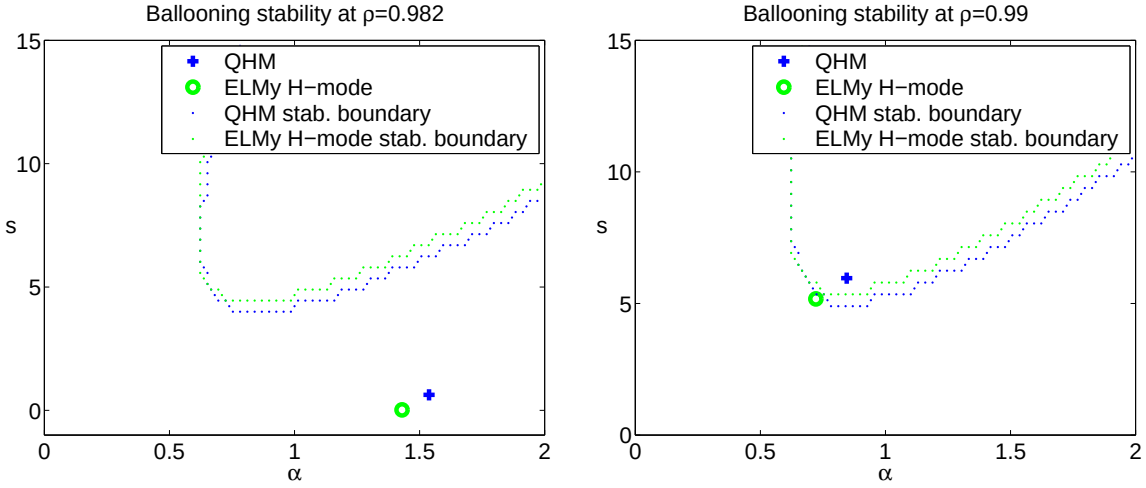

Figure 4.18: *The n=∞ ballooning mode stability diagram in s-α space at two different radial locations for QHM (cross) and ELMy H-mode (circle). The dotted lines show the stability boundary and the symbol shows the operational point, i.e., the equilibrium value for shear and α at that location.*

Stabilising effect of Z_{eff}

In QHM the effective ion charge Z_{eff} is significantly higher than in ELMy H-mode. In addition to the aforementioned value of $Z_{eff} = 5$ in ASDEX Upgrade QHM, in DIII-D $Z_{eff} = 6.5$ has been observed in quiescent double barrier mode that is similar to the "ordinary" QHM [43].

The direct effect of Z_{eff} on the equilibrium is to lower the bootstrap current. This leads to improved stability against the low-n peeling-ballooning modes. This is illustrated in Fig. 4.19, where the growth rate is plotted as a function of Z_{eff}. In this scan, temperature and density profiles are kept fixed. The plot shows that lowering the impurity content from the value typical to QHM (Z_{eff}=5) to the range of ELMy H-mode ($Z_{eff} = 2$) corresponds to a similar increase in the instability growth rate as caused by a 10 % increase in the pressure gradient.

Here it should be noted that while the increasing Z_{eff} has a stabilising effect on the low-n peeling-ballooning modes through the reduced bootstrap current, it does not necessarily mean that it is increased Z_{eff} that reduces the bootstrap current in the experiment. As explained above, also the high ion temperature and low density in QHM drives less bootstrap current for the same pressure gradient than low ion temperature and low density in the ELMy H-mode.

Plasma size and position

In ASDEX Upgrade, QHM has required a high clearance from the walls. The consequence of the large clearance is that the plasma size is smaller than in typical ELMy H-modes. The minor axis is 0.50 m instead of the conventional ELMy H-mode value of 0.53 m. The effect of the plasma size to the edge stability is investigated by analysing the stability

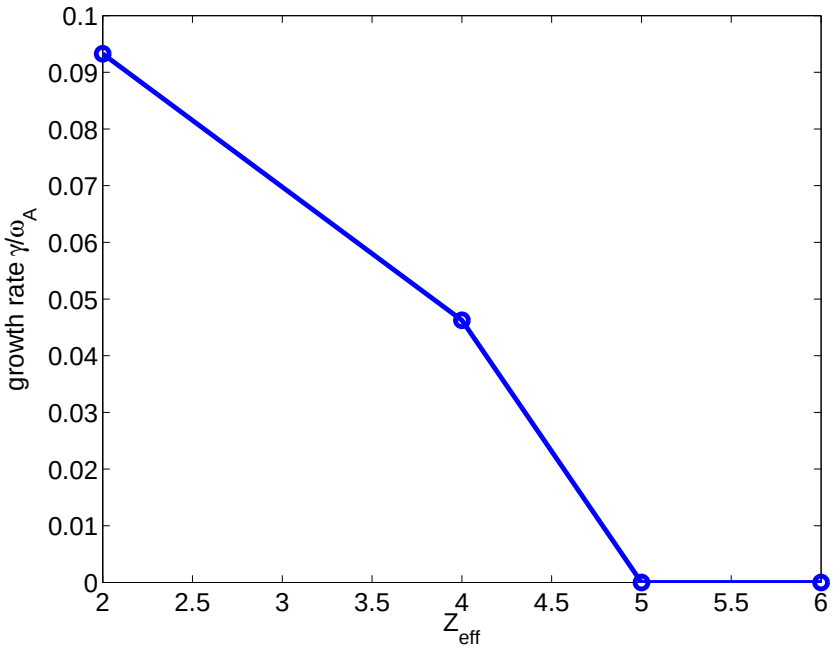

Figure 4.19: *Plasma edge stability against the n=3 peeling ballooning mode as a function of effective ion charge Z_{eff}. The pressure profile used in the scan corresponds to the second highest α for the QHM-plasma in Fig. 4.17*

of two equilibria with the same shape, but slightly different minor radius. Total plasma current and toroidal magnetic field are held fixed. As can be seen in Fig. 4.20, the edge pressure gradient $dp/d\psi_N$ can be increased more with the smaller plasma than with the larger one before it is driven n=3 unstable. Naturally, the difference in stability limits is even higher if, instead of using the pressure gradient with respect to the normalised flux surface on the x-axis, the actual spatial pressure gradient dp/dr were used. This is because with smaller plasma size $d\psi_N/dr$ increases.

Alternatively to reducing the plasma size, sufficient clearance from the outboard wall (as required by QHM) can also be achieved by moving the entire plasma inwards. The clearance on the low field side affects the plasma conditions indirectly by changing the fast particle population as well as recycling from the main chamber walls. These effects can modify the plasma profiles and the impurity content. Additionally, outward radial shift of the plasma directly changes the edge stability. If the plasma is shifted inwards with fixed vacuum toroidal magnetic field and plasma current, the toroidal magnetic field inside the plasma increases. This naturally lowers β and increases q, and tends to stabilise the edge peeling-ballooning modes. The change in the growth rate for the n=3 mode as a function of the radial position of the magnetic axis is shown in Fig. 4.21. With a radial shift of 10 cm, the unstable mode is completely stabilised.

As shown above, small size and inward positioning of the plasma increase stability of the edge against the low-n peeling-ballooning modes. However, these stabilising effects are relatively small, and can not alone explain the ELM suppression. Other effects from large clearance such as reduced ion orbit losses from ill-confined beam ions can have larger effects on the edge stability, but without detailed kinetic simulations these effects are difficult to quantify. The above stability analysis results on the plasma size and position

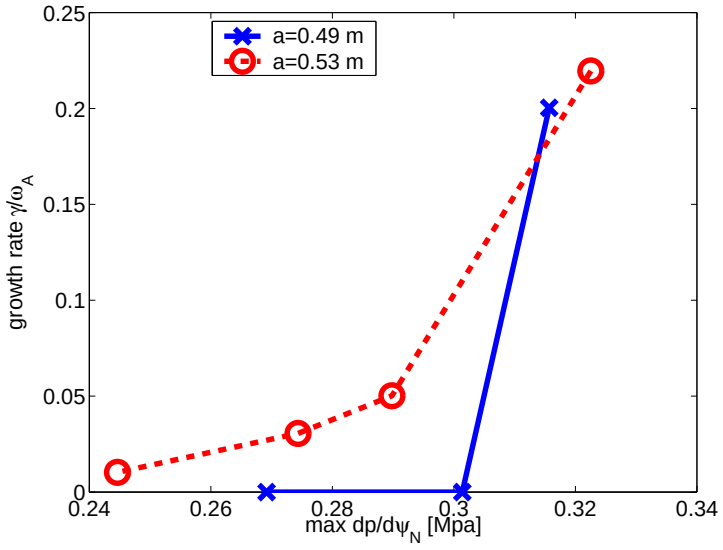

Figure 4.20: *The growth rate of the n=3 peeling-ballooning mode as a function of maximum value of $dp/d\psi_N$ in the pedestal for a=0.49 m and a=0.53 m.*

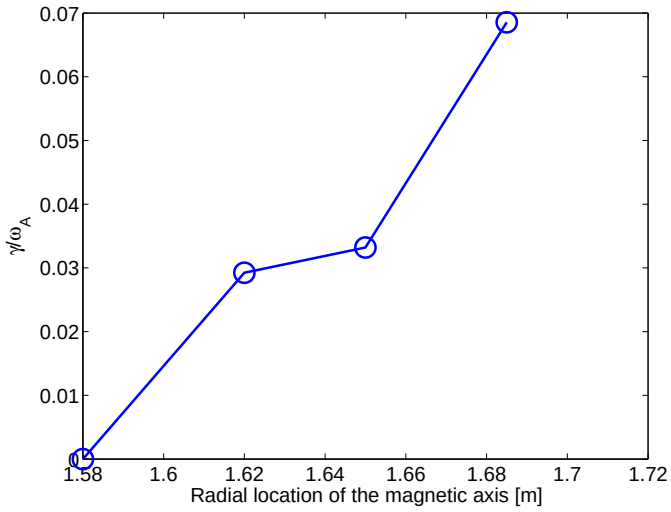

Figure 4.21: *The growth rate of the n=3 peeling-ballooning mode as a function of the radial position of the magnetic axis. Here, R_0 =1.685 corresponds to the most unstable point for QHM-type plasma in Fig. 4.17.*

have effect only in marginal cases, i.e. when the plasma is just at the border between the ELMy H-mode and QHM, a change in the size or position could trigger the transition.

4.4 Pellet Triggered ELMs in ASDEX Upgrade

ASDEX Upgrade has been successful in triggering ELMs using pellet injection from the high field side [63]. Small (6×10^{19} D-atoms) pellets were launched at the velocity of 560 m/s with repetition frequency of 19 Hz. During the 4 s when pellets were launched,

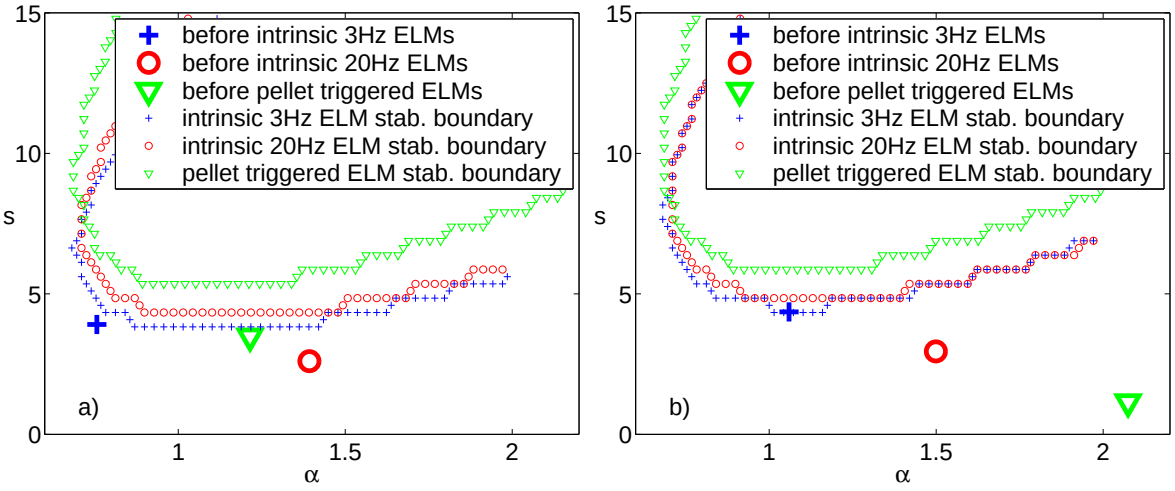

Figure 4.22: *The ballooning stability boundary and the plasma state in two radial locations, a)* $\rho = 0.97$ *and b)* $\rho = 0.98$ *for intrinsic 3 Hz ELMs, intrinsic 20 Hz ELMs and pellet triggered ELMs.*

the large intrinsic low frequency ELMs were replaced by smaller ELMs with the same frequency as the pellet launching. This chapter shows a stability analysis of plasmas with intrinsic low frequency (3 Hz) very large ELMs, intrinsic high frequency (20 Hz) ELMs and pellet triggered ELMs. Although the effect of the three dimensional ablating pellet itself can not be fully included in a two dimensional stability analysis, as a first approximation it can be assumed that the pellet is an external perturbation to the equilibrium. If the equilibrium is close to the stability limit prior to the pellet injection, it is not unreasonable to conclude that the pellet drives the plasma unstable and, thus, triggers an ELM. If the edge is far from the stability limit, the ELM-triggering mechanism of the pellet has to be something else.

Temperature and density profile data from Ref. [63] together with the analytical bootstrap current model by Sauter et al. [26] are used to create self-consistent equilibria for MHD stability analysis. In all three equilibria the shape of the plasma is identical and it is matched to the experiment. As in earlier type I and type II ELM stability analyses, we analyse the stability of the equilibria against low-n (n=3-8) peeling-ballooning modes using GATO and against n=∞ ballooning modes using IDBALL. As mentioned in earlier chapters, these are the most likely instabilities for triggering ELMs. The stability analysis results are used to explain the ELM triggering mechanism.

The n=∞ ballooning stability diagram is shown at two radial locations on the edge in Fig. 4.22. The diagram shows the stability boundaries in shear-α ($\alpha = 2Rq^2(dp/dr)/B^2$) space, as well as the location of the equilibrium in this space. There is a marked difference between the reference case with intrinsic 3 Hz ELMs and the other two. In the 3 Hz ELM case, the pressure gradient growth is limited by the tip of the ballooning stability boundary. A slight decrease in the shear would take it to the second stability region. The other two cases (intrinsic 20 Hz ELMs and pellet triggered ELMs) are deep in the 2$^{\text{nd}}$ stable region. Thus, their pressure gradient is not limited by the ballooning modes.

The low- to intermediate-n peeling mode stability is studied by varying the edge bootstrap current in the equilibria. GATO analysis shows that only the intrinsic 20 Hz ELM plasma is unstable without any current increase. The pellet triggered case is stable

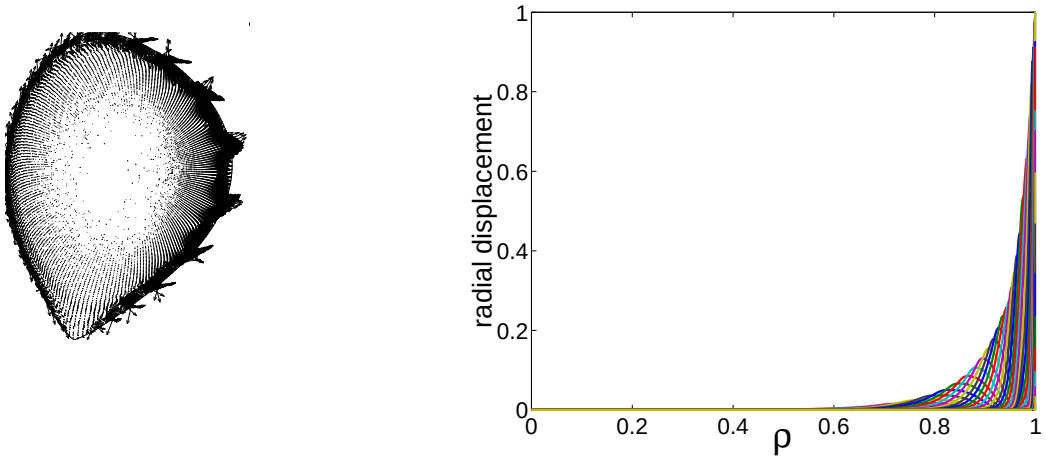

Figure 4.23: *Plasma displacement and Fourier decomposition of the radial component of the displacement ($\xi \cdot \nabla\psi$) for the $n = 8$ peeling mode in the intrinsic 20 Hz ELM plasma.*

but becomes unstable by increasing the edge current by 20 %. The intrinsic 3 Hz ELM plasma is not destabilised even by a 50 % increase in edge current. The displacement on the poloidal plane and the radial mode structure of the $n = 8$ mode are shown in Fig. 4.23 for the intrinsic 20 Hz ELMy equilibrium. The pellet-triggered equilibrium with 20 % increased edge current has similar mode structure and radial width.

Combining the differences in the high-n ballooning and low- to intermediate-n peeling-ballooning mode stability properties can give an explanation to the different ELM behaviour between the different plasmas. The intrinsic 3 Hz ELMy plasma stays limited by the first stability limit of the ballooning modes far from the stability limit of the low- to intermediate-n modes. The ELM crash completely eliminates the H-mode pedestal. Since the ELM crash occurs significantly below the low-n peeling-ballooning mode stability limit, it is likely that it is triggered by some other mechanism than the low- to intermediate-n peeling-ballooning mode that has been found in Type I ELMs. In the 3 Hz intrinsic ELMy plasma, the ELM crash is more violent than a typical Type I ELM crash, reducing the plasma energy by about 20 %. This also suggests that the triggering mechanism is different. They should be considered as very special cases of Type I ELMs or possibly not classified as Type I ELMs at all. Most likely they are short transitions back to L-mode.

On the other hand, before an ELM crash, both the intrinsic 20 Hz ELMy and pellet triggered ELMy plasmas are close to the low-n peeling-ballooning mode stability limit. Their triggering is caused by this mode with a mode structure that is localised close to the plasma edge as shown in Fig. 4.23. The ELM losses (about 5% of the plasma energy) are similar to other type I ELMs. The pellet driven plasma is still below the stability limit before the ELM crash, while the intrinsic 20 Hz plasma is already unstable. This can be explained by the fact that the pellet creates a large local perturbation that is able to trigger the instability even when the equilibrium is still slightly below the stability limit.

The active ELM triggering using pellets shows a promising way to reduce the ELM size, which could benefit ITER operation considerably. The stability analysis showed that the pellet triggered ELMs had similar characteristics as intrinsic ELMs with similar frequency.

It must be noted, however, that the 3 Hz intrinsic ELMs that the pellet triggering was able to remove, are significantly larger than normal Type I ELMs. Therefore, it is still not clear that the pellet-triggering can reduce the size of ordinary Type I ELMs to that of Type II ELMs by further increasing the launch frequency and reducing the size of a pellet.

4.5 ELMs in JET

4.5.1 Experimental observations

Several experiments have been carried out on the JET tokamak to study the ELMs [82–86]. However, only the recent JET discharges in Diagnostic Optimised Configuration (DOC) allow a detailed systematic stability analysis of the edge region using the experimental density and temperature profiles.

In JET Type I and III ELMs are routinely achieved. However, unlike in ASDEX Upgrade, so far no pure Type II ELMs have been observed. In addition to the standard Type I and Type III ELMs, H-mode operation with mixed Type I-II has been achieved [81]. Furthermore, steady-state operation with suppressed ELMs, like QHM in ASDEX Upgrade and DIII-D, has not been successful in JET.

In publication 5, the stability of various experimental JET plasmas in DOC have been analysed. Here, the methods and results are briefly summarised.

4.5.2 Equilibrium calculation

The low- to intermediate-n stability analysis of JET plasmas is conducted using the MISHKA [34] stability code, since it has been used extensively in analysing JET plasmas. In terms of computing requirements, MISHKA is also less expensive to run than GATO, allowing studies at higher toroidal mode numbers. As before, the high-n ballooning analysis is conducted using IDBALL.

In the equilibrium calculations, experimental density and temperature profiles are used. The edge density profile is obtained from the edge LIDAR system [88]. In the fitting, the interferometer data is used as a constraint for the line-averaged edge density. The core density profile is smoothed from the core LIDAR data. The electron temperature is obtained from the edge LIDAR and ECE systems. Ion temperature from the charge exchange system is found to agree with the electron temperature at the pedestal top and, thus, an assumption of $T_i = T_e$ is used to set the ion temperature in the edge region.

The equilibrium is constructed using JETTO code [32]. The bootstrap current that is important for the edge stability is calculated in JETTO using the formulation from Ref. [89]. The JETTO equilibrium is used as the basis of the stability analysis, but it can not be used as an input for the MISHKA stability code. Therefore, the equilibrium is recreated using HELENA equilibrium code with inputs of current, pressure and plasma shape from JETTO. In the stability analysis with MISHKA, the edge pressure gradient and the current are varied in HELENA to find the stability boundaries in shear-α space.

4.5.3 Edge stability within an ELM cycle

First, the stability of the equilibria just before and right after an ELM crash were compared. Figure 4.24 shows the region in shear-α parameter space, where the operational point (JETTO equilibrium values at a given flux surface) moves within an ELM cycle. In addition to the operational points before and after the ELM crash, the stability boundaries are plotted. The region unstable against low- to intermediate-n modes is marked by the number that represents the most unstable mode. The continuous line shows the n= ∞ ballooning mode stability boundary. Before an ELM the plasma is in the second stable region for the n= ∞ ballooning mode, and the operational point reaches the n=10 stability boundary. After the ELM crash, on the other hand, the plasma edge is far from the low- to intermediate-n mode stability limit, and if the edge current is assumed to be lost in the ELM crash, the edge pressure gradient becomes limited by the n= ∞ ballooning mode.

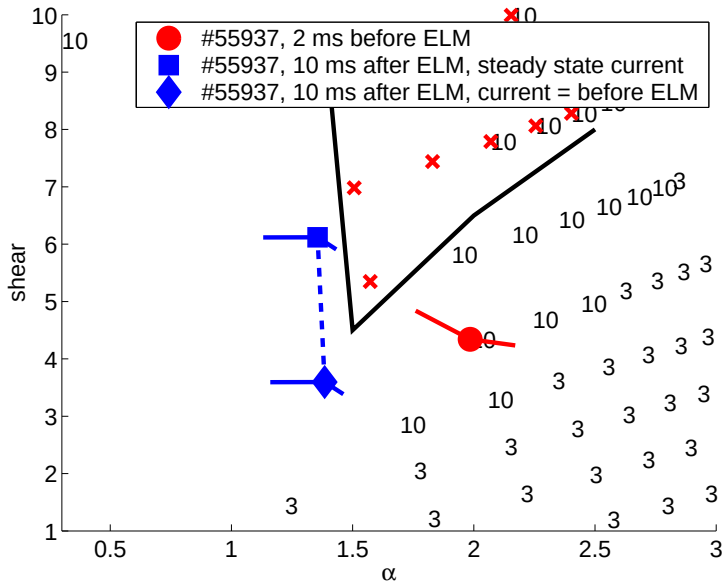

Figure 4.24: *Stability diagram in shear-α space of a Type I ELMy discharge (#55937) before and after ELM crash at ρ =0.98. At 2 ms before the ELM (red circle), the current is assumed to have reached the steady state. After the ELM, two assumptions of the edge current are used: Either the current has diffused to steady state (blue square) or the current is the same as before an ELM crash (blue diamond). The numbers represent the mode number of the most unstable mode and the solid line and the crosses shows the n=∞ ballooning mode stability boundary. The thin lines in the operational points show the error margins due to the errors in plasma profiles.*

4.5.4 External effects on the edge stability

As was found in Sec. 4.2 for ASDEX Upgrade, the ELM behaviour can be affected in various external ways. In JET experiments such methods as gas puffing, increasing heating power, changing the magnetic field strength, shaping the plasma, and puffing

impurities are used to change the ELMs. All these effects were studied in DOC except the level of triangularity which naturally requires also discharges in other configuration.

The gas puff and power scans gave almost identical results. As shown in Fig. 4.25, puffing gas or lowering the heating power makes the plasma more stable against the low- to intermediate-n peeling-ballooning modes but, at the same time moves the operational point closer to the high-n ballooning stability boundary. When the second stability access becomes very narrow or is completely closed, the pressure gradient becomes limited by the first ballooning stability, and the type of the ELMs changes from I to III.

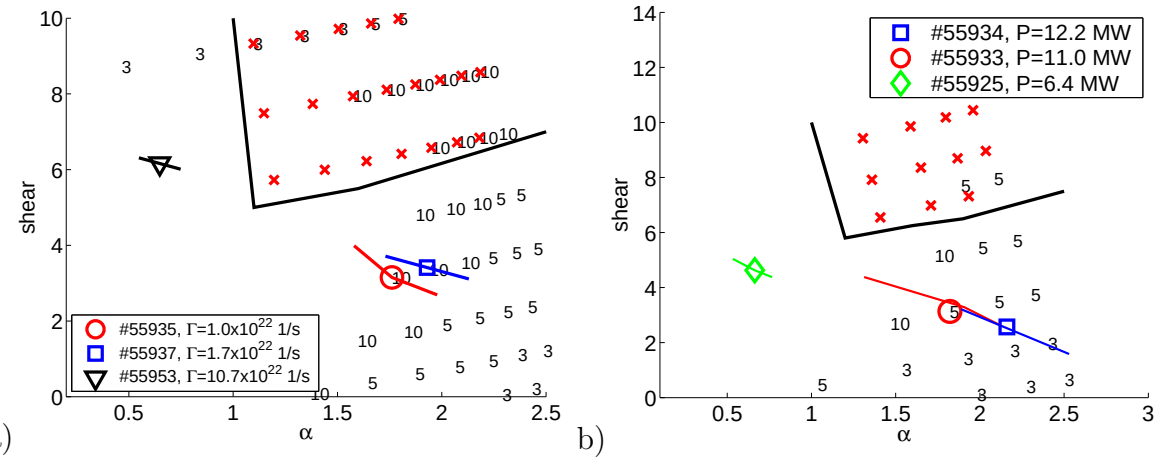

a) b)

Figure 4.25: *The α-shear stability diagram at ρ =0.99 for a) three levels of gas puffing and b) three levels of NBI power. The numbers represent the mode number of the most unstable mode and the solid line shows the n=∞ ballooning mode stability boundary. The symbols with error bars show the experimental values of shear and α for each discharge.*

Experimentally, it has been found that the frequency of the ELMs increases with increasing q_{95}. Since $q \sim B_t/B_p$, the edge stability variation with varying q_{95} is analysed by comparing discharges at three different levels of toroidal magnetic field but the same total plasma current. The edge safety factor varies from 3 to 5.2. As shown in Fig. 4.26, both the operational point and the stability boundary are shifted to higher values of α with increasing q_{95}. Since the normalisation of the pressure gradient for α is neutral for the variation of the toroidal magnetic field, the higher value of α corresponds to a steeper pressure gradient. Increasing q_{95} can therefore be seen as a way to achieve higher stable pedestal pressure.

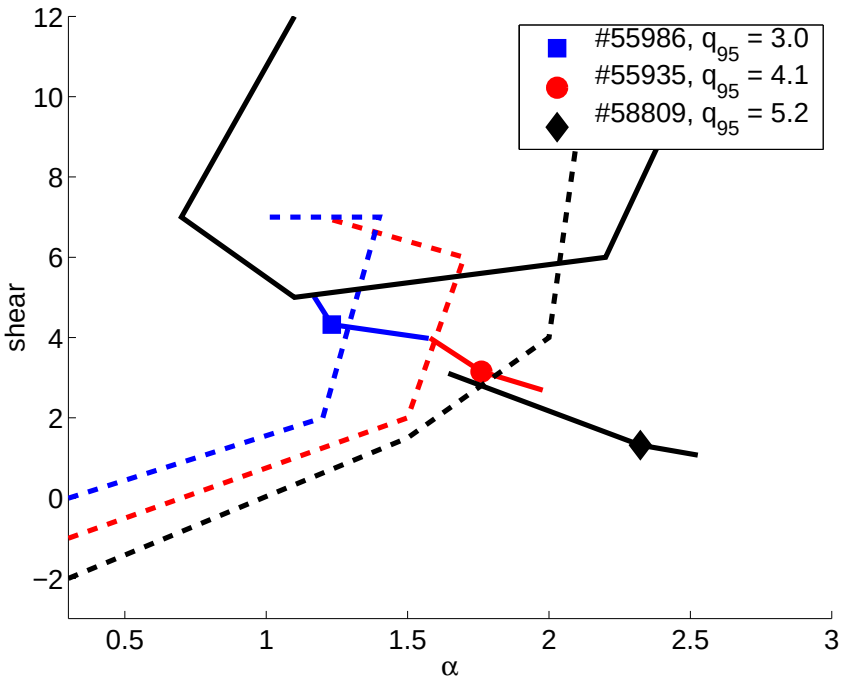

Figure 4.26: *The α-shear stability diagram at ρ =0.98 for three values of q_{95}: 3.0 and 4.1 and 5.2. The dashed lines show the low- to intermediate-n stability boundary for each value of q_{95}: 3.0 (blue), 4.1 (red) and 5.2 (black). The solid black line shows the high-n ballooning mode stability boundary. The symbols with error bars show the experimental value of shear and α of each discharge.*

Chapter 5

Summary and Conclusions

Explaining the plasma mechanisms that cause the ELMs and finding ways they can be influenced by changes in the plasma operation are fundamental problems for the safe and reliable operation of a tokamak fusion reactor. In this thesis, the ELM phenomenon has been investigated using MHD stability analyses. Most of the analyses were done using experimental data from ASDEX Upgrade and JET. In addition, stabilising effects due to plasma shaping and high poloidal β were studied using virtual plasma equilibria. The linear MHD stability analysis results presented in this thesis shed light on the nature of ELMs, explained some of the features observed in ELMs and formed a basis for the development of effective ELM control methods.

The main emphasis in the ELM research has been on the mechanism that triggers the ELMs. The model presented by Connor et al. [57] and extended by Snyder et al. [59] was chosen as a candidate for the ELM cycle. The model explains the ELM triggering as an interplay of high-n ballooning and low- to intermediate-n peeling-ballooning mode MHD instabilities that are localised in the edge of the plasma. In this thesis, the model was put into a test by analysing the linear stability of the experimental ASDEX Upgrade and JET plasmas.

The linear analysis is, of course, limited in its ability to describe the time evolution of the plasma behaviour. Consequently, it can not be expected to fully simulate the ELM cycle. However, the results of the stability analyses that set the stability boundaries and give the structure of the linear mode can give some insight also on the time evolution during the ELM cycle. The stability boundaries set the conditions where the edge plasma becomes unstable and results in ELM crash. Since the violent ELM crash is the most important part of the ELM cycle, the explanation of the mechanisms governing the ELM triggering is the key to any model for ELMs. In order to be consistent with experiments, the correct ELM model based on MHD instabilities should predict that the stability boundary is crossed just before an ELM crash.

The structure of the linear instability is likely to be associated with the transport during the crash, i.e., the transport is increased more in the regions with high mode amplitude than the regions of low amplitude. The MHD instabilities that serve as triggers in the ELM model should naturally have high amplitude in the edge region and more or less vanish in the core. A mode with a wide radial extent encompassing most of the plasma is more likely to cause a disruption than an ELM.

In the analysis of ASDEX Upgrade Type I ELMs, it was found that, indeed, the experimental pressure gradient is close to the high-n ballooning stability limit, if the

bootstrap current is low. With increasing bootstrap current, the access to second stability opened allowing the pressure gradient to steepen. However, just as predicted by the model, the edge plasma became low-n peeling-ballooning mode unstable as the bootstrap current increased. It is interesting to note that the mode numbers of the unstable modes agreed with the experimental observations for the precursors of Type I ELMs. The radial extent of the modes was limited to the edge region. It can be concluded that the stability analysis results using experimental ASDEX Upgrade Type I ELMy plasmas predict Type I ELMs to be triggered by low-n peeling-ballooning modes and, thus, agree with the studied ELM model.

In the analysis of JET plasmas, it was found that before a Type I ELM, the edge can access the second stability regime for ballooning modes. Just before an ELM, the edge is, within error margins, at the low- to intermediate-n peeling-ballooning mode stability boundary. After the ELM crash, the edge pressure gradient becomes again limited by the ballooning stability boundary. Just like in the ASDEX Upgrade stability analysis, the radial structure of the instabilities found in the JET plasmas before a Type I ELM crash is also localised in the edge region. It can be concluded that also JET Type I ELMs agree with the ELM model.

This is as far as a linear MHD can take the analysis of Type I ELM triggering mechanism. To get even further, a self-consistent transport analysis (such as simple models used in [91] and [92]) is needed for simulating the true ELM dynamics. However, the linear analysis can still be used to study how the triggering of ELMs can be influenced by adjusting the plasma operation, and what can be done to limit the detrimental effects of the ELMs. In addition, the effects of active control mechanisms on ELM triggering can be investigated using MHD stability analysis.

In this thesis, several ways to affect the ELMs have been investigated. The stability of the ASDEX Upgrade Type II ELMy plasma was compared with the Type I ELMy plasma. The changes in the plasma operating conditions (the level of triangularity, density, safety factor at the edge, and the double null configuration) were tested independently.

Increasing the triangularity increased the plasma stability against the ELM-triggering low-n peeling-ballooning mode (higher edge bootstrap current was needed to destabilise the plasma). When high triangularity was combined with the increase in the edge safety factor, the mode structure of the instability became significantly more localised into the edge region. The increasing density with constant pressure decreased the bootstrap current in the edge because of the increasing collisionality. This had a further stabilising effect on the low- to intermediate-n peeling-ballooning modes. Furthermore, it made the second stability access narrower for the high-n ballooning modes. Consequently, the low-n modes may not become unstable at all, and the ELM is triggered by a narrower intermediate-n mode. The almost double-null configuration makes the instability even more localised at the edge.

When all these effects are combined and the assumption that the magnitude of the ELM is proportional to the width of the instability is used, it can be concluded that the ELMs triggered in the Type II ELM conditions are smaller than those of the Type I ELMy plasma. This is exactly what is seen in the experiments and the ELM model seems to work very well with Type II ELMs in ASDEX Upgrade.

In addition to the stability analyses with experimental data, a stability analysis using equilibria with virtual plasma profiles was conducted to investigate the effect of the global poloidal β on the edge stability. In JT-60U, it had been observed that high pedestal

pressure can be achieved with high values of global β_p. With high β_p, also the ELMs tend to become smaller. In the stability analysis, the edge profiles were kept fixed and the core pressure was increased. It was found that in plasmas with high triangularity, the increasing β_p stabilises the low- and intermediate-n peeling-ballooning modes. This allows increasing the edge pressure gradient without triggering an ELM. The stabilising effect of high β_p was found to be reduced with low triangularity. The stability analysis results can explain the higher pedestal pressures observed in high-β_p high-triangularity discharges.

The ELMs in JET were also investigated with various changes in the plasma conditions. The stability analysis of the gas puff scan showed how the second stability access for high-n ballooning modes closed when the gas puffing was increased, and the ELMs changed from large Type I ELMs to smaller Type III ELMs with poorer confinement. On the other hand, the increased gas puffing also stabilised the low- to intermediate-n peeling-ballooning modes. The power scan had a very similar effect on the stability. The increasing heating power moved the operational point of the edge plasma into the unstable region of the low- to intermediate-n modes while at the same time widened the second stability access for high-n ballooning modes. Since the Type III ELMs are far from the stability boundary of the low- to intermediate-n modes, it is unlikely that they are destabilised by the same mechanism as the Type I ELMs. This can also explain their smaller size. The poor confinement that is generally observed with Type III ELMs can be due to the fact that, in the operational space, the edge plasma is limited to the first stability region.

The active ELM control mechanism investigated in this thesis was the launching of small pellets from the high field side. The active ELM control by launching pellets is a relatively new idea and will require more experimenting to prove its true value, but the current results are already encouraging. The impurity injection has been used as a way to affect the ELMs and to mitigate the ELM effects on the divertors. The study of the pellet injection discharges in ASDEX Upgrade showed that, from the edge MHD stability point of view, the small ELMs triggered by the small pellets are very similar to the intrinsic ELMs of the same frequency and differ considerably from the large ELMs that occurred in the reference plasma without the pellets. Unlike in the intrinsic ELMy plasma, however, the plasma with launched pellets is in the stable region before an ELM, and the pellet itself is needed to drive the edge unstable and trigger an ELM. To further investigate this, three dimensional modelling of the pellet plasmoid would be required. Even from the two dimensional analysis it can be concluded that the pellet launching appears a very promising way to mitigate ELM effects, and it can possibly still be improved with smaller pellets and even higher launching frequency.

In addition to ELMy plasmas, the quiescent H-mode (QHM), an operating mode without ELMs but with good confinement, was also investigated using the MHD stability analysis. In the comparison between an ELMy H-mode and QHM, it was found that higher pressure gradient is required for the destabilisation of the QHM. However, the slightly improved stability does not fully explain why the QHM plasma does not reach the stability limit and what is the role of the reversed neutral beam direction. Further work is also required to explain the observed MHD oscillations in QHM that can play a role in preventing the edge pressure gradient from steepening even further and causing an ELM crash.

The stability studies shown in this thesis give some insight into the highly complicated nature of the ELM phenomenon. The linear stability studies, especially the peeling-

ballooning analyses, presented in this thesis should be still complemented with analyses at higher mode numbers (n>10) that were neglected due to computational restrictions of the GATO code. In order to further improve the understanding of the ELMs, the results from the linear stability analyses should be used in a transport analysis to develop a model that can predict what happens at the edge after an ELM crash. The stability analysis methods themselves should also be improved to include some important effects from the particle description of plasma, such as stabilisation due to the finite larmor radii that can start playing a role when the pressure gradient becomes very steep, and the ion orbit loss driven currents that can affect the current profile at the very edge.

Even though the theoretical explanation of all the aspects of ELMs is still far from complete, the stability analyses have shown what kind of a role the MHD instabilities play in the triggering of ELMs. They also revealed how the instabilities can be affected with the changes in plasma and how these effects change the ELMs themselves. More work is still needed for instance incorporating the plasma rotation in the stability analysis. Many plasmas heated by neutral beams rotate at high speed which can affect the edge stability. In the future, this will hopefully lead to a complete understanding of the ELMs and also allow to develop tools to control the edge plasma so that the detrimental effects of ELMs can be avoided without sacrificing the plasma performance of a fusion reactor.

Chapter 6

Appendix: Ideal MHD equations

6.1 Kinetic picture of plasma

The ideal MHD equations can be derived starting from the Boltzmann equation for each species:

$$\frac{\partial f_\alpha}{\partial t} + \mathbf{u}\cdot\nabla f_\alpha + \frac{q_\alpha}{m_\alpha}(\mathbf{E}+\mathbf{u}\times\mathbf{B})\cdot\nabla_u f_\alpha = \left[\frac{\partial f_\alpha}{\partial t}\right]_c, \tag{6.1}$$

and the Maxwell's equations:

$$\begin{aligned}
\nabla\times\mathbf{E} &= -\frac{\partial\mathbf{B}}{\partial t}, && (6.2)\\
\nabla\cdot\mathbf{B} &= 0, && (6.3)\\
\nabla\times\mathbf{B} &= \mu_0\mathbf{J} + \frac{1}{c^2}\frac{\partial\mathbf{E}}{\partial t},\\
&= \mu_0\sum_\alpha q_\alpha\int\mathbf{u}f_\alpha d\mathbf{u} + \frac{1}{c^2}\frac{\partial\mathbf{E}}{\partial t}, && (6.4)\\
\nabla\cdot\mathbf{E} &= \frac{\sigma}{\epsilon_0} = \frac{1}{\epsilon_0}\sum_a q_\alpha\int f_\alpha d\mathbf{u}. && (6.5)
\end{aligned}$$

Here, the function $f_\alpha = f_\alpha(\mathbf{r},\mathbf{u},t)$ is the distribution function, q_α is the charge and m_α mass of species α. $\mathbf{u}$ is the velocity of the particle. For electromagnetic quantities the conventional notation is used, i.e. $\mathbf{B}$ is the magnetic field, $\mathbf{E}$ is the electric field, $\mathbf{J}$ is the current density, σ is the charge density, ϵ is the vacuum permittivity, μ_0 is the vacuum permeability, and c is the speed of light.

The right hand side of Eq. 6.1 represents changes in the distribution function due to collisions between particles. It is defined as

$$\left[\frac{\partial f_\alpha}{\partial t}\right]_c = \sum_\beta C_{\alpha\beta}, \tag{6.6}$$

where $C_{\alpha\beta}$ describes the collision rate of particle species α with particle species β.

Three conservation laws apply to the collisions, namely conservation of particles, momentum and energy. The conservation of particles implies

$$\int C_{ee}d\mathbf{u} = \int C_{ii}d\mathbf{u} = \int C_{ei}d\mathbf{u} = \int C_{ie}d\mathbf{u} = 0, \tag{6.7}$$

the conservation of momentum in collisions between like particles implies

$$\int m_e \mathbf{u} C_{ee} d\mathbf{u} = \int m_i \mathbf{u} C_{ii} d\mathbf{u} = 0, \tag{6.8}$$

while, the conservation of energy in collisions between like particles implies

$$\int \frac{1}{2} m_e u^2 C_{ee} d\mathbf{u} = \int \frac{1}{2} m_i u^2 C_{ii} d\mathbf{u} = 0. \tag{6.9}$$

Finally, the conservation of total momentum in collisions between unlike particles implies

$$\int (m_e \mathbf{u} C_{ei} + m_i \mathbf{u} C_{ie}) d\mathbf{u} = 0, \tag{6.10}$$

and the conservation of total energy in collisions between unlike particles implies

$$\int \frac{1}{2} (m_e u^2 C_{ei} + m_i u^2 C_{ie}) d\mathbf{u} = 0. \tag{6.11}$$

6.2 Two fluid equations

Taking velocity moments of the Boltzmann equation gives the mass, momentum and energy equations. The mass equation is obtained by integrating the Boltzmann equation over the velocity space:

$$\int \left[\frac{df_\alpha}{dt} - \left(\frac{\partial f_\alpha}{\partial t} \right)_c \right] d\mathbf{u} = 0 \Rightarrow \frac{\partial n_\alpha}{\partial t} + \nabla \cdot n_\alpha \mathbf{v}_\alpha = 0. \tag{6.12}$$

Multiplying the Boltzmann equation by particle momentum and integrating over the velocity space gives the momentum equation:

$$\int m_\alpha \mathbf{u} \left[\frac{df_\alpha}{dt} - \left(\frac{\partial f_\alpha}{\partial t} \right)_c \right] d\mathbf{u} = 0 \tag{6.13}$$

$$\Rightarrow \frac{\partial}{\partial t}(m_\alpha n_\alpha \mathbf{v}_\alpha) + \nabla (m_\alpha n_\alpha \langle \mathbf{u}\mathbf{u} \rangle) - q_\alpha n_\alpha (\mathbf{E} + \mathbf{v}_\alpha \times \mathbf{B}) = \int m_\alpha \mathbf{u} C_{\alpha\beta} d\mathbf{u},\ \alpha \neq \beta, \tag{6.14}$$

Finally, the second moment (multiplication by $1/2 m_\alpha u^2$ and integration over velocity space) gives the energy equation:

$$\int \frac{1}{2} m_\alpha u^2 \left[\frac{df_\alpha}{dt} - \left[\frac{\partial f_\alpha}{\partial t} \right]_c \right] d\mathbf{u} = 0 \tag{6.15}$$

$$\Rightarrow \frac{\partial}{\partial t}(\frac{1}{2} m_\alpha n_\alpha \langle u^2 \rangle) + \nabla \cdot (\frac{1}{2} m_\alpha n_\alpha \langle u^2 \mathbf{u} \rangle) - q_\alpha n_\alpha \mathbf{v} \cdot \mathbf{E} = \int \frac{1}{2} m_\alpha u^2 C_{\alpha\beta} d\mathbf{u},\ \alpha \neq \beta. \tag{6.16}$$

Here n_α is the number density of the particle species α, and $\mathbf{v}_\alpha$ is the macroscopic fluid velocity. Their definitions are

$$\begin{aligned} n_\alpha &\equiv \int f_\alpha d\mathbf{u} \\ \mathbf{v}_\alpha &\equiv \frac{1}{n_\alpha} \int \mathbf{u} f_\alpha d\mathbf{u}. \end{aligned} \tag{6.17}$$

The brackets $\langle\,\rangle$ are defined as averages

$$\langle Q\rangle \equiv \frac{1}{n_\alpha}\int Q f_\alpha d\mathbf{u}. \tag{6.18}$$

The random motion of the particles can be described with a new variable $\mathbf{w} = \mathbf{u} - \mathbf{v}_\alpha$. By definition $\langle \mathbf{w}\rangle = 0$. Before writing the fluid equations in terms of physical macroscopic quantities, it is useful to introduce the scalar pressure,

$$p_\alpha \equiv \frac{1}{3} m_\alpha n_\alpha \langle w^2\rangle, \tag{6.19}$$

the total pressure tensor,

$$\overline{P}_\alpha \equiv m_\alpha n_\alpha \langle \mathbf{w}\mathbf{w}\rangle, \tag{6.20}$$

the anisotropic part of the pressure tensor

$$\overline{\Pi}_\alpha \equiv \overline{P}_\alpha - p_\alpha \overline{I}, \tag{6.21}$$

the temperature,

$$T_\alpha \equiv \frac{p_\alpha}{n_\alpha}, \tag{6.22}$$

the heat flux due to random motion,

$$h_\alpha \equiv \frac{1}{2} m_\alpha n_\alpha \langle w^2 \mathbf{w}\rangle, \tag{6.23}$$

the mean momentum transfer between unlike particles,

$$\mathbf{R}_\alpha \equiv \int m_\alpha \mathbf{w} C_{\alpha\beta} d\mathbf{w}, \tag{6.24}$$

and the heat generated due to collisions between unlike particles,

$$Q_\alpha \equiv \int \frac{1}{2} m_\alpha w_\alpha^2 C_{\alpha\beta} d\mathbf{w}. \tag{6.25}$$

Using these definitions and limiting to two fluids, the two-fluid equations can be written in the form:

$$\frac{dn_\alpha}{dt} + n_\alpha \nabla\cdot\mathbf{v}_\alpha = 0, \tag{6.26}$$

$$m_\alpha n_\alpha \frac{d}{dt}\mathbf{v}_\alpha - q_\alpha n_\alpha(\mathbf{E} + \mathbf{v}_\alpha \times \mathbf{B}) + \nabla\cdot\overline{P}_\alpha = \mathbf{R}_\alpha, \tag{6.27}$$

$$\frac{3}{2} n_\alpha \frac{dT_\alpha}{dt} + \overline{P}_\alpha : \nabla\mathbf{v}_\alpha + \nabla\cdot\mathbf{h}_\alpha = Q_\alpha, \tag{6.28}$$

$$\nabla\times\mathbf{E} = -\frac{\partial\mathbf{B}}{\partial t}, \tag{6.29}$$

$$\nabla\times\mathbf{B} = \mu_0 e(n_i\mathbf{v}_i - n_e\mathbf{v}_e) + \frac{1}{c^2}\frac{\partial\mathbf{E}}{\partial t}, \tag{6.30}$$

$$\nabla\cdot\mathbf{E} = \frac{e}{\epsilon_0}(n_i - n_e), \tag{6.31}$$

$$\nabla\cdot\mathbf{B} = 0. \tag{6.32}$$

For simplicity, singly charged ions were assumed. If $Z_\alpha > 1$, the multiplication of n_α by electron charge e in Eqs. (6.29) and (6.31) is replaced by $Z_\alpha e$.

The above set of equations (6.26,6.27,6.28,6.29,6.30,6.31,6.32) describes the plasma exactly, but is useless for practical purposes, since the heat transfer between particles Q_α is higher order. Another equation could be obtained by taking even higher moment of the Boltzmann equation. This procedure produces the heat equation, which could be used to solve for Q_α. However, it would introduce yet another unknown quantity of even higher order. To make practical use of the equations, the sequence has to be closed at some point. This is done using a few approximations. While the approximations allow to make better use of the equations, they also limit the validity of the theory. This has to be kept in mind when the equations are used in practical problems.

6.3 Approximations

In full Maxwell's equations, there are two components that are responsible for high-frequency phenomena. The charge separation in Eq. (6.31) creates plasma oscillations that have very high frequency (recall the electron plasma period in Table 2.1). Another high-frequency oscillation comes from the second term of the right-hand side of Eq. (6.30). The ratio between the second and the first term is proportional to the frequency of the phenomenon, since $\partial/\partial t \approx \omega$. In low frequency cases, the second term can be neglected. Physically, this means that the electromagnetic waves of interest have phase velocities much slower than the speed of light, $\omega/k \ll c$.

Both Eqs. (6.31) and (6.30) can be transformed into low-frequency equations by letting $\epsilon_0 \to 0$. This eliminates the high-frequency components, i.e., the displacement current $\epsilon_0 \partial \mathbf{E}/\partial t$ and the charge density $\epsilon_0 \nabla \cdot \mathbf{E}$. The elimination of $\epsilon_0 \nabla \cdot \mathbf{E}$ means that there can not be any net charge anywhere in the plasma. Because of zero net charge, there is no charge separation, and it is possible to define $n_i = n_e \equiv n$. However, here it must be noted that neglecting the charge separation restricts the length scale of the phenomena to larger than the Debye length, $\lambda_d = V_{Te}/\omega_{pe}$. Remembering that, in MHD, only large-scale low-frequency phenomena are considered, these assumptions are well justified.

It is possible to simplify the momentum equation (6.27) by neglecting the electron inertia, i.e., $m_e \to 0$. This means that the motion of the plasma is determined by the ions, and the electrons respond infinitely fast on the time scales of interest. Again, this approximation restricts the time and length scales of the phenomena that can be treated with MHD. The time scales have to longer than the electron plasma period $\tau_{pe} = (m_e/4\pi n_e e^2)^{1/2}$ and the electron gyro period $\tau_{ce} = m_e/eB$, and the length scales have to be larger than the Debye length and the electron gyro radius $r_e = V_{Te}/\omega_{ce}$. Again, for MHD phenomena in fusion plasmas these conditions are satisfied.

6.4 Single fluid equations

After simplifying the exact equations by eliminating the high-frequency phenomena and the electron inertia, a set of equations that describe the behaviour of a single fluid is obtained. The fluid motion is determined by the ion motion and the electrons follow infinitely fast. In writing the equations, single-fluid variables will be used instead of

variables that refer to particle species. Instead of using the number density, the mass density is introduced,

$$\rho = m_i n, \tag{6.33}$$

where the mass of electrons was neglected as assumed above. The current density is defined as

$$\mathbf{J} = en(\mathbf{v}_i - \mathbf{v}_e). \tag{6.34}$$

Since the inertia of electrons is neglected, the momentum of the fluid is carried by ions. The fluid velocity is defined as

$$\mathbf{v} = \mathbf{v}_i. \tag{6.35}$$

The electron velocity can then be expressed as

$$\mathbf{v}_e = \mathbf{v} - \mathbf{J}/en. \tag{6.36}$$

The total pressure and temperature of the fluid are defined as

$$p = nT = p_e + p_i, \tag{6.37}$$
$$T = T_e + T_i. \tag{6.38}$$

Using these definitions, the single-fluid MHD equations can be written. The first of the single-fluid equations, conservation of mass, comes from the first of the two-fluid equations, Eq. (6.26), for ions when it is multiplied by ion mass,

$$\frac{\partial \rho}{\partial t} + \nabla \cdot \rho \mathbf{v} = 0. \tag{6.39}$$

Alternatively, by multiplying the same equation by the elementary charge e, writing it separately for electrons and ions and then subtracting, yields

$$\nabla \cdot \mathbf{J} = 0, \tag{6.40}$$

which represents the conservation of charge.

From the definition of R_α, Eq. (6.24, it can be seen that $R_e = -R_i$. Then writing the momentum equation separately for electrons and ions and adding them together leads to the equation

$$\rho \frac{d\mathbf{v}}{dt} - \mathbf{J} \times \mathbf{B} + \nabla p = -\nabla \cdot (\overline{\Pi}_i + \overline{\Pi}_e), \tag{6.41}$$

where the effect of the electric field was eliminated by charge neutrality. The anisotropic part of the pressure is dominated by the viscosity terms. Without going into details (see Ref. [17]), the largest terms in Eq. (6.41) are the ion viscosity terms that are of the order

$$\overline{\Pi}_{ii} \sim n T_i \tau_{ii} V_{Ti}/a, \tag{6.42}$$

where τ_{ii} is the ion-ion collision time. If it is assumed that the plasma is collisional, i.e.,

$$V_{Ti}\tau_{ii}/a \ll 1, \tag{6.43}$$

then the approximation

$$\frac{\nabla \cdot \overline{\Pi}_i}{\nabla p} \sim \frac{V_{Ti}\tau_{ii}}{a} \ll 1, \tag{6.44}$$

can be made. This allows neglecting the right hand side of Eq. (6.41).

Also the electron momentum equation can be written in single-fluid variables, yielding

$$\mathbf{E} + \mathbf{v} \times \mathbf{B} = \frac{1}{en}(\mathbf{J} \times \mathbf{B} - \nabla p_e - \nabla \cdot \overline{\Pi}_e + \mathbf{R}_e). \tag{6.45}$$

The left-hand side of Eq. (6.45) is the Ohm's law for perfectly conducting material. In ideal MHD, perfect conductivity is assumed, and the right-hand side should vanish. Indeed, the right-hand side becomes negligible with the following assumptions. First, the viscosity term is neglected under the same conditions as above. Second, neglecting the right-hand side of Eq. (6.41) and multiplying it by $1/(en)$, it can be seen that

$$\frac{1}{en}(\mathbf{J} \times \mathbf{B} - \nabla p_e) = \frac{1}{en}(\mathbf{J} \times \mathbf{B} - \nabla p + \nabla p_i) = \frac{1}{en}(\rho \frac{\partial \mathbf{v}}{\partial t} + \nabla p_i). \tag{6.46}$$

The first term, $\rho/(en)\partial \mathbf{v}/\partial t$, is comparable to ω/ω_{ci} times $|\mathbf{v} \times \mathbf{B}|$. For low frequencies ($\omega \ll \omega_{ci}$) it can be neglected. The second term, $\nabla p_i/en$, is compared with $\mathbf{v} \times \mathbf{B}$, resulting

$$\begin{aligned} |\nabla p_i/en| &\sim \frac{T_i}{ae} \sim \frac{m_i V_{Ti}^2}{ae}, \\ |\mathbf{v} \times \mathbf{B}| &\sim V_{Ti}B, \\ \Rightarrow \frac{|\nabla p_i|/en}{|\mathbf{v} \times \mathbf{B}|} &\sim \frac{r_i}{a}, \end{aligned} \tag{6.47}$$

where $r_i = V_{Ti}/\omega_{ci}$ is the ion gyro radius. Thus, in order to be able to neglect $\mathbf{J} \times \mathbf{B}$ and ∇p_e terms, one has to assume that

$$\frac{r_i}{a} \ll 1, \text{or } \frac{\omega}{\omega_{ci}} \ll 1. \tag{6.48}$$

This is the previous condition that the frequency of the MHD phenomenon has to be lower than the ion gyro frequency and the length scales larger than the ion gyro radius.

The last term in the electron momentum equation is $\mathbf{R}_e/en$ representing the collisions between electrons and ions. It is dominated by electrical resistivity and, using transport theory, can be written as

$$\frac{1}{en}\mathbf{R}_e \sim \eta \mathbf{J}, \tag{6.49}$$

where the resistivity η is

$$\eta \sim \frac{m_e}{ne^2\tau_{ei}}. \tag{6.50}$$

The momentum equation yields a scaling $|\mathbf{J}| \sim |\nabla p|/|\mathbf{B}|$. Now, a condition for the last term in Eq. (6.45) to be neglected can be written as

$$\frac{\eta|\mathbf{J}|}{|\mathbf{v} \times \mathbf{B}|} \sim \frac{\eta|\nabla p|/|\mathbf{B}|}{|\mathbf{v} \times \mathbf{B}|} \sim \frac{(m_e/m_i)^{1/2}}{\omega\tau_{ii}} \left(\frac{r_i}{a}\right)^2 \ll 1, \tag{6.51}$$

where $1/\omega \sim a/V_{Ti}$ is the typical time scale for MHD phenomena. Also the relation between collision times of electrons and ions $\tau_{ei} \sim \tau_{ee} \sim \tau_{ii}(m_e/m_i)^{1/2}$ was used. In Eq. (6.51), the collision time is in the denominator, which means that while the earlier conditions required plasma to be collisional, there should not be too many collisions. Otherwise, the plasma is not ideal, and the resistive diffusion should be included.

Using some algebra and the definition of the ratio of specific heats ($\gamma = \frac{5}{3}$), the remaining equations for ions and electrons (Eq. (6.28)) can be written in the form

$$\frac{d}{dt}\left(\frac{p_i}{\rho^\gamma}\right) = \frac{2}{3\rho^\gamma}(Q_i - \nabla\cdot\mathbf{h}_i - \overline{\Pi}_i : \mathbf{v}), \tag{6.52}$$

$$\frac{d}{dt}\left(\frac{p_e}{\rho^\gamma}\right) = \frac{2}{3\rho^\gamma}\left[Q_e - \nabla\cdot\mathbf{h}_e - \overline{\Pi}_e : \left(\mathbf{v} - \frac{\mathbf{J}}{en}\right)\right] + \frac{1}{en}\mathbf{J}\cdot\nabla\left(\frac{p_e}{\rho^\gamma}\right). \tag{6.53}$$

The last term in the electron equation comes from $(d/dt)_e = (d/dt) - (\mathbf{J}/en)\cdot\nabla$. Again the right-hand side of these equations can be neglected under certain conditions. The terms containing anisotropic pressure as well as the last term of the electron energy equation become negligible with the assumptions that have already been used. The heat flux is dominated by the conduction along the field lines and can be written as

$$\mathbf{h}_j \approx -k_{\|j}\nabla_\| T_j, \tag{6.54}$$

where $k_{\|j}$ is the parallel conductivity of the fluid of particle type j. Neglecting the joule heating in the collisional heating terms Q_j due to assumed negligible resistivity, only electron and ion energy equilibration contributes to Q_j. They can be written as

$$Q_e = \frac{n(T_e - T_i)}{\tau_{eq}}, \tag{6.55}$$

$$Q_i = -\frac{n(T_e - T_i)}{\tau_{eq}}, \tag{6.56}$$

where τ_{eq} is the energy equilibration time that is proportional to the ion-ion collision time with a relation

$$\tau_{eq} \sim \left(\frac{m_i}{m_e}\right)^{1/2}\tau_{ii}. \tag{6.57}$$

In order to neglect the terms containing Q_j, the condition $\omega\tau_{eq} \ll 1$ has to be fulfilled. Then $T_e \approx T_i$.

The transport theory (see for instance Ref. [1]) gives the parallel thermal conductivity as $k_{\|e} \sim nT_e\tau_{eq}/m_e$ for electrons and a value smaller by a factor of $(m_e/m_i)^{1/2}$ for ions. Adding the energy equations and neglecting the ion thermal conduction terms yields the equations

$$\frac{d}{dt}\left(\frac{p}{\rho^\gamma}\right) = \frac{1}{3\rho^\gamma}\nabla_\|\cdot(nT\tau_{eq}/m_e\nabla_\| T). \tag{6.58}$$

Here $T_e = T_i = T/2$ was used. The right hand side is negligible with the same condition as was used to neglect collisional heating terms, i.e. $\omega\tau_{eq} \ll 1$. It can be written out as

$$\omega\tau_{eq} \sim \left(\frac{m_i}{m_e}\right)^{1/2}\frac{V_{Ti}\tau_{ii}}{a} \ll 1 \tag{6.59}$$

It is easy to notice that this is even more restrictive condition than that obtained from the dominance of collisions in the momentum equation.

The ideal MHD equations can now be written as

$$\frac{\partial \rho}{\partial t} + \nabla \cdot \rho \mathbf{v} = 0, \tag{6.60}$$

$$\rho \frac{d\mathbf{v}}{dt} - \mathbf{J} \times \mathbf{B} + \nabla p = 0, \tag{6.61}$$

$$\frac{d}{dt}\left(\frac{p}{\rho^\gamma}\right) = 0, \tag{6.62}$$

$$\mathbf{E} + \mathbf{v} \times \mathbf{B} = 0, \tag{6.63}$$

$$\nabla \times \mathbf{E} = -\frac{\partial \mathbf{B}}{\partial t}, \tag{6.64}$$

$$\nabla \times \mathbf{B} = \mu_0 \mathbf{J}, \tag{6.65}$$

$$\nabla \cdot \mathbf{B} = 0. \tag{6.66}$$

6.5 Boundary conditions for MHD problems in fusion devices

To use the ideal MHD equations derived above for practical purposes, boundary conditions need to be defined. In a modern tokamak, the plasma is inside a conductive wall. Between the plasma and the wall, there is a region that can treated as vacuum, where $p = 0$. Since there are no currents in vacuum, the following equations define the vacuum magnetic field $\hat{\mathbf{B}}$:

$$\nabla \times \hat{\mathbf{B}} = 0, \tag{6.67}$$

$$\nabla \cdot \hat{\mathbf{B}} = 0. \tag{6.68}$$

On the surface of a perfectly conductive wall, the boundary condition is

$$\mathbf{n} \cdot \hat{\mathbf{B}}|_{\text{wall}} = 0, \tag{6.69}$$

where $\mathbf{n}$ refers to the normal vector of the wall. At the plasma boundary, the condition

$$\mathbf{n} \cdot \hat{\mathbf{B}}|_{surf} = \mathbf{n} \cdot \mathbf{B}|_{\text{surf}} \tag{6.70}$$

must be satisfied, because the boundary is a flux surface with a constant pressure.

Plasma surface is free to move into the vacuum and, consequently, the normal component of the velocity can be continuous across the boundary. Substituting Ampère's law into the momentum equation and integrating over the surface gives

$$\left[p + \frac{B^2}{2}\right]_{\text{surf}} = 0, \tag{6.71}$$

where $[X]_{surf}$ denotes the change across the boundary, i.e. $\hat{X} - X$. Similarly the Ampère's law gives

$$[\mathbf{n} \times \mathbf{B}]_{\text{surf}} = \mu_0 \mathbf{K}, \tag{6.72}$$

where $\mathbf{K}$ is the surface current density. If there are neither surface currents nor jumps in the pressure, these conditions require that the all the component of the magnetic field are continuous.

Bibliography

[1] Wesson J., *Tokamaks* 2nd. ed., Oxford Science Publications, Oxford 1997.

[2] Keilhacker M. et al., "High fusion performance from deuterium-tritium plasmas in JET", Nuclear Fusion **39** (1999) 209.

[3] Rebut P.H., Keen B.E., "Design, construction, and first operational experience on the Joint European Torus (JET)", Fusion Technology **1** (1987) 1.

[4] Kitsumezaki A. et al. "JT-60 program", Fusion Science and Technology **42** (2002) 179.

[5] Sykes, A., et al, "First results from MAST", Nuclear Fusion **41** (2001) 1423.

[6] Ono M., et al., " Exploration of spherical torus physics in the NSTX device", Nuclear Fusion **40** (2000) 557.

[7] *http://www.iter.org/ITERPublic/ITER/con_text.html as by 29/11/2004.*

[8] *http://www.naka.jaeri.go.jp/ITER/FDR/ as by 29/11/2004.*

[9] Pitcher C.S., Stangeby P.C, "Experimental divertor physics", Plasma Physics and Controlled Fusion **39** (1997) 779.

[10] Janeschitz G. et al., "Divertor design and its integration into ITER", Nuclear Fusion **42** (2002) 14.

[11] The JET Team, "The Route to High Performance on JET", Plasma Physics and Controlled Fusion **37** (1995) A359.

[12] Leonard, A.W., et al., "Impact of ELMs on the ITER divertor", J. Nucl Mater.**266-269** (1999) 109.

[13] Wagner, F., et al., "H-mode of W7-AS Stellarator", Plasma Phys. Control. Fusion **36** (1994) A61.

[14] Kirk, A., et al.,"ELM characteristics in MAST",Plasma Phys. Control. Fusion **46** (2004) 551.

[15] Cowley, S.C., Wilson, H., Hurricane, O., Fong, B.,"Explosive instabilities: from solar flares to edge localized modes in tokamaks", Plasma Phys. Control. Fusion **45** (2003) A31.

[16] J. P. Freidberg, *Ideal Magnetohydrodynamics*, Plenum Press, New York, 1987.

[17] S. I. Braginskii, Reviews of Plasma Physics, edited by M. A. Leontovich, Vol I, Consultants Bureau, New York (1965).

[18] Grad, H., Rubin, H. Proceedings of the Second United Nations International Conference on the Peaceful Uses of Atomic Energy 1958, United Nations, Geneva, **31**, 190.

[19] Shafranov, V.D., Soviet Physics, JETP **26** (1960) 682.

[20] Bickerton, R.J., Connor, J.W., Taylor, J.B, "Diffusion Driven Plasma Currents and Bootstrap Tokamak", Nature Phys. Sci. **229** (1971) 110.

[21] Zarnstorff, M.C., et al.,"Bootstrap current in TFTR", Phys. Rev. Lett. **60** (1988) 1306.

[22] Corday, J.G., et al.,"Bootstrap current theory and experimental evidence", Plasma Phys. **80** (1988) 1625.

[23] Peeters, A.G., "The bootstrap current and its consequences", Plasma Phys. and Contr. Fusion **42** (2000) B231.

[24] Kessel, C., "Bootstrap current in a tokamak" Nuclear Fusion, 34 (1994), 1221.

[25] Wilson, H.R., UKAEA Report Fus 271 (1994).

[26] Sauter, O., Angioni, C., Lin-Liu, Y.R., "Neoclassical conductivity and bootstrap current formulas for general axisymmetric equilibria and arbitrary collisionality regime" Phys. of Plasmas, **6** (1999) 2834.

[27] Greene, J.M., Johnson J.L., "Interchange instabilities in ideal hydromagnetic theory", Plasma Physics **10**(1968) 729.

[28] Frieman, E.A., Greene, J.M., Johnson, J.L., Weimer, K.E., "Toroidal effects on magnetohydrodynamic modes in tokamaks", Phys. of Fluids **16** (1973) 1108.

[29] Lortz, D., "The General Peeling Instability", Nucl. Fusion **15** (1975) 49.

[30] Connor, J.W., Hastie, R.J. and Taylor, J.B.,"Shear, Periodicity and, Plasma Ballooning Modes", Phys. Rev. Lett. **40** (1978) 396.

[31] Miller, R.L., Lin-Liu, Y.R., Osborne, T.H. and Taylor, T.S., "Ballooning mode stability for self-consistent pressure and current profiles at the H-mode edge", Plasma Phys. Control. Fusion **40** (1998) 753.

[32] Cennachi, G. , Taroni, A., JET-IR(88)03 (1998).

[33] Bernard, L.C., Helton, F.J., Moore, R.W., Comp. Phys. Comm. "GATO: An MHD Stability Code for Axisymmetric Plasmas with Internal Separatrices", **24** (1981) 377.

[34] A.B. Mihailovskii et al., Plasma Phys. Rep. **23** (1999) 844.

[35] Oja, R., Special assginment in Helsinki University of Technology, 2004.

[36] Connor, J.W., Hastie, R.J. and Taylor, J.B.,"High mode number stability of an axisymmetric toroidal plasma", Proc. R, Soc. Lond. A. **365** (1979) 1.

[37] Wagner F. et al., "Regime of improved confinement and high beta in neutral-beam heated divertor discharges of the ASDEX tokamak", Phys. Rev. Lett. **49** (1982) 1408.

[38] Doyle, E.J., et al., "Modifications in turbulence and edge electric fields at the L-H transition in the DIII-D tokamak", Phys. Fluids B **3** (1991) 2300.

[39] Suttrop, W., et al., "Identification of plasma-edge-related operational regime boundaries and the effect of edge instability on confinement in ASDEX Upgrade", Plasma Phys. and Contr. Fusion, **39** (1997) 2051.

[40] Takase, Y., et al.,"Radiofrequency-heated enhanced confinement modes in the Alcator C-Mod tokamak", Phys. of Plasmas, **4** (1997) 1647.

[41] Hubbard, A.E., et al.,"Pedestal profiles and fluctuations in C-Mod enhanced D-alpha H-modes", Phys. of Plasmas, **8** (2001) 2033.

[42] Burrell, K.H. et al.,"Quiescent H-mode plasmas in the DIII-D tokamak", Plasma Phys. and Contr. Fusion, **44** (2002), A253.

[43] West, W.P. et al., "Energy, particle and impurity transport in quiescent double barrier discharges in DIII-D" Phys. of Plasmas **9** (2002) 1970.

[44] Suttrop, W., et al., "ELM-free stationary H-mode plasmas in the ASDEX Upgrade tokamak" Plasma Phys. Control. Fusion **45** (2003) 1399.

[45] Burrell, K.H. et al.,"Quiescent double barrier high-confinement mode plasmas in the DIII-D tokamak", Phys. of Plasmas **8** (2001) 2153.

[46] Greenfield, C.M., et al., "Quiescent Double Barrier Regime in the DIII-D Tokamak", Phys. Rev. Letters **86** (2001) 4544.

[47] Zohm, H., "Edge localized modes (ELMs)", Plasma Phys. and Contr. Fusion, **38** (1996) 105.

[48] Kass, T., et al., "Characteristics of Type I and Type III ELM Precursors in ASDEX Upgrade", Nuclear Fusion, **38** (1998), 111.

[49] Marascheck M., et al.,"MHD Characteristics of ELMs and their Precursors", Proceedings of 25th EPS Conference on Controlled Fusion, Prague, (1998), 492.

[50] Bolzonella T., et al. "ELM-related High Frequency MHD Activity in ASDEX Upgrade" ,2002 29th EPS Conference on Plasma Phys. Contr. Fusion, (Montreaux) Vol. 26B, P-1.038.

[51] Perez, C.P., et al., "Type-I ELM Precursor Modes in JET", submitted to Nuclear Fusion (2003).

[52] Perez, C.P., et al., "Washboard modes as ELM-related events in JET", Plasma Phys. and Contr. Fusion **46** (2004) 61.

[53] Connor, J.W., "A review of models for ELMs", Plasma Phys. and Contr. Fusion, **40** (1998) 191.

[54] Manickam, J., "The role of edge current density on kink mode stability and its implication for magnetohydrodynamic activity associated with edge localized modes", Phys. Fluids B **4** (1992) 1901.

[55] The ASDEX Team, "The H-mode of ASDEX", Nucl Fusion **29** (1989) 1959.

[56] Lebedev, V.B., Diamond, P.H., Gruzinova, I. and Carreras, B.A.,"A minimal dynamical model of edge localized mode phenomena", Phys. Plasmas **2** (1995) 3345.

[57] Connor, J.W., Hastie, R.J., Wilson H.R., Miller, R.L., Magnetohydrodynamic stability of tokamak edge plasmas", Phys. of Plasmas, **5** (1998) 2687.

[58] Ferron, J.R. et al.,"Modification of high mode pedestal instabilities in the DIII-D tokamak", Phys. of Plasmas, **7** (2000) 1976.

[59] Snyder, P.B. et al. "Edge localized modes and the pedestal: A model based on coupled peeling ballooning modes" Phys. of Plasmas **9** (2002) 2037.

[60] Degeling, A.W., et al., "Magnetic triggering of ELMs in TCV", Plasma Phys. and Contr. Fusion, **45** (2003) 1637.

[61] Becoulet, M., et al., "Edge localized mode physics and operational aspects in tokamaks", Plasma Phys. and Contr. Fusion, **45** (2003) A93.

[62] Sartori, R., et al. "Study of Type III ELMs in JET", Plasma Phys. and Contr. Fusion, **46** (2004) in press.

[63] Lang, P.T., et al., "ELM frequency control by continuous small pellet injection in ASDEX Upgrade", Nuclear Fusion**43** (2003) 1110.

[64] Rapp, J., et al.,"ELM mitigation by nitrogen seeding in the JET gas box divertor", Plasma Phys. and Contr. Fusion **44** (2002) 639.

[65] S. Jachmich et al., "Seeding of impurities in JET H-mode discharges to mitigate the impact of ELMs", Plasma Phys. and Contr. Fusion **44** (2002) 1879.

[66] Maddison, G.P., et al., "Impurity-seeded plasma experiments on JET", Nuclear Fusion**43** (2003) 49.

[67] Kubo, H., et al., "High radiation and high density experiments in JT-60U", Nuclear Fusion**41** (2001) 227.

[68] Maddison, G.P. et al., "Improved ELM scaling with impurity seeding in JET", Plasma Phys. Control. Fusion **45** (2003) 1657.

[69] Moyer, R.A. and Evans, T.E., "3D non-axisymmetric effects in the DIII-D boundary", 2002 29th EPS Conference on Plasma Phys. Contr. Fusion, (Montreaux) Vol. 26B, P-1.063.

[70] Saarelma S., Günter, S.,Kurki-Suonio, T., Zerhfeld, H.-P., "Plasma Phys. and Contr. Fusion, **42** (2000) A139.

[71] Stober, J. et al, "Type II ELMy H modes on ASDEX Upgrade with good con nement at high density", Nucl. Fusion **41** (2001) 1123.

[72] Kamada, Y. et al., "Disappearance of giant ELMs and appearance of minute grassy ELMs in JT-60U high-triangularity discharges", Plasma Phys. and Contr. Fusion, **42** (2000) A247.

[73] Turnbull, A.D., Osborne, T.H., Strait, E.J., Lao, L.L., Miller, R.L., Taylor, T.S., "Identification of Intermediate n Ideal MHD Kink-Peeling Modes with ELMs in DIII-D H-Mode Discharges", Bull. Am. Phys. Soc. 43 (1998), 1761.

[74] Pereverzev G.V. et al., "ASTRA An Automatic System for Transport Analysis in a Tokamak", IPP Report 5/42, MPI f. Plasmaphysik, Garching (1991).

[75] Zehrfeld, H.P., "Equilibrium and Ballooning Stability of Resistive Tokamak Plasmas Near the Separatrix", Proceedings of the 25th EPS Conference on Controlled Fusion, Prague, (1998), 1927-1930.

[76] Suttrop, W., "The physics of large and small edge localized modes", Plasma Physics and Controlled Fusion, 42 (2000), A97.

[77] Ozeki, T. et al., "Plasma Shaping, Edge Ballooning stability and ELM Behaviour in DIII-D", Nuclear Fusion **30** (1990) 1425.

[78] Kamada, Y. et al,"Onset condition for ELMs in JT-60U", Plasma Phys. and Contr. Fusion, **38** (1996) 1387.

[79] Kamada Y. et al., "Pedestal characteristics and extended high-p ELMy H-mode regime in JT-60U", Plasma Phys. and Contr. Fusion, **44** (2002) A279.

[80] Greene, J.M. and Chance, M.S., "The second region of stability against ballooning modes", Nucl. Fusion **21** (1981) 453.

[81] Saibene, G. et al.,"Pedestal and ELM characterisation of highly shaped Single Null and Quasi Double Null plasmas in JET, at high confinement and density.", 2003 30th EPS Conference on Plasma Phys. Contr. Fusion, (St. Petersburg), Vol. 27A, P-1.92.

[82] Campbell, D.J., et al.,"H-modes under steady-state conditions in JET" Plasma Phys. Control. Fusion **36** (1994) A255.

[83] Horton, L.D., et al.,"Studies in JET divertors of varied geometry. I: Non-seeded plasma operation", Nucl. Fusion **39** (1999) 1.

[84] Saibene, G., et al., "The in uence of isotope mass, edge magnetic shear and input power on high density ELMy H modes in JET", Nucl. Fusion **39** (1999) 1133.

[85] Suttrop, W., et al., "High density, high performance high-confinement-mode plasmas in the Joint European Torus (JET)", Phys. of Plasmas **9** (2002) 2103.

[86] Loarte, A., et al., "Characteristics and scaling of energy and particle losses during Type I ELMs in JET H-modes", Plasma Phys. Control. Fusion **44** (2002) 1815.

[87] the JET Team, "Highly Radiating and Detached Plasmas on Carbon and Beryllium Targets", Plasma Phys. Control. Fusion **37** (1995) A227.

[88] M. Kempenaars et al 2003 "Edge gradient and pedestal measurements of ELMy H-mode plasmas at JET", 30th EPS Conf. on Controlled Fusion and Plasma Physics (St Petersburg vol 27A (ECA) EPS 2003.

[89] Houlberg, W.A., Shaing, K.C., Hirshman, S.P., Zarnstorff, M.C., "Bootstrap current and neoclassical transport in tokamaks of arbitrary collisionality and aspect ratio", Phys. of Plasma, **4** (1997), 3230.

[90] Suttrop, W., et al., "ELM-free stationary H-mode plasmas in ASDEX Upgrade", 2003 30th EPS Conference on Plasma Phys. Contr. Fusion, (St. Petersburg), Vol. 27A, P-1.125.

[91] Lonnroth, J.-S et al., "Integrated predictive modelling of the effect of neutral gas puffing in ELMy H-mode plasmas", Plasma Phys. Control. Fusion **45** (2003) 1689.

[92] Medvedev, S.Yu., et al.,"Edge Kink/Ballooning Mode Stability in TCV", Proc. of the 30th EPS Conference on Plasma Phys. Contr. Fusion, (St. Petersburg) (2003), Vol. 27A, P-3.129.

Abstracts of publications 1-5:

1. An ELMy ASDEX Upgrade plasma equilibrium is reconstructed taking into account the bootstrap current. The peeling mode stability of the equilibrium is numerically analysed using the GATO [1] code, and it is found that the bootstrap current can drive the plasma peeling mode unstable. A high-n ballooning mode stability analysis of the equilibria revealed that, while destabilizing the peeling modes, the bootstrap current has a stabilizing effect on the ballooning modes. A combination of these two instabilities is a possible explanation for the type I ELM phenomenon. Atriangularity scan showed that increasing triangularity stabilizes the peeling modes and can produce ELM-free periods observed in the experiments.

2. An MHD stability analysis of the plasmas with type II ELMs is presented. The stability properties in type II ELMy plasmas (high-q_{95}, high) are found to significantly di er from those of the type I ELMy plasmas. The differences between the type I and type II ELM cycles due to these stability properties are described.

3. We investigated the differences between type I and type II edge localized modes (ELMs) in ASDEX Upgrade using the MHD stability analysis. When plasma conditions are changed from typical type I ELMy conditions to type II ELMy conditions, the character of the edge instabilities change. With increased triangularity and edge safety factor, the low-n peeling ballooning mode becomes more stable and more localized to the edge region. We find the same mode localization effect in almost double null configuration. When the plasma density is increased, the access to the second stability of the high-n ballooning modes is closed. The changes in the stability properties give a qualitative explanation to the observed small amplitude of the type II ELMs.

4. An MHD stability analysis of the edge plasma shows that in highly triangular plasmas, the increasing global β_p has a stabilizing effect on the low-n instabilities that trigger edge localized modes (ELMs). The improved stability allows the access of higher edge pressure gradients before the ELM is triggered. At the same time, the edge plasma moves closer to the high-n ballooning mode stability boundary. The stability changes can explain why the high value of β_p helps to access smaller ELMs.

5. The plasma edge MHD stability is analysed for several JET discharges in the Diagnostic Optimized Configuration (DOC). The stability analysis of Type I ELMy plasmas shows how after an ELM crash the plasma edge is deep in the stable region against low- to intermediate-n peeling-ballooning modes. As the pressure gradient steepens and the edge current builds up, the plasma reaches the low- to intermediate-n peeling-ballooning mode stability boundary just before the ELM crash. Increasing the plasma fueling by gas puffing makes the second stability access against high-n ballooning modes narrower until it closes completely and the ELMs change from Type I to Type III. Reducing the plasma heating has a similar effect. Increasing the safety factor at the plasma edge improves the stability against low- to intermediate-n modes allowing steeper pressure gradients to develop before an ELM crash.